

EFFECT OF DEPOSITION PARAMETERS ON SILICON LAYERS TRANSITION
FROM AMORPHOUS PHASE TO MICRO/NANO-CRYSTALLINE PHASE IN
DIFFERENT DEPOSITION TECHNIQUES

A THESIS SUBMITTED TO
THE GRADUATE SCHOOL OF NATURAL AND APPLIED SCIENCES
OF
MIDDLE EAST TECHNICAL UNIVERSITY

BY

GİZEM NOGAY

IN PARTIAL FULFILLMENT OF THE REQUIREMENTS
FOR
THE DEGREE OF MASTER OF SCIENCE
IN
PHYSICS

AUGUST 2013

Approval of the thesis:

**EFFECT OF DEPOSITION PARAMETERS ON SILICON LAYERS TRANSITION
FROM AMORPHOUS PHASE TO MICRO/NANO-CRYSTALLINE PHASE IN
DIFFERENT DEPOSITION TECHNIQUES**

Submitted by **GİZEM NOGAY** in partial fulfillment of the requirements for the degree of
Master of Science in Physics Department, Middle East Technical University by,

Prof. Dr. Canan Özgen
Dean, Graduate School of **Natural and Applied Sciences**

Prof. Dr. Mehmet Zeyrek
Head of Department, **Physics**

Prof. Dr. Raşit Turan
Supervisor, **Physics Dept., METU**

Examining Committee Members:

Prof. Dr. Çiğdem Erçelebi
Physics Dept., METU

Prof. Dr. Raşit Turan
Physics Dept., METU

Prof. Dr. Mehmet Parlak
Physics Dept., METU

Assist. Prof. Dr. Y. Eren Kalay
Metallurgical and Materials Engineering Dept., METU

Dr. Baybars Oral
VAKSIS Company

Date : *01.08. 2013*

I hereby declare that all information in this document has been obtained and presented in accordance with academic rules and ethical conduct. I also declare that, as required by these rules and conduct, I have fully cited and referenced all material and results that are not original to this work.

Name, Last name : GİZEM NOGAY

Signature :

ABSTRACT

EFFECT OF DEPOSITION PARAMETERS ON SILICON LAYERS TRANSITION FROM AMORPHOUS PHASE TO MICRO/NANO-CRYSTALLINE PHASE IN DIFFERENT DEPOSITION TECHNIQUES

Nogay, Gizem
M.Sc., Department of Physics
Supervisor: Prof. Dr. Raşit Turan

August 2013, 101 pages

Hydrogenated nano/micro-crystalline silicon (nc-/ μ c-Si:H) thin films are the key materials for Si-based thin film solar cell technology. These films have attracted great attention due to their applications in thin film solar cells. Silicon phase transition from amorphous to nano/micro-crystalline phase is an important phenomenon, especially in progress of Si thin film tandem structured solar cells. It is well-accepted fact that the development of deposition phase diagrams allows phase engineering for systematic improvement of materials and cell structures. In this thesis, crystallization dynamics of the amorphous silicon prepared via different deposition techniques such as magnetron sputtering, electron beam evaporation, CCP-assisted CVD and ICP-assisted CVD have been investigated. The advantages and disadvantages of these production methods have been debated by considering different aspects such as cost efficiency, film uniformity, deposition rate and applicability. For each technique, different deposition parameters such as deposition power, pressure, coating duration, substrate temperature, and source gas dilution were investigated comprehensively. Deposited films were analyzed in structural, morphological, optical and electrical features. Films are deposited on different substrate such as glass, quartz and Si-wafer and basic diagnostic tools like Raman Spectroscopy (RS), Grazing Incidence X-Ray Diffraction (GR-XRD), X-Ray Photoelectron Spectroscopy (XPS), Spectroscopic Ellipsometry (SE), Fourier Transform Infra-Red Spectroscopy (FTIR), Scanning Electron Microscopy (SEM), High Resolution Transmission Electron Microscopy (HRTEM) are used as complementary methods. Crystalline volume fraction calculated by RS is assumed as the key parameter while defining the structural transition. At the end of this research, general knowledge about the crystallization parameters for different chemical and physical vapor deposition techniques was obtained.

Keywords: Plasma Enhanced Chemical Vapor Deposition, Silicon, Crystallization, Inductively Coupled Plasma, Raman Spectroscopy

ÖZ

FARKLI ÜRETİM METODLARI KULLANILARAK BÜYÜTÜLEN SİLİSYUM TABAKALARININ AMORF FAZDAN MİKRO/NANO KRİSTAL FAZINA GEÇİŞİ

Nogay, Gizem
Yüksek Lisans, Fizik Bölümü
Tez Yöneticisi: Prof. Dr. Raşit Turan

Ağustos 2013, 101 sayfa

Hidrojenlendirilmiş nano / mikro kristal silisyum (nc-/µc-Si:H) ince film malzemeler, Silisyum tabanlı ince film güneş gözeleri teknolojisinin anahtar malzemesidir. Bu filmler ince film güneş gözeleri uygulamalarında kullanılması nedeniyle yüksek oranda ilgi çekmektedir. Özellikle birbiri ardına dizilmiş çoklu Silisyum tabanlı ince film güneş gözeleri uygulamaları için silisyumun amorf fazdan nano / mikro kristal faza geçişi incelenmesi gereken önemli bir süreçtir. Böyle bir faz diyagramı oluşturmak malzemelerin ve göze yapılarının geliştirilmesinde kullanılacak fazların belirlenmesini mümkün kılacaktır. Bu çalışma kapsamında plazma ortamında kimyasal buhar biriktirme, magnetron saçtırma ve elektron demeti buharlaştırma gibi farklı yöntemlerle üretilen amorf silisyum ince film malzemesinin kristalleşme dinamikleri incelenmiştir. Bu birbirlerinden farklı yöntemlerin uygun maliyetliliği, film homojenliği, birikinti hızı ve uygulanabilirliği gibi özellikleri göz önünde bulundurularak birbirlerine göre avantajları ve dezavantajları araştırılmıştır. Her bir teknik için birikinti gücü, basıncı, kaplama süresi, alt taş sıcaklığı ve kullanılan besleme gazinin seyreltilme miktarı gibi parametreler ayrıntılı bir biçimde incelenmiştir. Büyütülen filmlerin yapısal, biçimsel, ışık ve elektriksel özellikleri analiz edilmiştir. Silisyum ince filmler cam, kuartz ve silisyum dilimlerin üzerine büyütülmüş olup Raman Spektroskopisi (RS), X-Işını Kırınımı (GIXRD), X-Işını Foto elektron Spektroskopisi (XPS), Ellipsometer (SE), Fourier Dönüşümlü Kızılötesi Spektroskopisi (FTIR), Taramalı Elektron Mikroskopu (SEM), Yüksek Kontrastlı Transmisyon Elektron Mikroskopu (HRTEM) gibi analiz metodlarıyla kontrol edilmiştir. Bu çalışmada Raman Spektroskopi analizinden hesaplanan kristal hacim fraksiyonu yapısal geçişi göstermede ana parametre olarak kabul edilmiştir. Bu araştırmanın sonunda, farklı fiziksel ve kimyasal buhar biriktirme metodları için kristalleşme parametreleri hakkında ayrıntılı ve güvenilir bilgi edinilmiştir.

Anahtar Kelimeler: Plazma Destekli Kimyasal Buhar Biriktirme, Silisyum , Kristallenme, İndüktif Eşleşmiş Plazma, Raman Spektroskopisi

To My Lovely Family...

ACKNOWLEDGMENTS

First and foremost, I would like to thank my supervisor Prof. Dr. Raşit Turan for providing me the opportunity to be a member of his research group. I am very grateful to him for his guiding, encouragement, perceptiveness and informative discussions during my study. I believe that his expertise gave me a significant knowledge, which I would use during my whole career.

I would like to thank Prof. Dr. Mehmet Parlak for his help and support. Assoc. Prof. Dr. Zaki Saleh and Assis. Prof. Alpan Bek for their informative discussions about my studies. Assis. Prof. Kadir Erturk for his help about e-beam evaporated samples and adapting his experience with instructive observations.

I would like to thank Serim Ilday for her comments, discussions and precious suggestions about this study. Being a part of her work was extremely valuable experience for me. I want to send special thanks to Engin Özkol for sharing his experience and equipment knowledge with me, making the laboratory very amusing place for me. Zeynep Demirciođlu for helping me during the CCP samples depositions and anytime I needed.

Also, I would like to thank to Dr. Baybars Oral and Mehmet Kabadayi from VAKSIS company for production of PECVD system used in this study, technical support and valuable comments. Harun Tanik for his encouragements. Seçkin Öztürk for very nice and clear HRTEM images and Sedat Canlı for long hours of SEM sessions. Firat Es for 3D drawing of systems schematics with CATIA. Dr. Tunay Tansel for his help during optimizing FTIR measurement equipment. Emre Mulazimođlu for his suggestion about TEM sample preparation and his creativity.

Also, I want to thank to my present and former group partners; Dr. Mustafa Kulakçı, Hisham Nasser, Hande Çiftpınar, Olgu Demirciođlu, Salar Habibur, Mehmet Karaman, Gülsen Baytemir, Makbule Bilgen, Yasin Ergunt, Burcu Barutçu, İrem Tanyeli, Mona Zolfaghariborra, Mete Günoven. GÜNAM staff; Buket Gökbakan, technician Nevzat Görmez, technician Dursun Erdoğan, technician Tayfun Yıldız.

I would like to thank Uđur Akyıldız for his endless support and patience during writing process of this thesis. Also I should not forget the language corrections that he performed. I finally thank to my family for their support and encouragements.

TABLE OF CONTENTS

ABSTRACT.....	v
ÖZ.....	vi
ACKNOWLEDGMENTS	viii
TABLE OF CONTENTS.....	ix
LIST OF TABLES	xi
LIST OF FIGURES	xii
LIST OF ABBREVIATIONS.....	xv
CHAPTERS	
1. INTRODUCTION	1
1.1 Importance of Photovoltaics	1
1.2 PV Materials	2
1.3 Silicon Based Thin Film Solar Cells.....	3
1.3.1 Structure and Operation principle of thin film silicon solar cells	4
1.3.2 Configuration of thin film silicon solar cells	6
1.4 Motivation of the Work.....	8
2. EXPERIMENTAL.....	9
2.1 Deposition Techniques.....	9
2.1.1 Plasma Enhanced Chemical Vapor Deposition (PECVD).....	9
2.1.2 Magnetron Sputtering	16
2.1.3 Electron Beam Evaporation	17
2.2 Plasma Diagnostics	19
2.2.1 Optical Emission Spectroscopy	19
2.3 Material Characterization.....	20
2.3.1 Spectroscopic Ellipsometry.....	20
2.3.2 Raman Spectroscopy.....	23
2.3.4 Grazing Incidence X-Ray Diffraction (GI-XRD) Spectroscopy.....	25
2.3.5 Fourier Transform Infra-Red (FTIR) Spectroscopy.....	27
2.3.6 Photoluminescence (PL)	30
2.3.7 Conductivity Measurements	33
3. CRYSTALLIZATION PROPERTIES OF Si-THIN FILMS PREPARED BY DIFFERENT DEPOSITION TECHNIQUES	35
3.1 Crystallization of CCP-CVD Deposited Si-Thin Films	35

3.1.1	Pressure Effect.....	35
3.1.2	Effect of Silane Concentration (SC).....	38
3.2	Crystallization of Si-Thin Films Deposited by Electron Beam Evaporation Technique.....	45
3.2.1	Effect of RTA duration.....	46
3.2.2	Effect of Deposition Rate.....	47
3.2.3	Effect of film thickness.....	53
3.3	Nanocrystalline Si formation in Silicon Rich Oxide System Deposited by Magnetron Sputtering.....	54
3.3.1	Structural Characterization.....	55
3.3.2	Optical Characterization.....	57
4.	STRUCTURAL PECULIARITIES AND AGING EFFECT IN Si-THIN FILMS PREPARED BY ICP-CVD.....	63
4.1	Effect of Deposition Power.....	64
4.1.1	Plasma Diagnostics and Deposition Rate.....	64
4.1.2	Crystallinity.....	65
4.2	Effect of Deposition Pressure.....	68
4.2.1	Plasma Diagnostics and Deposition Rate.....	68
4.2.2	Crystallinity.....	69
4.2.3	Morphology.....	71
4.2.4	Aging Effect.....	73
5.	OPTO-ELECTRONIC PROPERTIES OF Si THIN FILMS PREPARED BY ICP-CVD TECHNIQUE.....	79
5.1	Photoluminescence Properties.....	79
5.1.1	Pressure Effect.....	81
5.1.2	Hydrogen Dilution Effect.....	84
5.2	Band Gap Estimation.....	86
5.3	Electrical Characterization.....	87
5.3.1	Pressure Effect.....	87
5.3.2	Hydrogen Dilution Effect.....	88
6.	CONCLUSIONS AND FUTURE STUDIES.....	91
	REFERENCES.....	95

LIST OF TABLES

TABLES

Table 2-1 Detectable species with various optical spectroscopy methods.....	19
Table 2-2 Vibration modes and wavenumber for hydrogenated silicon films.....	29
Table 3-1 Deposition parameters of the films fabricated at room temperature with different pressure.....	36
Table 3-2 Deposition parameters of the films fabricated at 200 ⁰ C with different SC.....	38
Table 3-3 Calculated grain size from Raman spectrum.....	39
Table 3-4 Summary of GI-XRD data of films deposited with different SiH ₄ concentration.	41
Table 3-5 Calculated conductivity values of the films deposited with different H ₂ dilution.	45
Table 3-6 Results of the SE spectra analysis obtained for films deposited with 1, 5, 20, 50 1 Å/s rates. Values of thicknesses, optical constants at 622 nm and Raman crystalline volume fractions.	52
Table 3-7 Volume fractions calculated from XPS peak fitting and SE spectral data fittings	62
Table 4-1 Deposition parameters for the samples fabricated via ICP-CVD technique	64
Table 4-2 Hydrogen concentration changes with deposition pressure.....	75
Table 5-1 Positions and origins of the deconvoluted Gaussian components of PL spectra[131]	80
Table 5-2 Summary of XRD data for the Si thin films deposited with different hydrogen dilution.....	85

LIST OF FIGURES

FIGURES

Fig 1-1 Part of the periodic table, showing the important elements for solar cell application .	2
Fig 1-2 Highest confirmed efficiencies for $\geq 1\text{-cm}^2$ area cells fabricated using the different technologies [3]	3
Fig 1-3 p-i-n structure and charge transport mechanism	5
Fig 1-4 Basic configurations of p-i-n solar cells: (a) a-Si:H single junction solar cell (b) Micromorf (a-Si:H/ $\mu\text{c-Si:H}$) tandem solar cell	6
Fig 1-5 The spectral ranges which are absorbed by a-Si:H and $\mu\text{c-Si:H}$, respectively [10].....	7
Fig 2-1 Reactions occur in plasma environment [12]	10
Fig 2-2 Picture of multi-chamber PECVD system in GUNAM.....	12
Fig 2-3 Schematic illustration of conventional CCP-CVD system	13
Fig 2-4 Electron diffusion from bulk plasma to substrate (a), creation of sheath voltage (b), potential distribution in discharge (c).....	13
Fig 2-5 Cross-sectional view of ICP-CVD chamber (a), relative directions of E-field, B-field and induced current (I_{rf})(b).....	15
Fig 2-6 Schematic diagram of ICP-CVD chamber.....	15
Fig 2-7 Particle movement in magnetic field (a), B-field lines produced by magnetrons (b) 16	16
Fig 2-8 Schematic diagram of magnetron sputtering system	17
Fig 2-9 Schematic representation of electron beam evaporation mechanism	18
Fig 2-10 Typical OES spectrum of H_2 diluted SiH_4 plasma.....	20
Fig 2-11 Measurement principle of SE [25].....	21
Fig 2-12 Elliptically polarized light and definition of Δ and Ψ	21
Fig 2-13 Spectroscopic Ellipsometry reference data of the imaginary part of dielectric function ϵ_i for single-crystalline (c-Si), micro-crystalline ($\mu\text{c-Si}$), nano-crystalline (nc-Si) and amorphous (a-Si) silicon [27].....	22
Fig 2-14 Frequency shift after photon - matter interaction; Anti-Stokes shift (a), Stokes shift (b).	23
Fig 2-15 Reference RS data for phase transition of the silicon thin film [10].....	24
Fig 2-16 Deconvolution of the Raman spectrum for micro crystalline silicon sample.	25
Fig 2-17 Basic feature of typical XRD measurement	26
Fig 2-18 Reference data of XRD spectra for crystal silicon.....	27
Fig 2-19 All stretching and bending vibrations of C-H bonds	28
Fig 2-20 Local Si-H vibrational modes for SiH and SiH_2 group[32].....	29
Fig 2-21 Typical IR absorption spectrum of a-Si:H thin film[4]	30
Fig 2-22 Schematic diagram for the different optical absorption mechanism in materials[35]	31
Fig 2-23 Simplified energy diagram of Si [36]	32
Fig 2-24 Schematic of the experimental apparatus used for PL measurement.....	32

Fig 2-25 Experimental structure for co-planar conductivity measurements on silicon layers.	33
Fig 3-1 Raman spectrum of the films deposited at room temperature with different deposition pressure.	36
Fig 3-2 Raman spectrum of the films deposited at 200 ⁰ C with different deposition pressure.	37
Fig 3-3 Raman spectrum of the films deposited at 200 ⁰ C with different SiH ₄ concentration	39
Fig 3-4 GI-XRD spectrum of the films deposited at 200 ⁰ C with different SiH ₄ concentration	40
Fig 3-5 FTIR Spectra of films deposited with different SiH ₄ concentration	41
Fig 3-6 Deconvolution of the Si-H _x stretching mode.	42
Fig 3-7 Estimated bonded hydrogen content C _H of films deposited with different SiH ₄ concentration.	43
Fig 3-8 Dark I-V Characteristics of the films deposited with different H ₂ dilution.	44
Fig 3-9 Dark and illuminated I-V characteristics for samples with different crystallinity	44
Fig 3-10 Raman spectra of the Si films by RTA at 800 °C for 100, 300, 600 and 900 s. The inset shows the Raman crystalline volume fraction variation of these samples	46
Fig 3-11 XRD spectra of the Si films that is annealed with RTA at 800 °C for 100, 300, 600 and 900 s.	47
Fig 3-12 Schematic of film structure used as optical model in SE analyses.	47
Fig 3-13 Band gap enhancement after 1-hour H ₂ treatment at RTA system.	49
Fig 3-14 RS of the samples, annealed at 800 ⁰ C for 10min, deposited with various deposition rates; 1A/s, 5A/s, 20A/s and 50A/s.	49
Fig 3-15 XRD patterns of the samples deposited with various deposition rates; 1A/s, 5A/s, 20A/s and 50A/s and annealed at 800 ⁰ C for 10min.	50
Fig 3-16 Pseudo-dielectric function spectrereal part of the complex function (a) and imaginary part of the complex function (b), for the sample deposited with 1, 5, 20 Å/s and reference c-Si.	51
Fig 3-17 RS and GI-XRD spectra of the samples, annealed at 800 ⁰ C for 10 minute, deposited with various deposition rates and thicknesses. Two samples with 5 Å/s rate and two different thickness 250 nm & 500 nm (a,b), two samples with 1 Å/s rate and two different thickness 500 nm & 1000 nm (c,d).	53
Fig 3-18 Raman measurement of the films deposited with different Si-target power and annealed at 1100 ⁰ C.	56
Fig 3-19 HRTEM image of nc-Si within SRO film deposited with 81W Si-target power and annealed at 1100 ⁰ C for 1 hour.	57
Fig 3-20 PL analyses of the films deposited with different Si-target power (different excess Si amount) and annealed at 1100 ⁰ C for 1 hour.	58
Fig 3-21 Schematic of the film structure used as optical models in SE analyses for the films with low excess Si (a) and for the films with high excess Si (b)	59
Fig 3-22 SE spectral data and their fitting by applying TL and BEMA to the models for SRO film deposited with 18 W (a) 189 W (b) Si-target power	59
Fig 3-23 Annealing dependence of imaginary dielectric function (ε _i) for the SRO film deposited with 189 W Si-target power.	60

Fig 3-24 Cross-sectional bright field TEM images of the films deposited with 126 W (a) and 81W (b) Si target power	61
Fig 4-1 Applied power density dependence of deposition rate (a) and OES emission lines for the two different samples deposited at different power density (b).	64
Fig 4-2 RS for the ICP-CVD deposited samples with various power	66
Fig 4-3 GI-XRD spectra for the ICP-CVD deposited samples with various power.....	66
Fig 4-4 SEM images of the samples deposited with various power 2500 W (a), 2750 W (b), 3000 W (c) and Comparison of the calculated grain sizes with RS and GI-XRD (d).....	67
Fig 4-5 The effect of deposition pressure on optical emission spectroscopy (OES) spectra of the thin films (a), OES intensity change as a function of the deposition pressure of detectable plasma species (b).	68
Fig 4-6 RS spectra of the samples deposited at different deposition pressures.....	69
Fig 4-7 GI-XRD spectra of the Si thin films deposited at various deposition pressures.....	70
Fig 4-8 Surface topography (a) and Cross-sectional SEM images (b) of nc-Si thin film. Surface topography (c) and Cross-sectional SEM images (d) of a-Si thin film.	71
Fig 4-9 HRTEM images of Si:H cauliflower-like structure (a) and an individual Si:H bundle (b).	73
Fig 4-10 FTIR spectra of the samples deposited with various deposition pressures. Shifting of Si-H rocking/wagging mode with respect to deposition pressure (inset).	74
Fig 4-11 Variation of FTIR spectra with time (inset) integrated area change of Si-O-Si stretching mode signal.....	75
Fig 4-12 XPS depth-profiling spectrum of the film deposited with 10mTorr pressure at room temperature: O 1s core level (a), Si 2p core level (b) and atomic concentration percentage of O and Si extracted from XPS depth-profiling analyses(c).	76
Fig 5-1 Schematic energy level diagram and competing PL mechanisms for Si nanocrystals surrounded by large band gap material	80
Fig 5-2 PL Spectra of the samples fabricated at various deposition pressures.....	81
Fig 5-3 Positions of the deconvoluted three Gaussian components for three different pressures	82
Fig 5-4 The shift in position of peak-I of the PL spectra normalized to unity for the films deposited room temperature and at different pressures as indicated.	83
Fig 5-5 HRTEM images of three films deposited at room temperature and: 15-mTorr (a) 25-mTorr (b) and 35-mTorr (c)	83
Fig 5-6 The PL (a), RS (b) and GI-XRD (c) spectra for two films deposited at room temperature, 25 mTorr and different hydrogen dilution as indicated.....	84
Fig 5-7 HRTEM images for the samples deposited with 95% (a) and 90% (b) hydrogen dilution.	85
Fig 5-8 The optical band gap as determined from the Tauc's plot versus deposition pressure	86
Fig 5-9 Measured Current-Voltage spectra of the samples deposited at 15mTorr (a) and 25mTorr (b). Variation of dark conductivity with deposition pressure (c).	87
Fig 5-10 Measured current-voltage spectra of the samples deposited with different hydrogen at room temperature in the dark ambient.....	88

LIST OF ABBREVIATIONS

ABBREVIATIONS

CVD	Chemical Vapor Deposition
PECVD	Plasma Enhanced Chemical Vapor Deposition
CCP	Capacitively Coupled Plasma
ICP	Inductively Coupled Plasma
PVD	Physical Vapor Deposition
SPC	Solid Phase Crystallization
RTA	Rapid Thermal Annealing
OES	Optical Emission Spectroscopy
SE	Spectroscopic Ellipsometer
FTIR	Fourier Transform Infra-Red Spectroscopy
FWHM	Full Width Half Maximum
TO	Transverse Optical
LO	Longitudinal Optical
RS	Raman Spectroscopy
GI-XRD	Grazing Incidence X-Ray Diffraction Spectroscopy
SEM	Scanning Electron Microscopy
HRTEM	High Resolution Transmission Electron Microscopy
BFTEM	Bright Field Transmission Electron Microscopy
PL	Photoluminescence
XPS	X-Ray Photoelectron Spectroscopy
SC	Silane Concentration
TL	Tauc-Lorentz
BEMA	Bruggemen Effective Medium Approximation
SRO	Silicon Rich Silicon Oxide
DC	Direct Current
RF	Radio Frequency
CP	Critical Points

CHAPTER 1

INTRODUCTION

1.1 Importance of Photovoltaics

Today, energy generation and consumption without causing any harm to natural resources and environmental is very essential for the human life on our planet. Conventional energy sources like natural gas, coal and fossil fuels are limited resources and also cause fatal environmental problems such as air pollution, acid rain and greenhouse effect. To avoid these problems and prepare a safe and clean future for our planet and society, the use of renewable energy sources like wind, water and sun will be imperative.

Among the renewable energy sources that are available in different geological parts of the earth, the solar energy is the only one that has the potential to supply large-scale energy demands all over the world. The amount of energy arriving on earth from the sun is enormous, like 10 000 times the current energy consumption of the human race [1]. Moreover, sun is natural, unlimited, free and abundant. In general, there are two ways of benefitting from sun; thermal solar energy that transforms solar energy into thermal energy and electricity generation. For the electricity generation there exist two major technologies: Concentrated Solar Power (CSP) which first converts the solar radiation to thermal power for steam generation and then generate electricity using steam engines; and Photovoltaics (PV) that converts the sunlight directly into electricity using appropriate semiconductor devices called solar cells.

Solar cells made of semiconducting materials consist of a junction with a built-in electrical potential that provides the necessary driving force for the generation electrical current after the sunlight is absorbed by the active part of the cell. Solar cells are silent, does not have any moving part, clean and durable for many years. Although the material and manufacturing cost of PV systems were too expensive, with the price fall driven by far east companies, it has been quite competitive in recent years. Unlike other renewable energy technologies, PV modules operate autonomously with low operating and maintenance cost. However, the most significant drawback of the PV system is that they energy storage capability and is not usable during the nighttime. Independent storage systems (battery, hydrogen, heat etc.) should be developed to supply the energy consumption when the sunshine is not present.

The ultimate cost of the electricity is directly related to the conversion efficiency, which has been studied very intensively in the last 3 – 4 decades. Research activities are focused on both material and device aspects of the cell technologies. With these efforts, significant improvements in the conversion efficiency have been achieved. Among many approaches, fabrication of tandem solar cells utilizing different materials can be given as a successful example for the efforts towards higher efficiencies. Tandem cells made of III-V compound

semiconductors have reached record efficiency of 44 % under concentrated light. However, high material and system cost is preventing wide application of this technology. Driven by the cost requirements, thin film solar cells made of CdTe / CdS, CIGS / CdS, and a-Si / $\mu\text{c-Si}$ have been developed. In the case of Si based thin film systems, efficiency values up to 13 % have been obtained.

1.2 PV Materials

The history of photovoltaics started with discovery of photovoltaic effect in 1839 by a French experimental physicist Edmund Becquerel. Many years later, scientific investigation of Albert Einstein and Schottky provided detailed description of this effect and material-light interaction. Large number of materials show photovoltaic characteristics, however only very limited part of such materials can convert the energy of light photons into electricity with high efficiency, high stability and low cost [2].

The solids with metallic bond are good conductors and those with covalent bond are generally good insulators, and between these two groups there is an important material type called semiconductors [2]. Controllable conductivity property of semiconductors makes them very interesting and important for microelectronic and solar cell applications. In Fig 1-1, a small part of the periodic table is shown. Semiconductors from either group IV of the periodic table, or from a combination of group III and V (III-V semiconductors) and II-VI semiconductors such as silicon (Si), gallium arsenide (GaAs), indium phosphide (InP), copper indium (di)selenide (CuInSe_2), cadmium telluride (CdTe), copper indium gallium (di)selenide (CuInGaSe_2 or CIGS) are being used in photovoltaic applications.

							VIII A									
							2	He								
							5	6	7	8	9	10				
							III A	IVA	VA	VIA	VII A	VIII A				
							B	C	N	O	F	Ne				
							10.811	12.011	14.007	15.999	18.998	20.183				
							13	14	15	16	17	18				
							Al	Si	P	S	Cl	Ar				
							26.982	28.086	30.974	32.064	35.453	39.948				
IB	IIB								29	30	31	32	33	34	35	36
Cu	Zn	Ga	Ge	As	Se	Br	Kr	63.54	65.37	69.72	72.59	74.922	78.96	79.909	83.80	
47	48	49	50	51	52	53	54	Ag	Cd	In	Sn	Sb	Te	I	Xe	
107.870	112.40	114.82	118.69	121.75	127.60	126.904	131.30									
79	80	81	82	83	84	85	86	Au	Hg	Tl	Pb	Bi	Po	At	Rn	
196.967	200.59	204.37	207.19	208.980	(210)	(210)	(222)									

Fig 1-1 Part of the periodic table, showing the important elements for solar cell application

Performance of photovoltaics solar cells are related with the characteristics of materials used for manufacturing. Band-gap, absorption coefficient, minority carrier lifetime and minority carrier diffusion length are the main parameters determining the performance of the solar cell. Ideally, they should have a high optical absorption in the wavelength range from 350nm to 1000nm, long diffusion length and low recombination velocity.

Fig 1-2 shows twenty years of progress in confirmed cell efficiencies fabricated using different technology and materials. Among them silicon is the most versatile and abundant one. Also it

is possible to use different forms of silicon such as single crystalline (c-Si), polycrystalline (poly-Si), microcrystalline ($\mu\text{-Si}$), nanocrystalline (nc-Si) and amorphous (a-Si) for solar cell applications. According to the solar cell efficiency table version 41, c-Si sub-module efficiency measured under the AM1.5 spectrum has achieved 25% [3], due to their high efficiencies and long term reliability, PV market is today dominated by c-Si and poly-Si technologies. However. In these technologies, mono-crystalline or multi-crystalline wafers with thicknesses of several hundreds of micrometers are required. Additionally, high energy consumption during fabrication makes this technology unsuitable for low-cost production [4]. This situation draws attention to the thin film technology, which provides extensive cost-reduction potential. As it is seen in Fig 1-2 thin films solar cell technologies such as CIGS and CdTe have been improved significantly. On the other hand silicon thin films solar cells have an advantage over the others of using silicon as raw material. With the potential improvements in material and device quality, Si thin film technologies will have a strong position in the PV technologies in the near future.

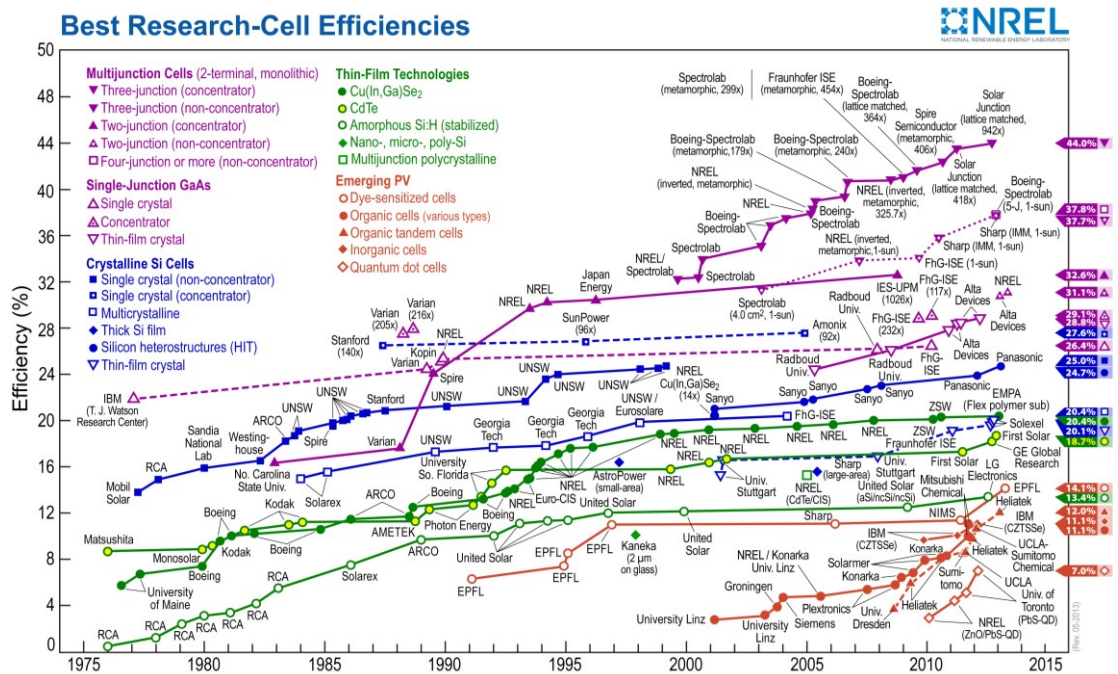


Fig 1-2 Highest confirmed efficiencies for $\geq 1\text{-cm}^2$ area cells fabricated using the different technologies [3]

1.3 Silicon Based Thin Film Solar Cells

In the last decade, the thin film solar cells attracted attention since they are very cost effective and offer an integrated production technology. As it is mentioned before the most common materials used for solar cell technology is silicon and its different forms, they are also used in thin film applications. Amorphous silicon should be called as hydrogenated amorphous silicon, a-Si:H, since amorphous silicon used for solar application is passivated by hydrogen. Silicon thin film solar cells can be deposited on large and cheap substrates such as glass, stainless steel or polymer, which makes it very suitable for high volume manufacturing. Additionally, number of process steps is remarkably low compared to crystalline silicon solar

cell production for which a series of production steps are required. For making modules, monolithic series connection can easily be made using laser-scribing technique during the production [5]. Another advantage is that very thin silicon layer of around 1 micro - meter is enough for thin film solar cell applications. When all advantages mentioned above are considered together, we see the potential of thin film systems in the PV applications.

1.3.1 Structure and Operation principle of thin film silicon solar cells

Working mechanism of the solar cells depends on optical interaction (absorption and carrier generation), carrier dynamics (life time, recombination) and transport of charge carriers. General solar cell process can be summarized in two basic steps:

- I. Generation of electron-hole pairs
- II. Separation of generated electrons and holes

First step is strongly related with energy of incoming light photon (E_{ph}) and band gap (E_g) value of the illuminated semiconductor. Band gap is defined as difference in energy level between the highest energy level of valance band (E_v) and lowest energy level of conduction band (E_c) of semiconductor [4]. When the energy of the incoming photon is higher or equal to E_g , photon can be absorbed and an electron from valance band can excite to the conduction band leaving a hole (positive charge) behind. However if the photon energy is lower than E_g , photon cannot be absorbed and it cannot generate electron-hole pairs, thus photon energy is not used to generate power. After creation of electron-hole pairs, it is important to separate them (second step) for the production of current to the external load. An effective separation can only be done by an electric field, which should be present internally for power extraction. Under the action of the electric field, electrons and holes move in reverse directions, and reach the opposite junction of the cell. . Fortunately this internal electric field is easily created by bringing, p-type doped material with the n-type doped one that forms so-called p-n junction. At the junction region, holes of p-type layer diffuse to the n-layer where they recombine with the electrons while, electrons of n-layer diffuse to p-layer and recombine with the holes there. Diffusion and recombination of carriers across the junction leave ionized atoms behind, that result in the formation of an electric field at the junction. However amorphous silicon (a-Si) and its phases such as μ c-Si and nc-Si are extremely defective materials, and when they are doped, the defect density of the materials becomes a few order of magnitude higher than the un-doped one [6]. Due to their higher defect density, diffusion length of the charge carriers is extremely low in these materials. Thus creating a p-n junction as in the case of crystalline silicon solar cells is not suitable for a-Si and its other phases. For this reason, a-Si based solar cells are fabricated using a p-i-n structure. The additional intrinsic layer (i-layer) placed between n-layer and p-layer enlarges the active region of the cell and thus increases the amount of light absorption. Internal electric field through i-layer assists the collection of excited electrons and holes [4].

Schematic of the p-i-n structure and charge transport mechanisms are shown in Fig 1-3. As mentioned above, p-layer contains mostly free holes while n-layer contains free electrons. Additional i-layer that used in this structure behaves as no free carrier except for the thermally generated ones. If p-layer put into contact with neutral i-layer, free holes at the junction region diffuse into i-layer and they leave negative charges behind. Similar to what happens in a single

p-n junction, these holes reach the n-side where they make recombination. The same process happens for the electrons diffusing from the n-side to the p-side. As a result, a negatively charged space charge region on the p-side, and a positively charged space charge region on the n-side are formed. The intrinsic layer between these two space charge regions acts as an uncharged dielectric material. An electric field is thus created across the intrinsic layer. In a p-i-n device, the excitation occurs in the intrinsic region, which is sometime called depletion region (i-layer).

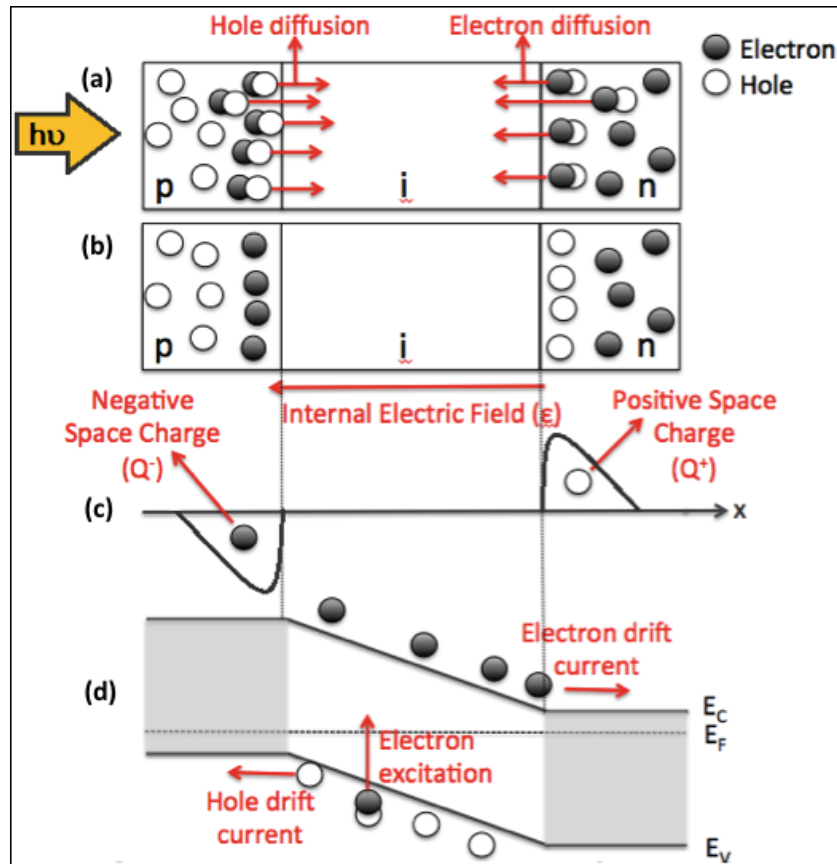


Fig 1-3 *p-i-n structure and charge transport mechanism*

When the light is absorbed by i-layer, electron-hole pair is generated. Electrons drift towards to n-layer, while holes drift towards the p-layer because of the internal electric field. Thus generated electrons and holes are separated. Quality of the i-layer is very important at this point. It should have high enough quality to let the carriers drift easily without trapping by a recombination center. The photo-generated carriers are collected through drift mechanism in a p-i-n junction structure rather than a diffusion process as in the conventional p-n junction structure. Thickness of the doped p- and n- layers is critical for an effective charge collection. Absorption that occurs in the doped p- and n- layers can not excite electrons in general, since these layers become highly defective with doping causing high recombination density. Excited electrons are trapped by these recombination centers before reaching the conduction band. Hence doped layers should be very thin to reduce the absorption by the doped layers. On the other hand, they should be thick enough to be able to form internal electric field. In some

cases, alloying them with suitable elements reduces the absorption in this layer. For example adding carbon (C) or oxygen (O) to silicon increases the band-gap of the material, thus more photon can pass through the material without being absorbed.

1.3.2 Configuration of thin film silicon solar cells

Typical structure of p-i-n type a-Si:H solar cell on glass substrate is illustrated in Fig 1-4 (a). Although there are different configurations, the presented one is the most common configuration used by the industry today. In this structure, p-layer is deposited as a window layer which means light enters into the cell from this layer first. As mentioned above, after the separation of the photo-generated carriers, holes drift towards p layer. Since the mobility of the free electrons are three times higher than the mobility of free holes and more electron-hole pairs are generated at the region close to window layer, p-type doped layer deposited as a window layer in the structure in order to collect holes faster and effectively. Additionally, p-layer has a band gap of 2.0 eV and both intrinsic and the n-layer has band gaps of 1.8 eV in general. The use of a wider band gap p-layer is desirable [7] in a-Si:H devices to reduce optical absorption in this layer.

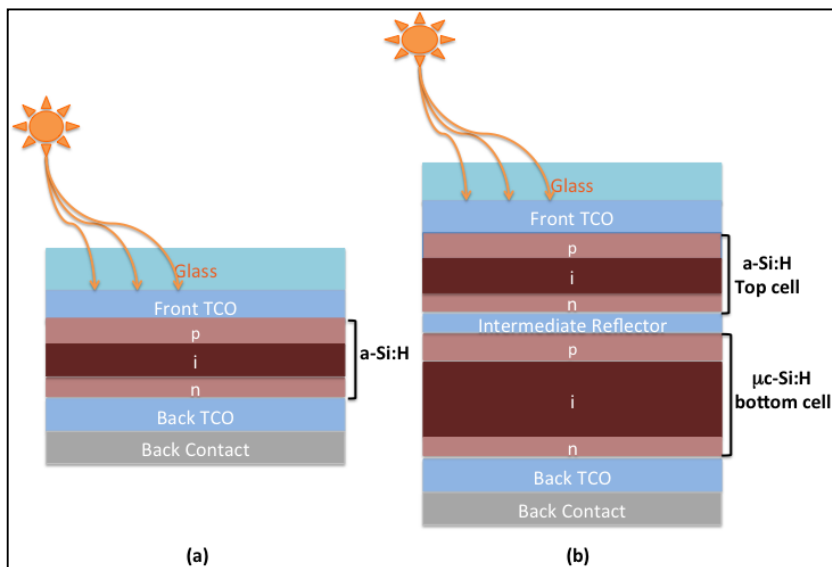


Fig 1-4 Basic configurations of p-i-n solar cells: (a) a-Si:H single junction solar cell (b) Micromorph (a-Si:H/ μ c-Si:H) tandem solar cell

In order to collect the separated photo-generated electrons and holes, metallic contacts are needed. According to the general deposition sequence, first Transparent Conductive Oxide (TCO) layer is deposited as a front contact on glass substrate. This first layer should be as transparent as possible and randomly textured to enhance the scattering of light at the interface. The scattering enhances light absorption inside the solar cell. After front contact, silicon-based layers, p-layer, i-layer and n-layer are sequentially deposited on the TCO. Afterwards, back TCO layer with the same properties as the front contact is deposited. As a final layer metal contact is deposited onto the TCO layer.

It is well known fact that, when a typical a-Si:H solar cell is exposed to sunlight, density of unpassivated dangling bonds increases. This is called as light induced degradation (LID) or Staebler - Wronski effect [8]. Dangling bonds that are created in this way cause additional recombination centers through the active i-layer. Thus, drift length of the photo-generated carriers decreases and recombination probability increases. As a result, the conversion efficiency of a a-Si:H p-i-n solar cell degrades dramatically under light illumination in time. The conversion efficiency of a Si thin film solar cell can be improved by employing more than one junction called tandem solar cell. In this case, the bottom cell is made of a microcrystalline Si thin film which is less affected by the light induced degradation effect [9]. In Fig 1-4 (b) microcrystalline and amorphous silicon (micro-morph) tandem structure is shown. As a top cell thin a-Si:H p-i-n structure is deposited and since the band gap of $\mu\text{c-Si:H}$ is lower than that of a-Si:H. Band gap of amorphous silicon is around 1.75 eV, whereas E_g of highly microcrystalline silicon is around 1.1 eV. Compared to a-Si:H, $\mu\text{c-Si:H}$ absorbs light coming from a wider spectral range as it is shown in Fig 1-5 [10]. Therefore, such multi-junction cell structure takes advantage of utilizing a wider range of the solar spectrum compared to a single-junction cell and helps to improve light trapping.

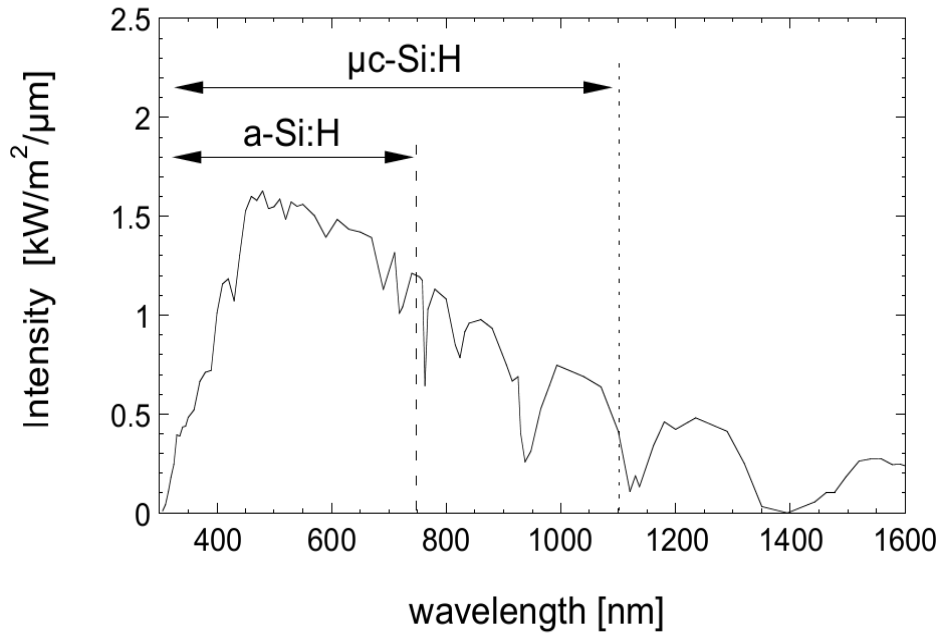


Fig 1-5 The spectral ranges which are absorbed by a-Si:H and $\mu\text{c-Si:H}$, respectively [10]

Band gap engineering is the process of controlling or altering the band gap of a material by controlling the composition of certain semiconductor. In this case, it is possible to control the bandgap of the silicon material by changing the crystallinity. Spectral response of the material can be controlled by this approach. Thus not only $\mu\text{c-Si:H}$ but also nc-Si:H films can be used in solar cell applications. According to the solar cell efficiency tables- version 41, a-Si/nc-Si/nc-Si triple-junction solar cell efficiency measured under the global AM1.5 spectrum (1000W/m^2) by national renewable energy laboratory (NREL) is 13.4% [3]. Nanocrystalline silicon is also very important material for next generation solar cells which are expected to utilize the quantum size effect occurring in the nc-Si quantum dots (QDs) fabricated in an appropriate matrix and increase the device efficiency significantly.

1.4 Motivation of the Work

As discussed above, hydrogenated microcrystalline and nanocrystalline silicon thin films with tunable optical band gap are important because of spectral response enhancement and less LID. Due to their band gaps, nc-Si:H and μ c-Si:H thin films are used in Si tandem solar cell applications to utilize wider range of the solar energy spectrum. The degree of crystallization, and the kinetics of this process should be understood and controlled for this application. This study is focused on the analysis of the crystallization of the intrinsic amorphous silicon produced by plasma enhanced chemical vapor deposition (PECVD) technique, e-beam evaporation and crystal formation in silicon rich silicon oxide (SRO) matrix deposited by magnetron sputtering technique. We obtain different crystal fraction by altering the deposition parameters such as deposition power and pressure and substrate temperature etc. Optical and electrical properties of these samples are studied using different characterization tools.

The most efficient solar cells are achieved when an intrinsic layer is deposited near the μ c-Si:H / a-Si:H transition. However, phase transition from amorphous to crystalline is extremely important and complex subject needed to be investigated. In that manner, a systematic study of the crystal formation deposited by different techniques in different matrix is essential for silicon thin films and next generation solar cell applications.

In addition to the introduction and the conclusions, this thesis is divided into four chapters;

- ❖ In Chapter 2, deposition systems and main characterization methods used throughout this work with their physical background are described.
- ❖ Chapter 3 is focused on the analysis of crystallization of the amorphous silicon deposited with different techniques and crystal formation in SRSO matrix. In parallel, structural and optical properties of the deposited layers are also discussed.
- ❖ In our PECVD system, one of the chambers is equipped with an Inductively Coupled Plasma (ICP) system that provided us a unique opportunity to study this plasma technique which is different from conventional capacitively coupled plasma systems. Especially, samples deposited with ICP-CVD show interesting structural peculiarities, Chapter 4 is devoted to the study of these structures.
- ❖ Lastly in Chapter 5, opto-electronic properties of ICP-CVD deposited a-Si:H and nc-Si:H films are investigated in detail via different characterization methods.

CHAPTER 2

EXPERIMENTAL

2.1 Deposition Techniques

Deposition processes used for the preparation of thin films are very important due to their effects on optical, electrical and structural properties of the films. Especially, growth mechanism and nucleation during production are highly affected by chosen deposition method. For Si thin film fabrication, it is possible to classify deposition techniques according to their primary sources. There are mainly two group of methods used for fabrication; Physical Vapor Deposition (PVD) technique in which solid phase target is used as a source and Chemical Vapor Deposition (CVD) technique in which gas phase source is used for film growth. Methods such as thermal or electron beam evaporation, magnetron or ion-beam sputtering can be an example for the PVD technique. CVD technique is more commonly used technique to fabricate Si-thin films in different phases. Plasma enhanced-CVD, low pressure-CVD, hot wire-CVD, atmospheric pressure-CVD are the most popular CVD techniques. In this thesis, PE-CVD, magnetron sputtering and electron-beam evaporation techniques are used to produce Si-thin films in different phases to be able to compare films deposited by different techniques. Plasma-assisted deposition methods such as PECVD and sputtering, include two types of variables; plasma related variables such as electron-ion densities, energies, etc. and process related variables such as pressure, temperature, etc [11]. The effects of these variables on the film properties are also investigated in this work.

2.1.1 Plasma Enhanced Chemical Vapor Deposition (PECVD)

PECVD is plasma based chemical vapor deposition technique. PECVD has received particular attention since it provides different microstructure fabrication, great variety of film compositions, high deposition rate by comparison with PVD and uniform coating with high purity on distinctive substrate shapes. The most significant advantage of PECVD is being low temperature deposition process (200 – 250 °C), which can provide the opportunity to use variation of low cost substrates.

Reaction	General equation	Example
<i>Reactions with electrons</i>		
Ionization	$e + A \rightarrow A^+ + 2e$	$e + N_2 \rightarrow N_2^+ + 2e$
Excitation	$e + A \rightarrow A^* + e$	$e + O_2 \rightarrow O_2^* + e$
Dissociation	$e + AB \rightarrow e + A + B$	$e + SiH_4 \rightarrow e + SiH_3 + H$
Dissociative ionization	$e + AB \rightarrow 2e + A^+ + B$	$e + TiCl_4 \rightarrow 2e + TiCl_3^+ + Cl$
Dissociative attachment	$e + AB \rightarrow A^- + B$	$e + SiCl_4 \rightarrow Cl^- + SiCl_3$
Three-body recombination	$e + A^+ + B \rightarrow A + B$	$e + H^+ + CH_4 \rightarrow H + CH_4$
Radiative recombination	$e + A^+ \rightarrow A + h\nu$	$e + Ar^+ \rightarrow Ar + h\nu$
<i>Reactions between heavy species</i>		
Charge exchange	$A^+ + B \rightarrow A + B^+$	$N_2^+(fast) + N_2(slow) \rightarrow N_2(fast) + N_2^+(slow)$
Penning ionization	$A^+ + B \rightarrow A + B^+ + e$	$He^+ + O_2 \rightarrow He + O_2^+ + e$
Ionization by interchange	$A^+ + BC \rightarrow AB^+ + C$	$N^+ + O_2 \rightarrow NO^+ + O$
Combination	$A + B \rightarrow AB$ $AB + CD \rightarrow AC + BD$	$2SiH_3 \rightarrow Si_2H_6$ $SiH_2 + O_2 \rightarrow SiO + H_2O$
<i>Heterogeneous interactions (with surfaces)</i>		
Adsorption	$R_g + S \rightarrow R_s$	$CH_2 + S \rightarrow (CH_2)_s$
Metastable deexcitation	$A^* + S \rightarrow A + S$	$N_2^* + S \rightarrow N_2 + S$
Sputtering	$A^+ + B_s \rightarrow A + B$	$Ar^+ + H_s \rightarrow Ar + H$
Secondary electron emission	$A^+ + S \rightarrow S + e$	$O^+ + S \rightarrow S + e$

Fig 2-1 Reactions occur in plasma environment [12]

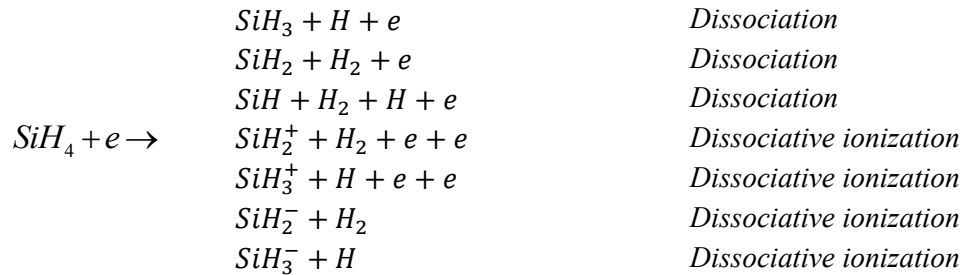
PECVD is a complex method as it contains lots of interactions such as dissociation, ionization, dissociative ionization, excitation-relaxation, recombination (Fig 2-1). Additionally, chemical reactions taking place in a PECVD process can be classified into two different groups; gas-phase reactions in the plasma and substrate-surface reactions, as it is also shown in Fig 2-1.

Plasma can be described as an ionized gas that includes mixture of electrons, neutral atoms, ions, free radicals and molecules at many different levels of excitation [13]. For plasma generation, sufficient voltage is applied in a chamber filled with related gases. Ionized gas is generated using a high electric field or magnetic field. This is known as cold plasma [14] which has not thermal equilibrium in between gas (T_g) and electron (T_e) temperature ($T_e > T_g$). Under this non-equilibrium condition, chemical reactions initiation occurs by collisions with the highly energetic electrons and excited species react with each other. This is the reason why the processing temperature is much lower than conventional thermal CVD. In thermal CVD, films are deposited through thermochemical surface reactions and high temperature (500 - 800 °C) is needed to promote deposition reaction (to provide atoms with sufficient mobility). Plasma can also be called as glow discharge, since energy transfer from electron to related gas molecules during the collision, cause a radiation in visible part of the spectrum. Thin film formation process in a plasma system can be summarized mainly as follows;

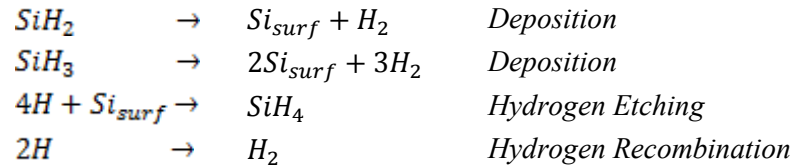
- i. Diffusion of source gas,
- ii. Inelastic electron impact process for dissociation of source gas,
- iii. Chemical reactions in gas phase and diffusion of the reactive species to the substrate surface,
- iv. Adsorption of reactive species on the substrate surface and the surface reaction of these species,
- v. Surface diffusion of the species. Island nucleation and merging islands into a continuous thin film,
- vi. Desorption of by products and transport of them from the growth region.

In this work, hydrogen (H_2) diluted silane (SiH_4) gas mixture is used as a source gas for Si thin film deposition. The formation of Si thin films by PECVD contains mainly four step processes.

Primarily, first reaction takes place in between electrons and feed-gas H_2 diluted SiH_4 , which is dissociated mainly by electron excitation. As a result of this step various positive ions, negative ions, neutral radicals, neutral molecules and electrons are generated. For instance, following reactions can be observed in this step;



In the second step, secondary reaction in between molecule and ion or molecule and free radicals occurs in the plasma. As a result of these secondary reactions, reactive species are generated. Among them neutral species transport to the substrate surface via diffusion or drifting, positive ions are accelerated and cause ion bombardment through the substrate surface. In the third step, reactive species interact with surface of the substrate and also some of them adsorb on the surface. As a last step, finally film formation can be observed with the incorporation of the species or reaction products of them. Also as an example of surface interactions one can see following reactions;



Where Si_{surf} refers to deposited Si-layer. Dissociation of molecules can also cause some desorption from the surface.

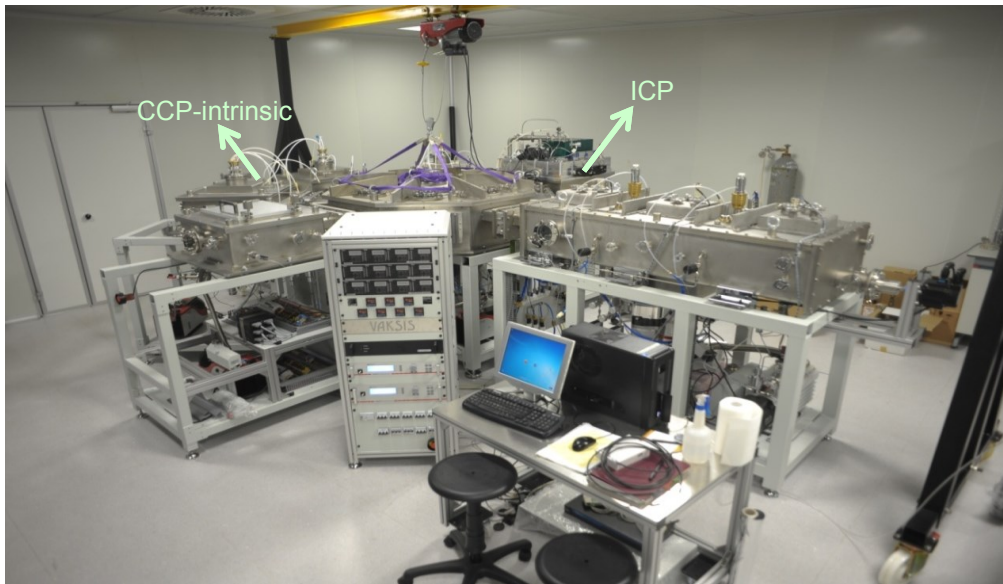


Fig 2-2 Picture of multi-chamber PECVD system in GUNAM

In this work a multi-chamber PECVD system and radiofrequency (RF) plasma sources operated with frequency of 13.56 MHz are used (Fig 2-2). In general, RF powered plasmas have been categorized according to their excitation mode [15, 16];

- i. Capacitively coupled plasma excited by electric field (E-field)
- ii. Inductively coupled plasma excited by induction field (H-field)

The ionization is started by an external electromagnetic field; therefore, different electromagnetic boundaries will determine different ionization mechanisms. This is the basis of the concepts of capacitively and inductively coupled plasmas. In the scope of this thesis, intrinsic silicon thin film is deposited using both E-field and H-field excitation modes. To understand the differences, advantages and disadvantages of these RF plasma types, we examine them more closely in the following sections.

2.1.1.1 Capacitively Coupled Plasma (CCP)-CVD

Schematic illustration of conventional CCP-CVD system in cluster PECVD, used in this work, is shown in Fig 2-3. Reactor contains two capacitive configurations of electrodes parallel to each other; one of them is grounded and the other one is connected to the RF power supply (typically at frequency 13.56 MHz). The distance between two parallel electrodes is significantly important parameter that affects the film quality since it determines the travel distance of radicals before arriving the surface. Typical electrode spacing is around 1 to 5 cm for uniform and high quality Si-thin films. The gap between the electrodes is filled with a gas. Substrate is placed on the top of grounded electrode. Substrate heater unit is placed bottom of grounded electrode. Gas inlet and exhaust for reacted or un-reacted gases are on the top of the chamber. The plasma formed in this configuration is called as capacitively coupled plasma.

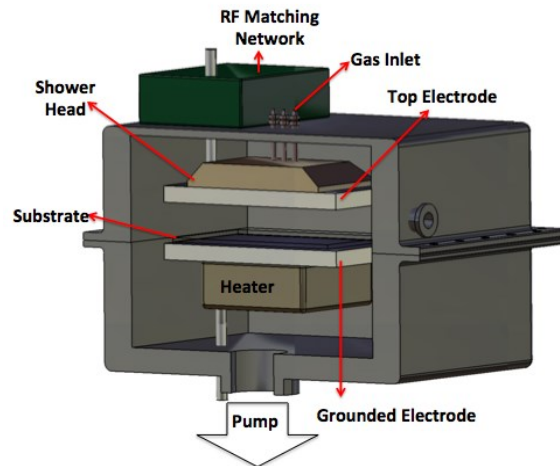


Fig 2-3 Schematic illustration of conventional CCP-CVD system

When the chamber is full with feed-gases and sufficient RF power is applied to the top electrode, electric field is generated in between two electrodes. Atoms and molecules are ionized and release electrons due to electric field and as a result plasma is ignited.

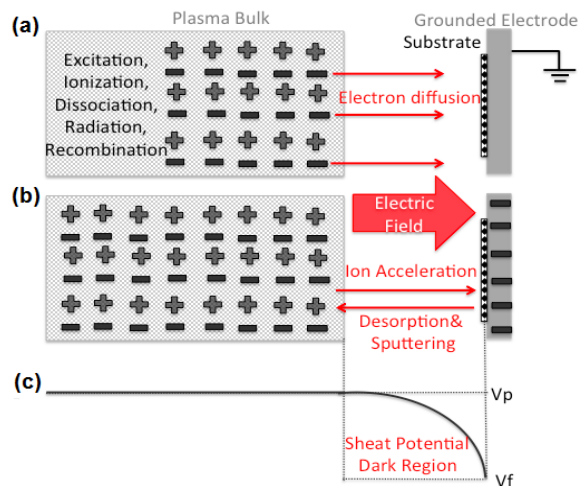


Fig 2-4 Electron diffusion from bulk plasma to substrate (a), creation of sheath voltage (b), potential distribution in discharge (c)

Electrons are significantly lighter and more energetic than the ions, thus in most of the plasma models ions are assumed as a stationary. Additionally, the ions are not influenced by the electric fields and move randomly within the plasma. Since electrons move much faster than ions, they can escape easily from the bulk plasma leaving behind positively charged plasma. Hence, anything close to the plasma such as electrodes and walls are charged negatively. In Fig 2-4 (a) electron diffusion from bulk plasma to substrate is illustrated. Although, plasma potential is always positive and all processing plasma have the uniform plasma potential, negatively charged electrodes repel the electrons and attract positive ions, and thus potential difference between plasma and electrode is created (Fig 2-4 (b)). Resulting potential difference between the electrodes and the plasma creates an electric field region at the edge of the plasma, which is called as a sheath region. Sheath region accelerates the positive ions towards to substrate surface with a high energy. Surface reactions occur due to the high-energy ion

bombardment towards the substrate. Fig 2-4 (c) shows the created potential distribution in glow discharge for the case of equal electrodes area where V_p is plasma potential. The region in between electrode and bulk plasma is so-called as a sheath potential or dark region with less luminosity than the bulk plasma owing to the potential drops. In this region, the density and energy of the free electrons is lower, consequently, less collisions occur and less photons are emitted.

2.1.1.2 Inductively Coupled Plasma (ICP)-CVD

Inductively coupled plasma is a promising and widely used high-density plasma source in which the energy is supplied by electric current produced by electromagnetic induction. ICP provides high electron densities, such as 10^{12} cm^{-3} , at low ion energies [13]. In 1869 Hittorf observed that evacuated chamber which is surrounded by induction coil and filled with gas can glow discharge, if induction coils has enough current frequency. Later, again Hittorf reported that main reason of discharge is not electric field but magnetic field of induction coils.

The inductive plasma generation can be explained using Maxwell's equations for electric and magnetic fields; \vec{E} and \vec{B} . In general, ICP is generated by locating a spiral or helical induction coils adjacent to or inside the discharge region. According to the Ampere's law, time varying magnetic field (\mathbf{B} -field) is created by a time varying RF current (\mathbf{J}_c) passes through these induction coils (Ampere's Law);

$$\nabla \times \mathbf{B} = \mu_0 \mathbf{J}_c + \mu_0 \epsilon_0 \frac{\partial \mathbf{E}}{\partial t} = \mathbf{J}_T \quad (\text{Eqn. 2-1})$$

where \mathbf{B} is magnetic field, \mathbf{J}_c conduction current, second term of the equation is displacement current and \mathbf{J}_T is total current (conduction current + displacement current).

In Fig 2-5 (a), it is possible to see cross-sectional view of ICP chamber. Direction of the current passing through the induction coils and created magnetic field are also shown in the Fig 2-5 (b). Magnetic field should be parallel to the chamber axis. Thus time rate of change of the magnetic field creates an induced electric field and associated induced plasma current (J_p) from Faraday's law;

$$\nabla \times \mathbf{E} = -\frac{\partial \mathbf{B}}{\partial t} \quad (\text{Eqn. 2-2})$$

This induces electric field that causes an acceleration of the electrons by transferring energy within the skin depth layer of thickness δ near the plasma surface. Skin depth can be defined as the layer through which induced RF current is passed and is given by expression;

$$\delta_s = \sqrt{\frac{2}{\mu \omega \sigma}} \quad (\text{Eqn. 2-3})$$

where μ is permeability of the medium, ω is plasma frequency and σ is plasma conductivity. The induced plasma current direction is the opposite to the current flowing through induction coils.

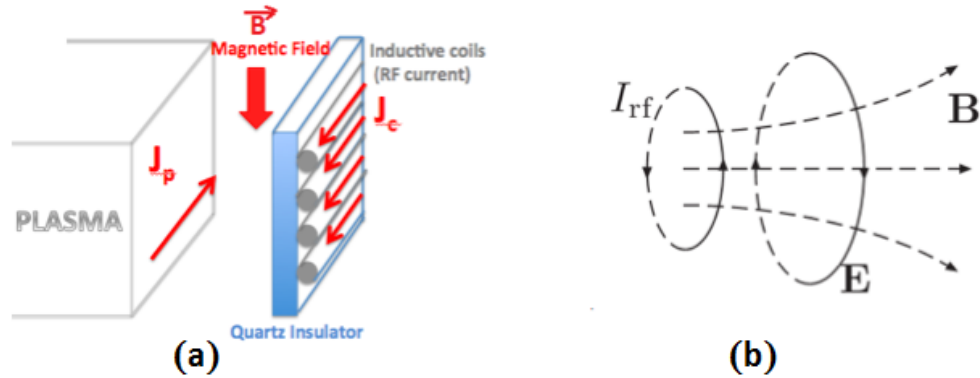


Fig 2-5 Cross-sectional view of ICP-CVD chamber (a), relative directions of E-field, B-field and induced current (I_{rf}) (b)

Main advantage of the ICP-CVD system is to be able to control the energy of ions reaching the film surface by voltage source [17]. In a CCP-CVD there should be large RF potential drop across the plasma sheath to form space charge region and establish the current flow. This large potential drop is also the reason of striking ions to substrate with very high energies and it causes the damaged the surface of deposited films. Thus, ICP-CVD system can help to reduce the ion bombardment and increase the film quality.

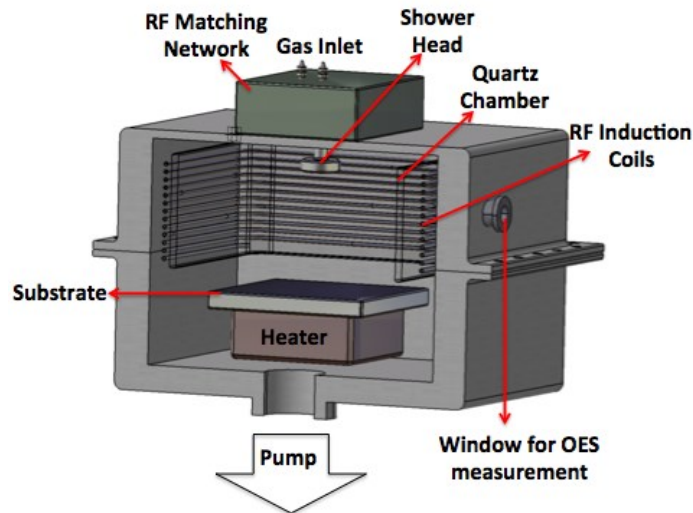


Fig 2-6 Schematic diagram of ICP-CVD chamber

The schematic diagram of ICP chamber used in this thesis is illustrated in Fig 2-6. ICP-CVD reactor is built of stainless steel. The plasma is generated by a RF frequency (13.56 MHz) power source that has a capacity of 5 kW. It is connected to the copper coils that surround the chamber outside a quartz tube. The 25x25 cm² holder is placed on the heater. The source gases enter the chamber from the top and after deposition residuals are pumped out from bottom of the chamber.

2.1.2 Magnetron Sputtering

In CVD techniques, gas phase-molecular species react at a film surface for the formation of the film, however in PVD techniques, films are deposited from single atoms or small clusters and no surface reaction takes place for the film formation. Sputtering is the one of the most common PVD techniques, which provides excellent film uniformity, surface smoothness, thickness control and surface adhesion. Sputter process is basically a kinetic process including momentum exchange. Energetic and non-radioactive incident ions bombard surface of the target to create the ejection of atoms. Ejection process occurs after momentum and energy are transferred from energetic ions to surface atoms of target. Afterwards, formation of the films occurs with condensation of sputtered atoms on the substrate surface. Secondary electrons are emitted from target due to the ion bombardment and they are very significant to maintain the discharge. Number of ejected atoms per incident ions is called sputter yield and it is related to the energy and incoming angle of the ions [18]. Ar^+ , which is generated after the ionization of Ar gas, is the most frequently used non-reactive gas ions to increase the sputter yield.

In general deposition rates of sputtering process are lower than the other PVD technique since the significant part of the ions energy are converted to heat. Fortunately, high deposition rates are reachable with high ion current density in some particular sputtering geometries like magnetron sputtering. In magnetron sputtering configurations, additional magnetrons create magnetic field parallel to the target surface to keep secondary electrons in the plasma region. Created magnetic field and electric field define the electrons path and keep them close to surface of the target. Generally, target is defined as cathode (negative terminal) in this magnetron-sputtering configuration.

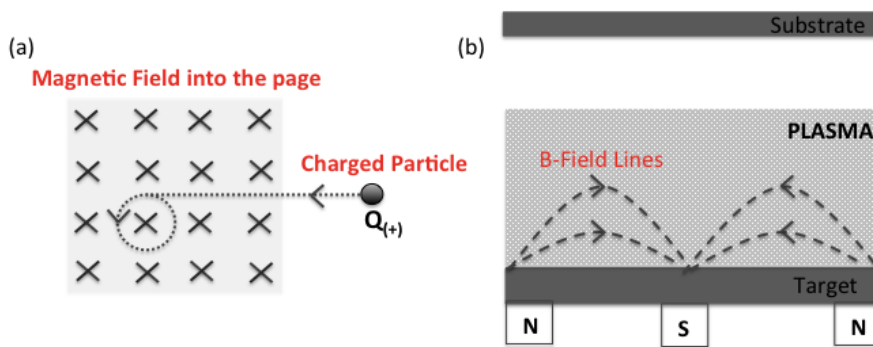


Fig 2-7 Particle movement in magnetic field (a), B-field lines produced by magnetrons (b)

Electromagnetic force on a moving charged particle in magnetic field is described by Lorentz force (**F**);

$$F = qV \times B \quad (\text{Eqn. 2-4})$$

where **B** is the magnetic field, q is the charge and **v** is the velocity. When the charge movement is perpendicular to magnetic field direction, charge continue to move in a helical or circular path around the magnetic field lines as it is shown in Fig 2-7 (a). Hence, the path length of the charged particle and secondary electrons in the plasma are increasing due to the helical motion

and this causes a higher collision probability with gas atoms. More collisions mean more ionizations and excitations, which create denser plasma and increase deposition rate. Additionally, since secondary electrons are trapped close to the target, they cannot bombard the substrate surface [19]. Fig 2-7 (b) shows the B-field lines created by magnetrons with in the plasma, which causes the electron trapping around the target.

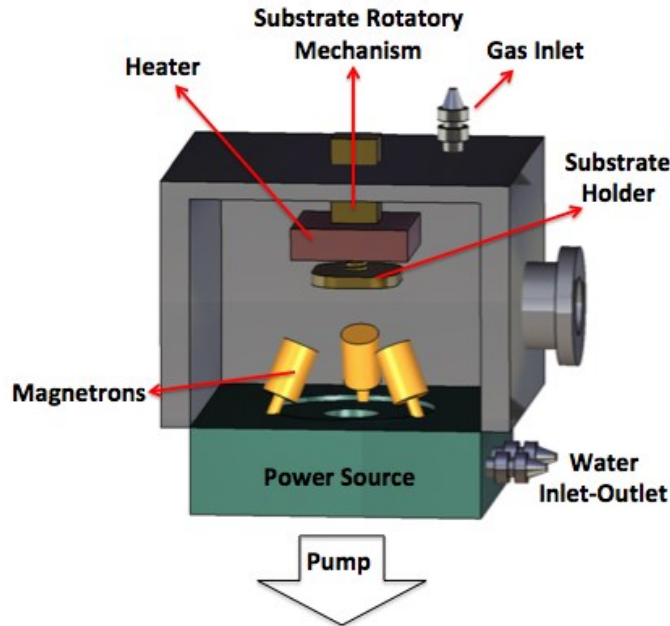


Fig 2-8 Schematic diagram of magnetron sputtering system

In Fig 2-8, one can see the schematic of the magnetron sputtering system used in this work. There are three targets, which provide an opportunity to deposit complex structures with more than one component. Both RF and DC sources can be used as a power source depending on the target material. While DC sources are used only for conductive target material, RF sources can be used for both conductive and non-conductive target material. Electric field between substrate and target is created by applying RF or DC power to the target and magnetrons that are placed bottom of the target in order to generate non-uniform magnetic field parallel to the target surface. Electric and magnetic field create $\mathbf{E} \times \mathbf{B}$ drift trapping effect and path for drifting of secondary electrons. These electrons are trapped in the plasma and move perpendicularly to both E-field and B-Field.

In this study, magnetron-sputtering system is used to fabricate nanocrystalline silicon (nc-Si) structures in silicon rich silicon oxide (SRO) matrix. 99.9% pure Si and SiO₂ targets and 99.99% pure Ar as the process gas are used. DC power is applied to the Si target while the RF power is applied to the SiO₂ target. To observe the nanocrystal formation, thermal annealing is done after deposition of the magnetron sputtered thin films.

2.1.3 Electron Beam Evaporation

As mentioned above, PVD techniques can be divided into two main categories as evaporation and sputtering. Basically, evaporation systems include a heating source such as electron beam,

laser beam, thermally heated crucible, etc. for vaporizing materials. Evaporation source is chosen according to the material. In this thesis electron beam evaporation technique is used to deposit Si thin film in different phase. The major advantages of this technique are, wide range of evaporation rate control and using cooled crucible to eliminate film contamination, which originates from the reaction in between evaporant and crucible.

Electron beam sources are generally called as electron beam guns and divided into two groups: plasma guns and thermionic guns. Here thermionic gun is used as a beam source. Energetic electron beams are produced by heating of tungsten filament and directed through the source material placed in crucible. Electromagnetic field guides the electrons while focusing and directing towards the source material, and then energy of the electrons is transferred and evaporates the material.

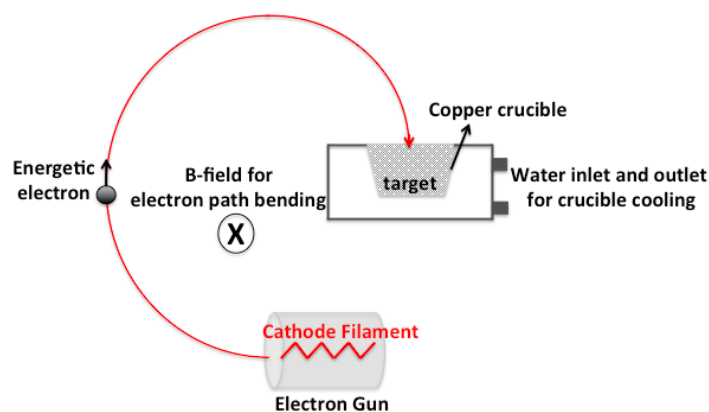


Fig 2-9 Schematic representation of electron beam evaporation mechanism

The filament is heated by current passing through, thus it is possible to control the energetic electron beam density and deposition rate by altering the current. After the evaporation of the target material, thin film formation takes place through the nucleation of single atoms on the substrate surface. If the time of atom migration on the surface is enough to meet another atom before re-evaporation, these atoms merge to form an island. As the energy required for evaporation of one of the atoms of this pair is considerably higher than that needed for an isolated atom, stable islands start to form on the surface. These islands combine and lastly the continuous growth of thin film is observed (Fig 2-9).

Silicon pieces are used as a target for Si-thin film deposition by electron beam evaporation. After film growth, a-Si thin film is crystallized by thermal annealing and polycrystalline silicon film with a size of few microns grain is obtained [20]. This process is called solid phase crystallization (SPC) and it is a low-cost way to produce polycrystalline structure. Rapid thermal annealing (RTA) method is used for annealing process. RTA system consists of halogen lamps, which can be heated up high temperature like 1100⁰C, rapidly.

2.2 Plasma Diagnostics

Plasma diagnostics measurements are very useful to obtain better knowledge about plasma conditions and controlling deposition process. Basic plasma properties such as type of the species in, their densities and energies, electron-ion temperature, current density, electric field and plasma potential are the main parameters, which determine quality of the deposited films. They should be determined and controlled accurately during the deposition for a reliable and reproducible film fabrication. In general, these process and plasma parameters can be determined using various plasma diagnostic techniques including mass spectroscopy, electrical probe and optical spectroscopy. Neutral species and ions in the plasma can be determined by using mass spectroscopy. Plasma density and electrons energy distribution can be measured by an electrical probe method. The plasma species and its dynamics can be monitored using four different methods. Optical emission spectroscopy examine the emitted light from the discharge; optical absorption spectroscopy analyses the absorbed energy from radiated light into the plasma; laser induced fluorescence spectroscopy analyses fluorescence light emitted in relaxation transition after laser excitation of atoms or molecules in the plasma and coherent anti-stokes Raman spectroscopy analyses rotational energy distribution for molecules from the shape of the spectrum. Regrettably, information obtained by a single diagnostic tool is usually limited making it necessary to combine more than one method to reach conclusive results [14].

Table 2-1 Detectable species with various optical spectroscopy methods

Method	Detectable Species
Optical Emission Spectroscopy (OES)	$H_{\alpha}^*, H_{\beta}^*, Si^*, SiH^*$
Optical Absorption Spectroscopy (OAS)	SiH, SiH_2, SiH_4
Laser-Induces Fluorescence (LIF)	Si, SiH
Coherent Anti-Stokes Raman Spectroscopy (CARS)	SiH_2, SiH_4

Table 2-1 shows detectable species of the H₂-diluted SiH₄ plasma using optical spectroscopy methods mentioned above. Here in this study we study the optical spectroscopy technique to analyze both capacitively and inductively coupled highly H₂-diluted SiH₄ plasma. However, OES of the silane glow discharge is expected to be a useful tool for investigating the behavior of only reactive species [21]. $H_{\alpha}^*, H_{\beta}^*, Si^*, SiH^*$ represent the excited reactive species, which are mainly observed in the OES of H₂-diluted SiH₄ plasma.

2.2.1 Optical Emission Spectroscopy

Optical Emission spectroscopy (OES) is non-invasive diagnostic technique that analyzes the emitted light from the plasma in the absence of any external optical excitations [22]. As it does not interfere with the plasma itself, information on the undisturbed plasma can be obtained from this in-situ diagnostic tool. However, additional window is needed in deposition chamber for plasma monitoring and only semi-quantitative information can be obtained with this method. Inelastic collisions in between high-speed energetic electrons and gas phase species cause excitation of the atoms to higher quantized energy levels in plasma. Spontaneous photon emission is observed when excited atoms decay to lower energy states. These transitions

generally occur in the visible and ultraviolet region of the electromagnetic spectrum. The spectrum of the light emitted by the plasma is dispersed and its intensity is measured as a function of the wavelength. These spectra provide information about the type and number of the some excited particles in the plasma.

The formation of the Si thin films in evacuated plasma environments is much affected by the concentrations of different radical species in the discharge. OES is used to find out relative amount of depositing species of silicon under distinctive processing conditions. Fig 2-10 shows commonly used emission lines to analyze highly H₂-diluted SiH₄ plasma. As it is shown in table the detectable reactive species of related plasma are $H\alpha^*$, $H\beta^*$, Si^* , SiH^* , corresponding peak positions of the these species in OES spectrum are as follows; 656nm, 486nm, 288nm and 412nm, respectively [23]. Intensity changes of these peaks are related with decomposition ratio of plasma gases and depletion of radicals. Therefore effect of deposition parameters such as pressure, power, temperature and gas flow on plasma diagnostics can be determined by analyzing mentioned peaks, since deposition parameters have significant effect on decomposition and depletion of the radicals.

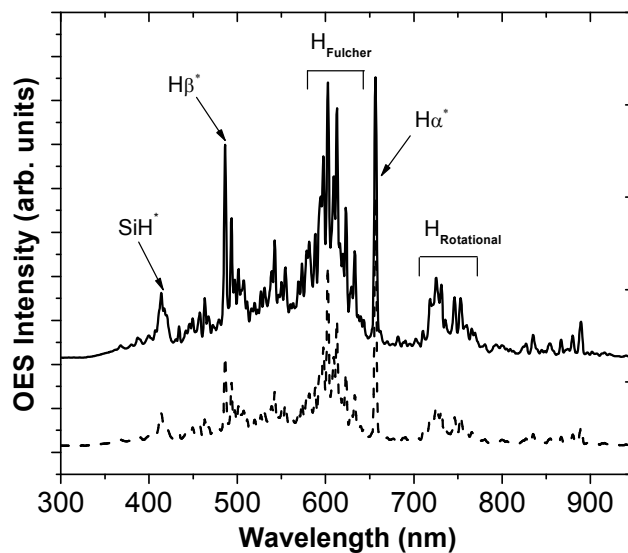


Fig 2-10 Typical OES spectrum of H₂ diluted SiH₄ plasma

2.3 Material Characterization

2.3.1 Spectroscopic Ellipsometry

Spectroscopic ellipsometry (SE) is a powerful and non-destructive tool to evaluate a wide range of thin film properties such as thickness, crystallinity, composition, size, roughness, optical and dielectric constants, band-gap etc.[24]. SE measurement technique is based on the change of the polarization state of light after reflection or transmission from the surface of the sample at non-normal incidence. Fig 2-11 shows the measurement principle of SE, where sample is irradiated by linearly polarized light and polarization of the light becomes elliptical after reflection from the sample surface.

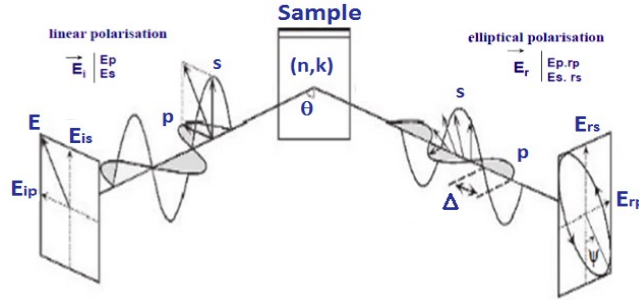


Fig 2-11 Measurement principle of SE [25]

Upon light reflection on sample p- (parallel to plane of incidence) and s-(perpendicular to plane of incidence) polarizations undergo different alterations in phase and amplitude. SE basically measures two parameters psi (ψ) and delta (Δ), which describe the amplitude ratio and phase difference in between p- and s- polarizations, respectively (Fig 2-12). These parameters are measured as a function of wavelength or energy of the light. The change in polarization state (ρ) is generally defined with ψ , Δ or ratio of Fresnel reflection coefficients R_p and R_s for p- and s-polarized light [26].

$$\rho = \tan(\psi)e^{i\Delta} = \frac{R_p}{R_s} \quad (\text{Eqn. 2-5})$$

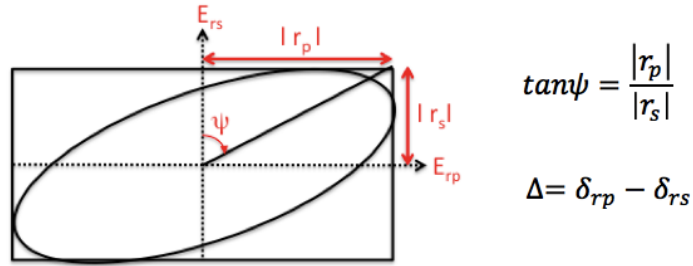


Fig 2-12 Elliptically polarized light and definition of Δ and Ψ

SE provides the determination of the optical constants; refractive index (n) and extinction coefficient (k). By using n , k values it is possible to determine complex refractive index (N) which describes changes in light wave caused by light-material interaction and complex dielectric function (ϵ) which describes material's response to electromagnetic radiation.

$$N = n + ik \quad (\text{Eqn. 2-6})$$

From Maxwell's equation, complex dielectric function of conductors can be defined as;

$$\epsilon = N^2 \quad \text{where} \quad \epsilon = \epsilon_r + i\epsilon_i \quad (\text{Eqn. 2-7})$$

$$\epsilon_r + i\epsilon_i = (n + ik)^2$$

$$\epsilon_i = 2nk(\text{imaginary part}) \quad (\text{Eqn. 2-8})$$

$$\varepsilon_r = n^2 - k^2 (\text{real part}) \quad (\text{Eqn. 2-9})$$

These real and imaginary parts of dielectric function represent the in-phase (ε_r) and out-of-phase (ε_i) component of frequency response of the material. In-phase component results in dispersion while out-of-phase component results in enhancement of absorption. On the other hand, there are some constraints imposed by the material studied. Since light scattering, surface roughness reduces the intensity of the reflected light; SE measurement becomes difficult for the rough [26]. For a reliable measurement, the surface roughness of the sample should be very small. The incidence angle at which measurement is performed is another critical parameter, for semiconductor characterization typical angle range lies between 70-80°.

As an illumination source Xenon lamp is used. First, the light is converted to collimated beam by collimator, then polarizer makes the light linearly polarized. After the reflection of light from the film structure, polarization state changes depending on the thickness and refractive index of layer and analyzer identifies the changed polarization state of light in terms of ψ and Δ . However, SE measurement is an indirect characterization technique, which requires fitting to measured ψ and Δ spectra, dielectric function modeling and construct an optical model for data analysis. There are different dielectric function models for fitting and proper model is chosen according to the optical properties (absorption, transmission, reflection, etc.) of the sample. For instance, in transparent region ($k=0$) Cauchy or Sellmeier model is commonly used, however if there is free carrier absorption Drude model is preferred. In addition, there are various models such as Lorentz model, Tauc-Lorentz model, model dielectric function, etc that can be applied to some specific material system. Moreover, complex refractive indices of surface roughness and interface layers can be determined by using Bruggmen Effective Medium Approximation (BEMA). An important advantage of using BEMA is to be able to determine the volume fractions in composite materials [24].

In the scope of this thesis, SE is used to determine the volume fractions of existing subspecies in nc-Si in SRSO matrix systems and the change in the crystallization with deposition parameters using mostly BEMA and Tauc-Lorentz models.

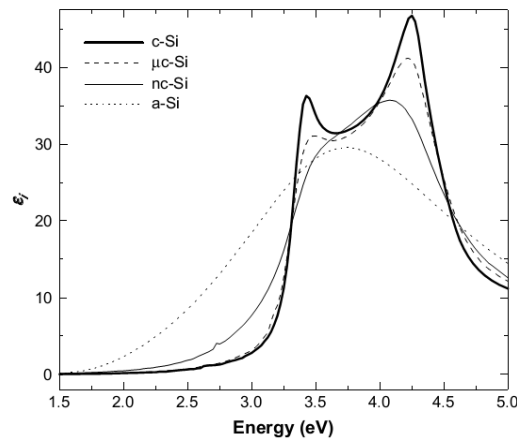


Fig 2-13 Spectroscopic Ellipsometry reference data of the imaginary part of dielectric function ε_i for single-crystalline (c-Si), micro-crystalline (μ c-Si), nano-crystalline (nc-Si) and amorphous (a-Si) silicon [27]

In determining the crystalline volume fraction of the silicon thin film samples, imaginary part of dielectric function is very important. Fig 2-13 illustrates the way of observing phase transition from amorphous to single-crystalline silicon using ϵ_i . The variation of optical constants with crystallization can be also analyzed using SE measurements.

2.3.2 Raman Spectroscopy

Raman spectroscopy (RS) is a powerful, fast and non-destructive tool that provides information about vibrational, rotational, and other low-frequency modes in a sample [28]. It does not require any sample preparation process before the measurement. RS relies on a frequency change of incoming light photons after inelastic interaction with matter. If the scattered photon has the same frequency or energy as that of the incident light, the interaction process is called as elastic or Rayleigh scattering. If the scattered photon has different frequency or energy than that of the incident light, the process is called inelastic scattering. In RS, local atom-atom bonding structure is investigated by inelastic interaction of incoming photon with longitudinal or transverse modes of phonon. Spectral feature of phonon vibrations in solids can be analyzed by RS, which gives an opportunity for sample identification and phase quantification.

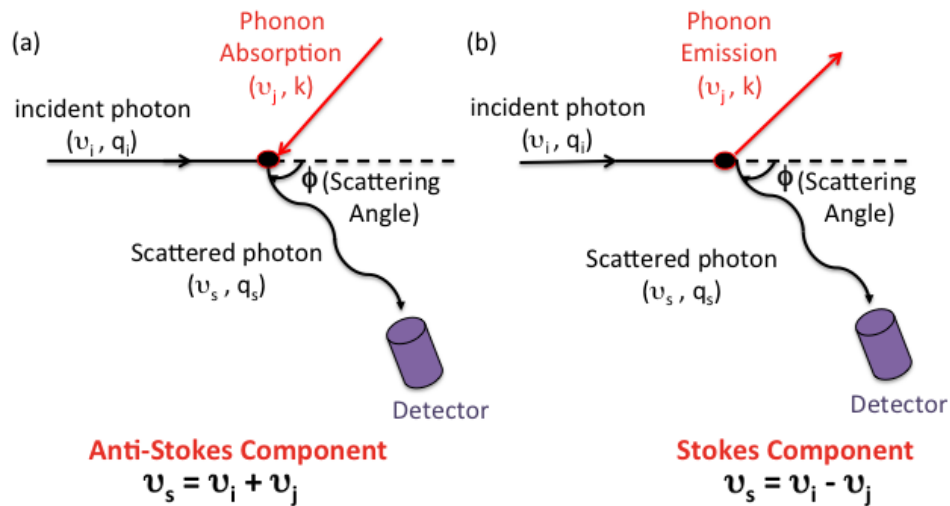


Fig 2-14 Frequency shift after photon - matter interaction; Anti-Stokes shift (a), Stokes shift (b).

Interaction mechanism that causes a frequency change is illustrated in Fig 2-14. If the light photon gains energy after the interaction by absorbing a phonon, the frequency of scattered photon is shifted up and this process is known as anti-stokes Raman scattering. If light photon loses energy after interaction by emitting a phonon, frequency of scattered photon is shifted down, this process is known as stokes Raman scattering. Since the anti-Stokes peaks are weaker than the Stokes peak, generally in Raman spectra Stokes peaks are displayed. Frequency shift is defined as; $\Delta\nu = \nu_s - \nu_i$ and it is equivalent to an energy change since $E = h\nu$. On the other hand, in Raman spectra, results are generally expressed by wavenumber ($\bar{\nu}$) instead of frequency (ν). While frequency is equal to number of vibration per second,

wavenumber is equal to number of waves per centimeter. Relation in between these two terms is $\bar{\nu} = \nu/c$ where c is the speed of the light in vacuum and equal to approximately 2.99×10^8 m/s. Additionally $\bar{\nu}$ is inversely proportional to the wavelength (λ) since;

$$\nu = \frac{c}{\lambda} \quad (\text{Eqn. 2-10})$$

Commonly used unit of the wavenumber is inverse centimeter (cm^{-1}). The energy difference in between the incident and the scattered photons corresponds to the energy of phonons in material. The frequency shift observed in scattering is directly related with vibrational energy of chemical bonds in between atoms within material. Hence, analysis of the scattered frequencies reveals information about the structure of the scattering medium. In crystalline structures local bonds have well-defined energies. Due to narrow distribution of bonding energies, Raman spectra show narrow lines. However, in amorphous structures wide distribution of bonding energies is observed, thus broad scattering signal is obtained from this kind of disordered structures. In Fig 2-15, reference data are shown to represent the phase transition from crystalline silicon phase to amorphous silicon phase with Raman spectrum in the $350 - 650 \text{ cm}^{-1}$ wavenumber range. Microcrystalline silicon is a mixture phase, which includes both crystalline and amorphous phase.

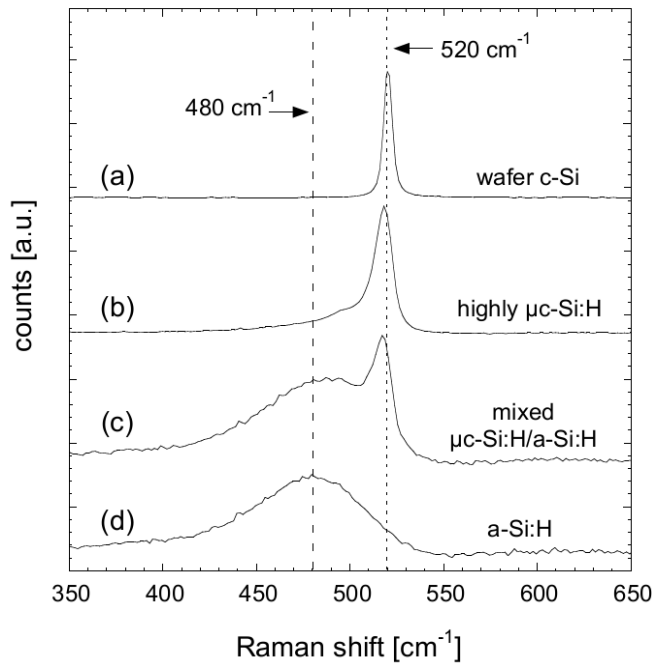


Fig 2-15 Reference RS data for phase transition of the silicon thin film [10]

In this thesis, Raman scattering spectra of the samples deposited with different parameters are measured in the wavenumber range of $200 - 800 \text{ cm}^{-1}$. More specifically, it has been well recognized that Si:H comprises three phases in terms of Raman scattering shift that is usually identified by a deconvolution process with three Gaussian peaks : the amorphous phase ($\sim 480 \text{ cm}^{-1}$), intermediate phase ($\sim 510 \text{ cm}^{-1}$) originating from the defective part of the

crystalline phase associated with grain boundaries and crystalline phase ($\sim 520\text{cm}^{-1}$) resulting from the transverse optical (TO) mode of Si-Si vibrations in the crystalline. In fact, the crystallinity of Si-thin films can be determined by the ratio of the integrated areas;

$$X_c = \frac{I_c + I_i}{(\alpha I_a + I_c + I_i)} \quad (\text{Eqn. 2-11})$$

where I_a , I_i and I_c are the integrated area of amorphous phase, intermediate phase and crystalline phase, respectively in scattering spectra. The factor α is estimated to be 1 if the crystalline sizes are very small. This is semi-quantitative measurement of the crystalline volume fraction [29]. In Fig 2-16, ideal deconvolution of the Raman spectra for silicon samples is represented.

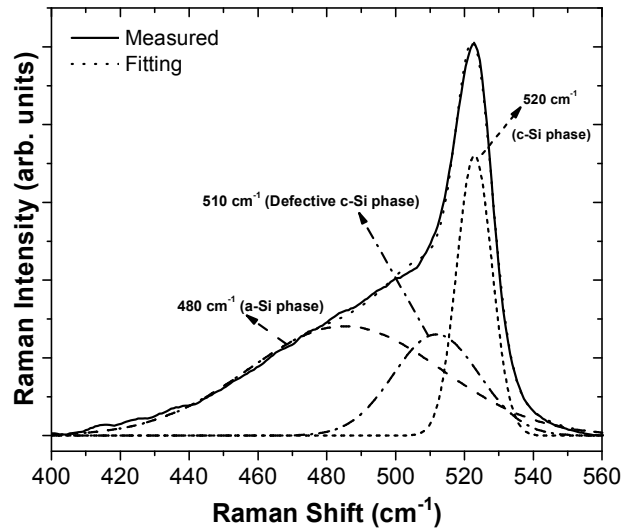


Fig 2-16 Deconvolution of the Raman spectrum for micro crystalline silicon sample.

A slight shift of the 520cm^{-1} peak towards lower or higher wavenumbers can be observed and this shift is attributed to the change in the crystalline size and stress within the film. It is possible to estimate average Raman crystalline size using wavenumber shift of TO mode of Si-Si vibration from 520cm^{-1} in Raman spectrum using the following empirical relation;

$$d_{\text{raman}} = 2\pi \sqrt{\frac{B}{\Delta\bar{\nu}}} \quad \text{where} \quad \Delta\bar{\nu} = 520 - \bar{\nu}_{\text{peak}} \quad (\text{Eqn. 2-12})$$

where $\Delta\bar{\nu}$ is the peak shift, d is the estimated crystalline size and B is a constant value of 2.24 for silicon [30]. In this work, Horiba-Jobin Yvon i550 Raman system is used for measurement. Charge-coupled device (CCD) camera with 1cm^{-1} resolution is attached to the system and 532nm green laser is used as a monochromatic light source at room temperature.

2.3.4 Grazing Incidence X-Ray Diffraction (GI-XRD) Spectroscopy

X-ray diffraction (XRD) is another important characterization technique that gives crystallographic information about sample. XRD relies on the diffraction of x-ray radiation

within the sample into different directions and provides direct evidence of periodic atomic structure of crystals. Crystals are formed of unit cells whose dimensions are called as lattice parameter. For example silicon consists of cubic unit cells, which has only one lattice parameter. By using Bragg's Law, it is possible to determine lattice parameter of crystalline with XRD method.

The atomic planes of a crystal cause an incident beam of X-rays to interfere with one another as they leave the crystal. Interference of the waves can be destructive or constructive according to their phase difference. Bragg's law suggests that constructive interference only occurs when the phase difference is equal to wavelength multiplied by an integer [31];

$$n\lambda = 2d \sin \theta \quad (\text{Eqn. 2-13})$$

where d is the distance between atomic layer in crystal, λ is wavelength of incoming x-ray beam, n is an integer. Diffraction occurs only when Bragg's law is satisfied the constructive interference condition otherwise waves cancel out each other.

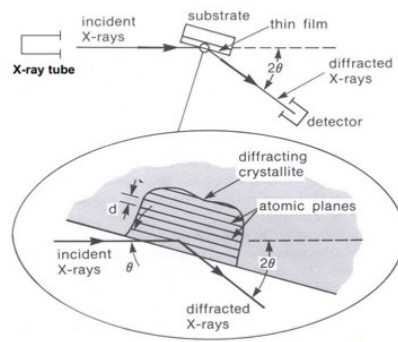


Fig 2-17 Basic feature of typical XRD measurement

Basic XRD measurement configuration is shown in Fig 2-17. Generally, Bragg-Brentano configuration is used in XRD measurement system. In this configuration, incident and diffracted x-ray beam make the same angle with the sample surface. Diffraction maxima appear when the angle coincides with a Bragg angle (θ_B). However, since x-ray radiation has a large penetration depth into the material, thin film characterization is very problematic due to its slight diffracting volume and low diffracting intensity. Thus, it is more suitable to use special technique that is called grazing incidence (GI) angle XRD. GI-XRD method is applied at very low incidence angles ($0.1^\circ - 3^\circ$) to increase the path of incoming x-ray radiation through the thin film and enhance the out-coming signal strength. Because of this asymmetric configuration, it is possible to irradiate larger surface area. During the diffraction spectrum collection, incident angle and x-ray path are kept constant, while detector is rotating through the angular path around the thin film surface.

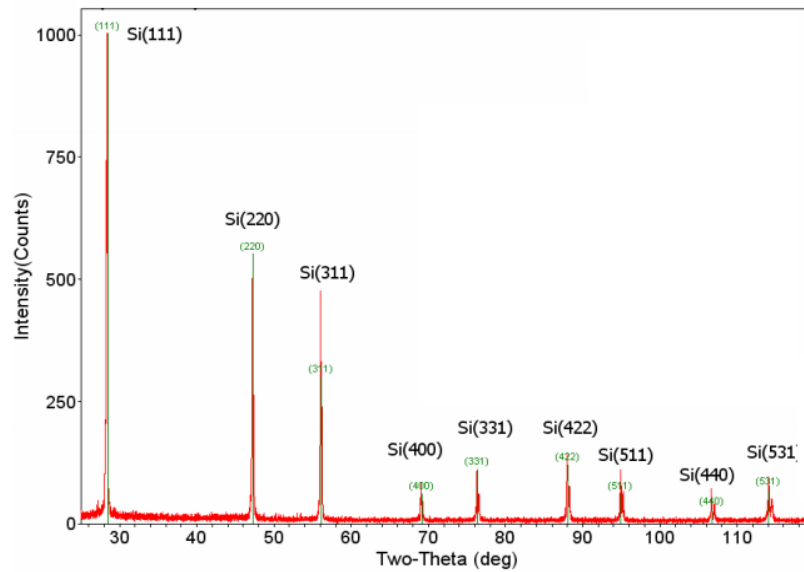


Fig 2-18 Reference data of XRD spectra for crystal silicon

In Fig 2-18, a typical diffraction pattern of crystalline silicon is shown. More specifically, three pronounced diffraction peaks located at $2\theta = 28.4^\circ$, 47.4° and 55.8° can be attributed to Si (111), (220) and (311) planes, respectively. These three peaks are more commonly used during the analysis since their intensities are higher than the rest. It is possible to identify structure and lattice parameter by analyzing peak position. Additionally, crystalline size and preferred orientation of crystals can be determined using peak width and area. Average Si grain size can also be estimated using the well-known Debye Scherrer's formula;

$$d_{XRD} = \frac{k\lambda}{\beta \cos \theta} \quad (\text{Eqn. 2-14})$$

where k is a shape factor, λ is the wavelength of the X-ray, β is the full-width-half-maximum (FWHM) of peak at 28.4° and θ is the Bragg angle. FWHM of diffraction peak is defined as the width of the peak, measured in radians at the half height of the same peak. Although size calculation using Scherrer's formula has advantages of being simple and non-destructive, it is not very reliable since shape factor and FWHM determination are not easy for complex structure. Nevertheless, it enables us to observe relative changes in the crystal size with deposition parameters and to compare the obtained crystal size with Raman crystal size.

In this study, structural GI-XRD is carried out in Rigaku Ultimate-IV diffractometer with $\text{CuK}\alpha$ radiation ($\lambda=1.5406\text{\AA}$) source. Measurements are conducted with 2θ scans over angular range from 20° to 80° by using 1 degree/minute scan speed.

2.3.5 Fourier Transform Infra-Red (FTIR) Spectroscopy

Like Raman Spectroscopy, infrared (IR) spectroscopy is based on the interaction between a

sample molecule and infrared radiation. Mainly, IR spectrum is measured by transmitting infrared radiation through the sample and determining what portion of the incoming radiation is absorbed at a particular frequency. All the atoms in a molecule make vibrations relative to each other continuously above absolute zero temperature. If the vibration frequency of molecule matches with the frequency of the incident IR radiation, the molecule in the sample absorbs the light and makes vibrational motion with that particular frequency. Thus, the frequency at which any peak in an absorption spectrum shows up is related with the frequency of molecule vibration. One important restriction for IR absorption is that during the vibration, electric dipole moment of the molecule should change; this is called as a selection rule of IR spectrum. Molecular vibrations include both changes in bond length and bond angle, which are called stretching and bending, respectively. In Fig 2-19, stretching and bending modes of C-H bonds are illustrated as an example. According to the direction of the bending, this type of vibration can be classified as rocking, scissoring, wagging and twisting. When bonds stretch in phase, symmetric stretching is observed. If bonds stretch out-of phase, asymmetric stretching is obtained (Fig 2-19). Usually, symmetric bonds do not show any IR absorption, as this kind of stretching mode does not lead to a change in electric dipole moment of the related molecule. The larger change in dipole moments means more intense IR absorption. Thus asymmetric vibrations are very significant to obtain reliable results from IR spectra.

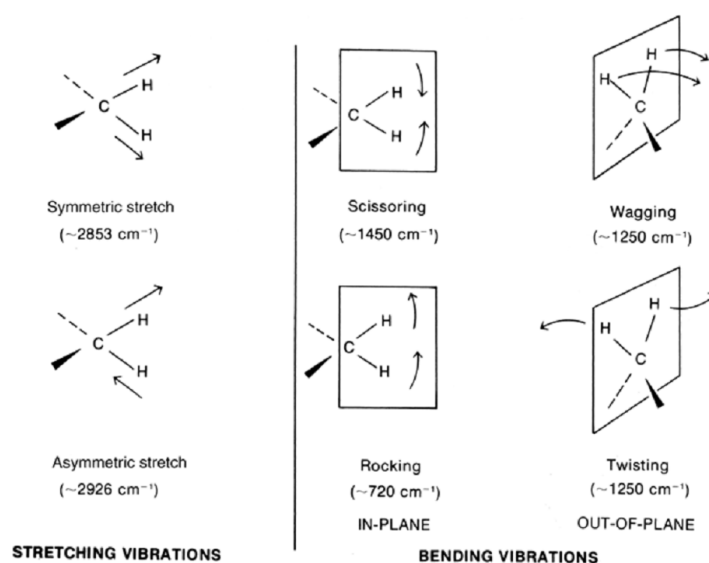


Fig 2-19 All stretching and bending vibrations of C-H bonds

In general IR spectrum is divided into three regions: near, mid, and far IR. In this work, FTIR measurements are performed in the mid-IR region that covers the wavelength (λ) range in between 2.5 μm to 25 μm . Spectral results are usually presented in wavenumbers like in Raman spectroscopy. Since,

$$\bar{\nu}(\text{cm}^{-1}) = \frac{1}{\lambda(\mu\text{m})} \times 10^4 \quad (\text{Eqn. 2-15})$$

Typical mid-IR spectrum lies in between 400-4000 cm^{-1} in wavenumber (ν). This spectrum can be divided into four regions. The vibrations in the 4000 - 2500 cm^{-1} region are related with the X-H (O-H, C-H, N-H, etc.) stretching mode. In 2500 - 2000 cm^{-1} regions, triple bond stretching absorption is observed due to the high force constant of bonds. The vibrations related with the double bonds lies in range from 2000 to 1500 cm^{-1} . Lastly, region in between 1500-600 cm^{-1} is called as finger print region of the sample since it provides an opportunity to identify samples from the wavenumber positions of the absorption band. More specifically, the vibration mode of the hydrogenated silicon films, which is subject of this thesis, is given in Table 2-2.

Table 2-2 *Vibration modes and wavenumber for hydrogenated silicon films*

Wavenumber(cm^{-1})	Vibration Mode
640	Si-H Bending
880	SiH ₂ Bend-scissors
2000	Si-H Stretching
2090	SiH ₂ Stretching
1080	Si-O-Si Stretching

Schematic representations of the vibrational modes of silicon involving hydrogen motions are illustrated in Figure 20.

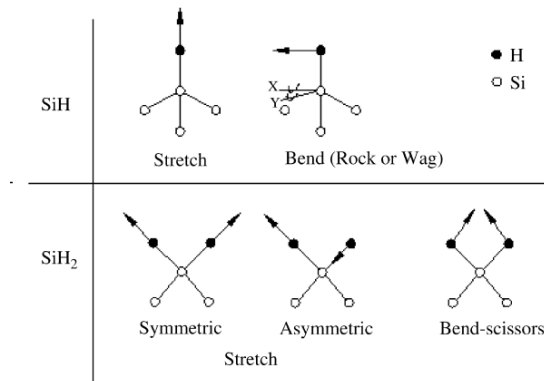


Fig 2-20 *Local Si-H vibrational modes for SiH and SiH₂ group*[32]

Furthermore, it is possible to calculate the oxygen or hydrogen concentrations of the deposited hydrogenated silicon thin films using the peak intensities in the IR absorption spectrum. Since hydrogen content affects all optical and electrical properties of the films, it is very essential to be able to calculate hydrogen content. of the IR absorbance band can be used to determine the hydrogen concentration of the films using a generally accepted method that employs the following relation [33];

$$C_H = \frac{A_w}{N_{Si}} \int \frac{\alpha(\nu)}{\nu} d\nu \quad (\text{Eqn. 2-16})$$

where A_w is the proportionality constant for Si-H bending mode and it is equal to $1.6 \times 10^{19} \text{ cm}^{-2}$, N_{Si} is the atomic density of pure silicon which is equal to $5 \times 10^{22} \text{ cm}^{-3}$, $\alpha(\nu)$ is the absorption coefficient. For the integrated component, only the peak intensity of Si-H bending mode that is located around 640 cm^{-1} is calculated. The absorption coefficient is related to the transmission according to Beer-Lambert Law;

$$\alpha = \frac{-\log(T)}{d} \quad (\text{Eqn. 2-17})$$

where d is the thickness of the film. In this work, FTIR spectroscopy measurements are performed by using Bruker-Equinox spectrometer in the absorbance mode at wavenumbers between $400\text{--}4000 \text{ cm}^{-1}$ with 4 cm^{-1} resolution. Characteristic IR absorption spectra taken by FTIR for a-Si are shown in Fig 2-21, as a reference data [4].

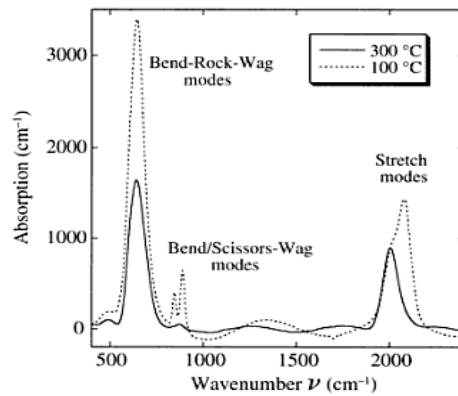


Fig 2-21 Typical IR absorption spectrum of a-Si:H thin film[4]

In this work, FTIR measurements are performed from the films deposited on c-Si substrate. It should be remembered that the resultant spectra may be different from that obtained from the layer deposited on glass substrate.

2.3.6 Photoluminescence (PL)

Luminescence is the light emission that results from the spontaneous radiative recombination [34]. It refers to the emission of electromagnetic radiation from a material under some form of excitation such as light illumination, electron illumination, chemical reaction or voltage applied in visible region. For many substances, the emission is independent of the nature of the excitation, which is pre-request to the emission. The emission of radiation results when a material adjusts itself from an excited state to the ground state. The quality and quantity of luminescence radiation are strongly dependent on the nature of the excited material. The luminescence, which arises after absorption of photon process, is called photoluminescence (PL).

PL spectroscopy is a powerful analysis technique that provides valuable information about electronic structure and material quality. Specifically, PL is used to investigate basic properties

of the semiconductor materials such as defects, impurity concentration, energy levels and band gap. In PL mechanisms, the exciting photon should have energy greater than the material band gap energy to be able to be absorbed and excite an electron from the valence band to the conduction band. This process is called as photo excitation. After the excitation of the electron to the higher energy level of the conduction band, electron loses energy through lattice scattering until it drops the bottom of the conduction band. Then it can directly recombine with a hole in the valence band by emitting a photon with energy equal to the band gap, E_g . Thus the energy of the emitted photon is directly related with the band gap energy of the material.

Basically, semiconductor materials are divided into two groups: direct band gap and indirect band gap materials. For direct band gap material, maximum of the valance band and minimum of the conduction band are located at the same value in the momentum space (k-vector). However for indirect band gap material, maximum of valance band and minimum of conduction band are not at the same momentum space. Carrier excitation in materials can be classified into five group; (1) hot-carrier inter-band excitation, (2) excitation across the band gap absorption edge, (3) exciton generation, (4) impurity level excitation, (5) intra-band excitation [35]. Fig 2-22 shows schematic illustration of these excitations.

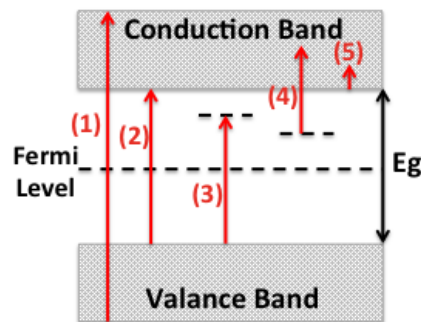


Fig 2-22 Schematic diagram for the different optical absorption mechanism in materials[35]

After excitation of carriers, in a material with direct band-gap carriers recombine directly by emitting a photon. On the contrary, in a material with indirect band-gap, for carrier transition from conduction band to valance band phonon emission (crystal lattice vibration) is needed in addition to photon emission in order to conserve momentum in momentum k-space. Thus, the photoluminescence of indirect band gap materials is negligible when it is compared with direct band gap material. The low probability of radiative recombination in indirect band gap materials favors non-radiative decay processes, and excited electrons generally lose energy as heat, not emitted photons.

In the scope of this thesis, PL characteristic of silicon material is investigated. As it is mentioned before Si is the most predominant material in the electronics world, not only because of its abundance and low-cost, but also as it has a stable oxide, which offers outstanding electronic passivation. However, due to its indirect band gap, silicon is not a strong light emitter. Schematic illustration of silicon indirect band structure and the most relevant transitions are shown in Fig 2-23. Black line shows the absorption of a photon via a phonon-

assisted indirect transition, red line shows emission of a photon via a phonon-assisted indirect transition, orange line indicates free carrier absorption and green line shows the Auger recombination process in silicon [36].

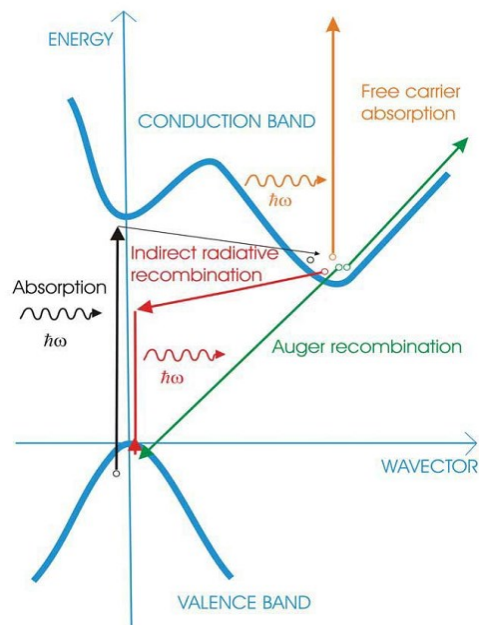


Fig 2-23 Simplified energy diagram of Si [36]

Recently, it was shown that it is possible to obtain light emission from silicon material when its size is reduced to nanometer level. This effect called quantum size effect provides also the ability of band-gap engineering. In 1990, Canham discovered that porous silicon, which has nanometer scale features, displays efficient photoluminescence at visible region above the bulk Si band gap of 1.12 eV. Since then, luminescence of Si nanocrystals has been studied in various systems such as single nanocrystals, multilayered structures, etc. Another way of obtaining light emission is to introduce localized impurity states in the band gap of Si [37]. Adding localized states into the energy diagram of the silicon where excitons can be trapped and recombine radiatively making Si luminescent [38].

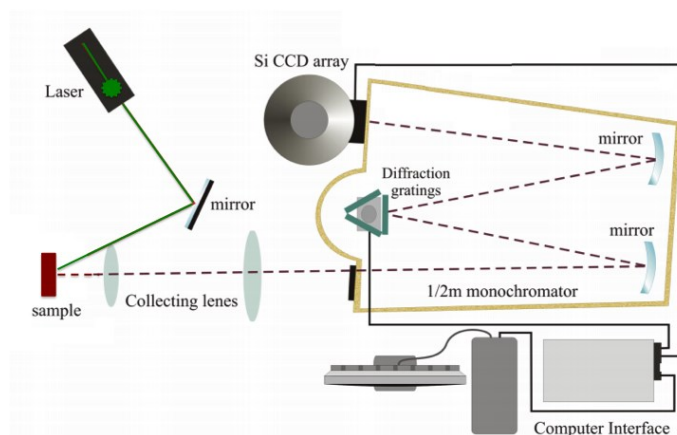


Fig 2-24 Schematic of the experimental apparatus used for PL measurement.

Fig 2-24 shows the PL measurement set-up that we used in this study. Green laser with 532 nm wavelength is used as an excitation source. Laser beam is directed on to the sample via various mirrors. The luminescence emitted from sample is collected and focused by two convex lenses onto the entrance slit of the monochromator. In front of the entrance slit, a notch filter is placed in detection channel to increase the signal-noise ratio. The signal obtained from sample was resolved with the monochromator that has three diffraction gratings with 1200 lines/mm, 600 lines/mm and 300 lines/mm. A Charge Coupled Device device (CCD) that is mounted on the monochromator is used for the light detection.

In this thesis, photoluminescence of nc-Si embedded in SRSO matrix and highly nc-Si:H film prepared by an inductively coupled plasma system.

2.3.7 Conductivity Measurements

Conductivity measurements are another important characterization technique to determine the film quality, since conductivities of the deposited films are directly related with their structural characteristics and crystalline volume fractions. During this study, co-planar electrode configuration is used for the conductivity determinations. Two parallel a few hundred nanometers thick aluminum electrodes are thermally evaporated on top of the silicon film. Separation of the electrodes was kept 0.5mm and electrode length was 10mm (Fig 2-25). After evaporation metal contacts were annealed under nitrogen flow at 150 °C in order to evaporate the moisture on the surface.

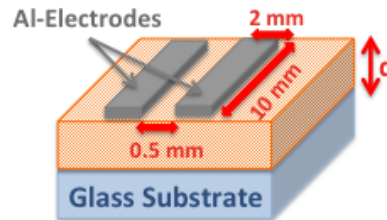


Fig 2-25 Experimental structure for co-planar conductivity measurements on silicon layers.

The basic principle of the measurement is that, electric voltage V was applied to two parallel metal electrodes and resulting electrical current passing through the film was measured. While determining the photo response, films were illuminated with AM 1.5 Sun. Conductivity calculations were performed by the following formula:

$$\sigma = \frac{I}{V} \frac{w}{ld} \quad (\text{Eqn. 2-18})$$

slope of the current-voltage graph gives the film resistance ($R=V/I$), w is the distance between two electrodes, l is the length of the electrodes and d is the thickness of the deposited film. During the calculations, current density was assumed uniform over the cross section for simplicity.

CHAPTER 3

CRYSTALLIZATION PROPERTIES OF SI-THIN FILMS PREPARED BY DIFFERENT DEPOSITION TECHNIQUES

3.1 Crystallization of CCP-CVD Deposited Si-Thin Films

nc/ μ c-Si thin film layers with desired properties is very essential for tandem solar cells applications. This type of thin film exhibit promising features including good electrical conductivity, controllable band gap energy and low absorption coefficient in the visible range of the spectrum. Numerous analyses and studies have been performed about nc/ μ c-Si thin film produced using several methods that are mentioned in previous chapter. The most common way of producing crystallized Si-thin films is the deposition of a-Si:H films and crystallize them via post-annealing (Solid Phase Crystallization) in a conventional tube furnace or using newly developing techniques like excimer laser annealing. In this part of the thesis, direct crystallization behavior of Si-thin films during PECVD deposition is investigated. nc/ μ c-Si layers are usually deposited with very high excitation frequency (greater than 40 MHz) power supplies. Nevertheless, in this work conventional (13,56 MHz) RF-PECVD system is used for layer production. The effect of substrate temperature, hydrogen dilution of the feed gas and deposition pressure on the crystalline volume fraction are systematically examined. It is very essential to understand how these deposition parameters influence the crystalline volume fraction of the film. In most of the a-Si solar cell structure, layers are deposited close to the transition regime between the two microstructures (from amorphous regime to nano- /micro-crystalline regime) for the best photovoltaic performance [39]. Moreover, a-Si:H fabricated near the onset of micro-crystallization shows more stable properties [40, 41]. Transition from amorphous regime to crystalline regime is commonly obtained by controlling the hydrogen dilution of the feed gas, however other deposition conditions such as total deposition pressure, substrate temperature and RF power have crucial importance for the nc/ μ c-Si:H growth and opto-electrical properties of the deposited films [42].

3.1.1 Pressure Effect

In the first sample set, films were deposited at room temperature to observe the crystallization without any heating. Deposition parameters are shown in Table 3-1.

The substrate area that is used in this work is quite large, 25x25cm (Corning Eagle-XG glass). Applied power is around 0.48W/cm². In order to passivate the dangling bonds and obtain more stable silicon thin films additional hydrogen gas is also fed to the evacuated chamber. Base pressure of the chamber is around 1x10⁻⁶ Torr just before the deposition.

Table 3-1 Deposition parameters of the films fabricated at room temperature with different pressure.

Deposition Power	SiH ₄ Flow	H ₂ Flow	Deposition Pressure	Deposition Duration
300W	10 sccm	500 sccm	0.8 - 2.5 Torr	35 - 50 min

To be able to observe the crystal phase change, deposition pressure is altered systematically from 0.8 Torr to 2.5 Torr while the all other parameters are kept constant. In order to keep thicknesses constant, deposition duration is adjusted with respect to the deposition rate, which is observed to be depending on the pressure. The thickness of the all deposited films are around 400 - 450 nm. Keeping the thickness constant is important when observing the crystalline volume fraction change with deposition parameters due to the fact that microcrystalline grain size and crystal volume fraction are strongly related with thickness of the deposited films [43]. In general, grain size and crystalline volume fraction increase systematically with increasing film thickness [44].

The Raman scattering spectra of Si-thin films deposited at room temperature with different total deposition pressure is shown in Fig 3-1.

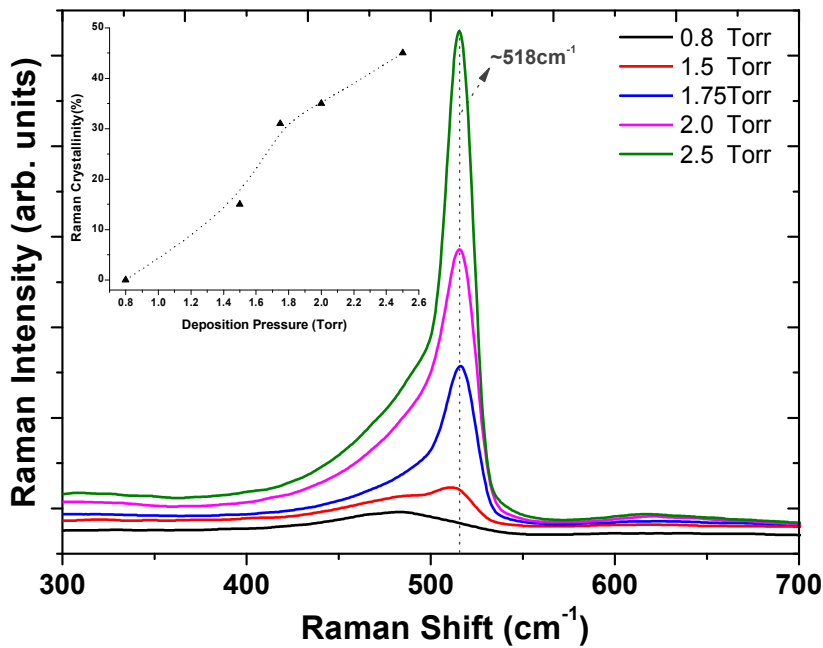


Fig 3-1 Raman spectrum of the films deposited at room temperature with different deposition pressure.

According to Fig 3-1, if the pressure is below 1.5Torr, the film remains in the amorphous regime characterized by a broad - band centered at around 480 cm⁻¹. However, when the pressure is above 1.5 Torr, a transition from a-Si:H to nc-Si growth occurs as indicated by the emergence of the narrow peak located at 518 cm⁻¹ which is a sign of c-Si structure occurrence. The relative intensity of the crystalline peak increases with increasing pressure since the decomposition of the SiH₄ feed-gas increases. Thus SiH_x (0≤x≤3) related radicals are

increasing drastically with releasing H_2 . Especially, SiH_3 radical is very important for film growth since it has low reactivity and high surface mobility [45]. With more dissociation, more H_2 and SiH_3 precursors are created. Additional H_2 and SiH_3 help passivation of dangling bonds and create more ordered micro - structures by surface reactions. Hence, high deposition pressure promotes the crystal formation due to the greater amount of SiH_3 and H_2 [46]. The spectrum was decomposed into three components: the crystalline silicon TO mode component peaked at around 518 cm^{-1} , the amorphous component peaked at 480 cm^{-1} , and an intermediate component peaked at $505 - 510\text{ cm}^{-1}$ which is associated with bond dilation at grain boundaries [47]. Raman crystallinities (X_c) are calculated using integrated areas of these three peaks and this method is explained in previous chapter in detail. Alteration of crystalline volume fraction with pressure is shown inset of the Fig 3-1. It changes from 0 to 64% just by increasing deposition pressure from 0.8 Torr to 2.5 Torr.

In the second set, films are deposited at 200°C with different pressure values; all other parameters are kept constant to observe the pressure effect on the heated substrate. Raman spectra of these samples are shown in Fig 3-2. Three different films are deposited at 0.5, 1.0 and 1.5 Torr. As it is obviously seen from Fig 3-2, at high temperature depositions, pressure effect become weaker on the crystalline volume fractions of the deposited films. Calculations of crystalline volume fraction show that the amount of crystallization changes slightly in these films. The film deposited at 0.5 Torr has crystalline volume fraction around 62.5 %, while at 1.5 Torr it is approximately 63.9%. FWHM values of the crystalline silicon phase related peak changes from 18 cm^{-1} (for 0.5 Torr) to 16.5 cm^{-1} (for 1.5 Torr) with increasing pressure. Thus it is possible to conclude that crystalline regime peak becomes narrower very slightly with increasing deposition pressure. Transition from amorphous regime to nano/micro crystalline regime with pressure is not clearly observed in this case, since temperature effect become more dominant.

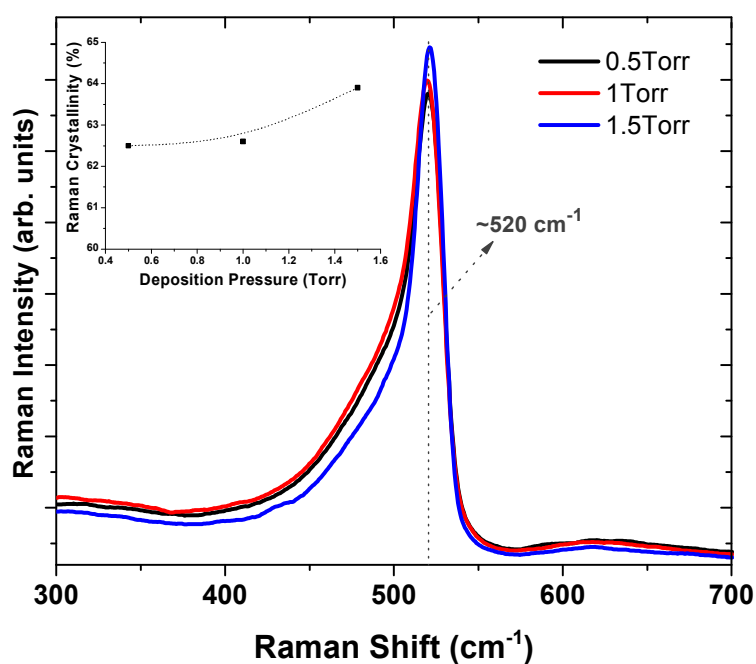


Fig 3-2 Raman spectrum of the films deposited at 200°C with different deposition pressure.

Nevertheless, Raman data shows that high deposition pressure effects the micro/nano-crystal formation positively during the film growth and causes an enhancement of crystallization.

3.1.2 Effect of Silane Concentration (SC)

Most of the scientific researches about silicon thin films indicate that excessive hydrogen dilution in silane plasma affects the microstructure of the films even at low temperature [48]. In practice, dilution level of SiH₄ in H₂ is defined as SC, which is equal to;

$$SC(\%) = \frac{[SiH_4]}{[SiH_4]+[H_2]} (x100\%) \quad (\text{Eqn. 3-1})$$

where [SiH₄] , [H₂] are silane and hydrogen flow, respectively. Hence, SC can be defined as the ratio of the silane flow to the total flow.

In this set of experiment, silane concentration of the feed-gas is varied from 4.2% to 2% by adjusting the ratio of the hydrogen flow while keeping silane flow constant at 10 sccm. Deposition parameters are shown in Fig 3-2. Depositions are performed at a pressure of 2 Torr and substrate temperature of 200°C. 440 nm thick films have been deposited on corning glass and p-type Si wafers in (100) crystallographic direction with a resistivity of 10-20 Ω.cm for different series of analysis.

Table 3-2 Deposition parameters of the films fabricated at 200°C with different SC

Deposition Power	SiH ₄ Flow	H ₂ Flow	Deposition Pressure	Deposition Duration
300W	10 sccm	240 - 500 sccm	2 Torr	35 - 50 min

A series of samples has been characterized by Raman scattering spectroscopy, grazing incidence x-ray diffraction and infrared spectroscopy. Additionally, current-voltage characteristics of the deposited films are also examined both in dark and illuminated ambient.

3.1.2.1 Structural and Optical Characterization

The Raman scattering spectrum of the Si-thin films deposited at the various hydrogen dilution ratios is measured and shown in Fig 3-3. The curves are shifted for better clarity. When the R-value is equal to 4.2%, single broad peak centered around 480 cm⁻¹ is observed. This peak is a typical amorphous silicon signal and for this sample we observe no crystallization. Decreasing R by increasing hydrogen flow causes a small peak shoulder at 518 cm⁻¹, which obviously indicates the occurrence of micro/nano-crystalline silicon growth for the sample deposited with 2.5% silane concentration. Under these deposition conditions, the transition region of amorphous to micro/nano-crystalline regime is observed.

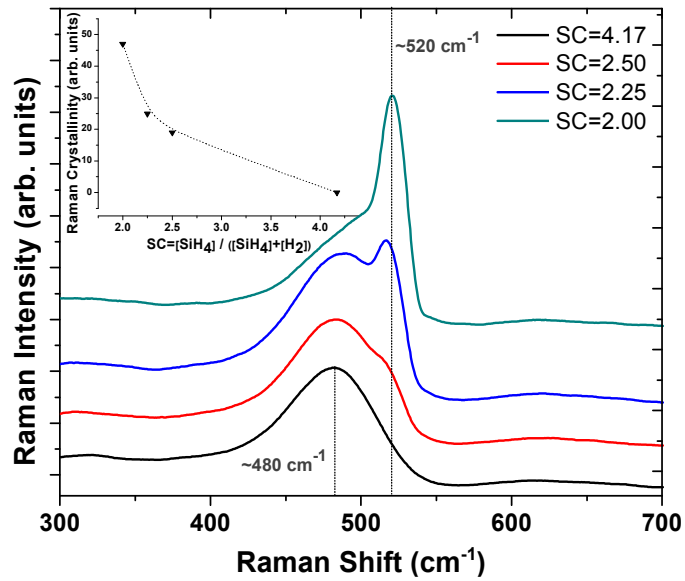


Fig 3-3 Raman spectrum of the films deposited at 200°C with different SiH₄ concentration

For 2% silane concentration, peak of crystalline silicon phase located at around 520 cm⁻¹ becomes more intense and dominant; FWHM is decreasing with decreasing SC. In the inset of Fig 3-3, calculated crystalline volume fractions with respect to R is shown. We see that the crystalline volume fraction is easily controlled from 0% to 49% with hydrogen dilution. It is also possible to observe that with the increase of the hydrogen dilution ratio, position of silicon crystalline phase Si-Si TO mode related peak shows a slight shifting from 518 cm⁻¹ at SC=2.5 to 520 cm⁻¹ at SC=2. This shift is correlated with the size of the Si grains in the structure, since Raman crystal size is inversely related with the shift in the wavenumber from 521cm⁻¹. This is in a good agreement with the literature [42, 49]. Raman grain size is calculated using the method which is explained in the previous chapter, however it is not possible to calculate grain size for the sample SC=4.17.

Table 3-3 shows the calculated grain sizes.

Table 3-3 Calculated grain size from Raman spectrum

SC=[SiH ₄]/([SiH ₄]+[H ₂])	4.17	2.50	2.25	2.00
Raman Grain Size	-	5.4 nm	6.6 nm	7.4 nm

Decreasing silane concentration SC causes an increase in the size of the silicon grains. However, it should be mentioned that this slight shift could also be attributed to the stress effects within the films [50, 51].

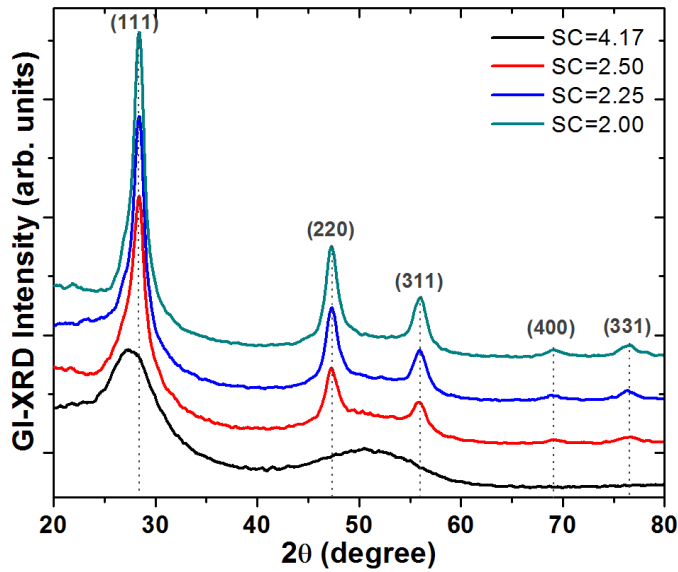


Fig 3-4 GI-XRD spectrum of the films deposited at 200°C with different SiH_4 concentration

X-ray diffraction (XRD) is another straightforward method to analyze crystallization of the deposited films and evaluate the grain sizes. Fig 3-4 shows GI-XRD spectra of the same sample series for which Raman spectra is shown in Fig 3-3. For silane concentration of 4.17%, Raman spectra does not provide any crystal silicon phase related peak, however in GI-XRD spectrum broad peak located at 27.69° shows the presence of crystallization in (111) plane. This pattern indicates nano-crystalline formation in Si (111) plane on the film surface, however the film structure is still mostly amorphous due to the quite wide FWHM of the observed peaks. As SC is decreased with increasing hydrogen dilution, the other crystalline orientations emerge. In addition to the major (111) peak seen at 27.69° , two additional peaks originated from Si (220) and Si (311) planes are clearly observed at 46.26° and 55.79° , respectively. With a further decrease of silane concentration R, Si (400) and (331) crystal planes also become slightly clear at around 69° and 76° . The intensity of the (111) peak increases more than the intensities of the any other peaks with increasing hydrogen dilution. Hence, GI-XRD spectrum indicates that preferential growth orientation of the grains in the deposited films is (111) crystal plane. According to Kakinuma et al. this preferential growth is explained with the lower surface energy of (111) Si crystal plane than the other planes [44]. Additionally, there are other parameters that affect the preferential growth such as nucleation, lateral growth, substrate temperature and etching [52]. In the study reported by Matsuda et al. and Veprek et al. it is shown that preferential growth direction can be transformed from (111) to (220) plane with varying the substrate temperature [53, 54]. Detailed information about preferential growth direction can be obtained from scientific publication of Kakinuma et al.[44]. The grain size of the films estimated from the FWHM and position of (111) peak using Debye-Scherrer formula and FWHM values of silicon crystal plane peaks are summarized in Table 3-4. Besides the grain size calculation, FWHM is an important parameter for crystallinity determination of the samples. Decrease in FWHM indicates the enhancement of the crystallinity. In this case, FWHM of (111) peak decreases with decreasing silane concentration SC. Accordingly, the average grain size increases from 1.2 nm to 6.3 nm in the

respective samples. The results obtained by Raman spectroscopy agree with XRD analysis quite well (see Table 3-3). For instance, grain size calculated using Raman spectra is 5.4 nm while with XRD it is 4.9 nm for the sample deposited with silane concentration 2.5%.

Table 3-4 Summary of GI-XRD data of films deposited with different SiH₄ concentration

SC	2θ (degree)					FWHM					Size (nm)
	(111)	(220)	(311)	(400)	(331)	(111)	(220)	(311)	(400)	(331)	
4.17	27.69	-	-	-	-	6.66	-	-	-	-	1.2
2.50	28.36	47.26	55.79	69.20	76.60	1.67	1.38	1.55	1.90	3.00	4.9
2.25	28.41	47.25	55.84	69.00	76.22	1.31	1.32	1.60	1.40	2.50	6.2
2.00	28.40	47.21	56.23	68.95	76.55	1.30	1.51	1.90	4.60	2.60	6.3

FTIR absorption measurement is also conducted for determination of Si-H bonding modes and calculation of the bonded hydrogen content of the films. FTIR absorption spectra in the range 550-2200 cm⁻¹ for the Si thin films deposited with different silane concentration SC is shown in Fig 3-5. Thin vertical dotted lines specify position of the absorption modes in Si thin films. The absorption band at 630cm⁻¹ is attributed to the Si-H rocking/wagging mode, the ones at 870 cm⁻¹ is attributed to the Si-H₂ bending modes and the other one at around 2000-2030 cm⁻¹ is ascribed to the Si-H_x (1≤x≤3) stretching modes.

As it is clearly seen in Fig 3-5, silane concentration affects the intensity of the related absorption band spectra. The rocking/wagging absorption band peak is located at same peak position for all deposited films with different silane concentration SC, however the intensities of these peaks are changing with SC. Si-H₂ bending band peak centered at around 870 cm⁻¹ has the same intensity and position for all films. This indicates that the silane concentration change does not affect bending band significantly. However stretching band peak located at 2000- 2030 cm⁻¹ varied both in intensity and position. As it can be seen clearly from the Fig 3-5, the symmetry of the stretching band is also influenced significantly from SC.

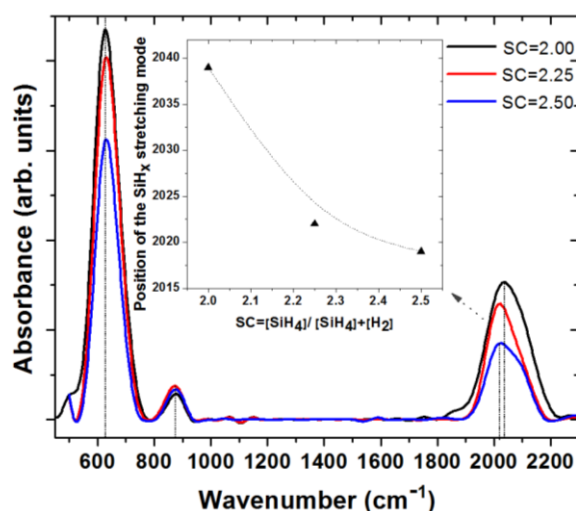


Fig 3-5 FTIR Spectra of films deposited with different SiH₄ concentration

The intensities of all peaks are related with the bonded hydrogen content of the films while the position change is related with the micro-structures. Structure of the films can be analyzed with stretching mode peak in detail.

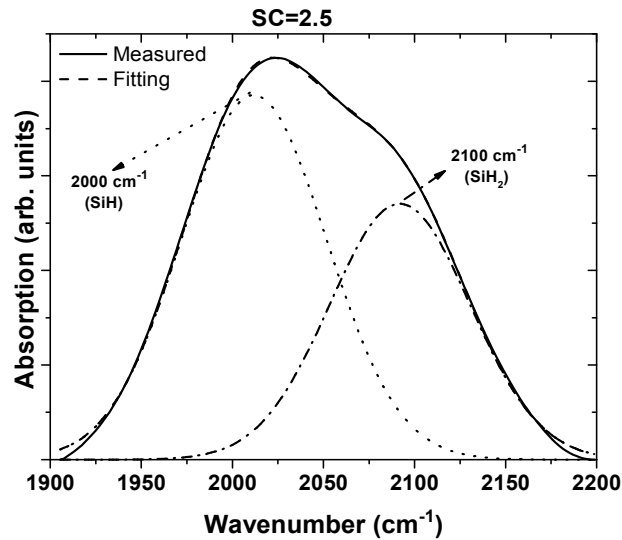


Fig 3-6 Deconvolution of the $Si-H_x$ stretching mode

Each film possesses a particular ‘microstructure’ that denotes the structure on a scale from the atomic level to 10-15 nm. In Si-thin films, many features such as H-bonding configurations, internal surface related micro-voids, vacancies, bonded or un-bonded-H distributions come together and generate microstructure [55]. Especially, micro-void density in the material is a very significant parameter that reduces the film quality, since a high amount of hydrogen atoms bonded to micro-void related internal surface instead of passivating dangling bonds. Researchers defined a microstructure factor, r , to differentiate isolated silicon-hydrogen bonds in a dense network and other bonding configurations, such as internal void surface bonds and isolated di-hydride bonds [56].

For Si-layers microstructure factor, r , is calculated for estimation of the micro-void concentrations and structures [57, 58]. In order to calculate r , $Si-H_x$ bond stretching mode located at around 2000-2030 cm^{-1} is deconvoluted into two Gaussian components using Peak Fitting program as it is shown in Fig 3-6 for the sample SC=2.5. Deconvoluted Gaussian peak located at 2000 cm^{-1} is related with the absorption band owing to stretching mode of isolated Si-H bonds and 2100 cm^{-1} is related with all other bonds in stretching modes. Isolated bonds are always desired for high quality materials, hence r should be equal to zero, ideally [55]. Microstructure factor is defined as follows;

$$r = \frac{I_{2100}}{I_{2100} + I_{2000}} \quad (\text{Eqn. 3-2})$$

where I_{2000} and I_{2100} are intensities of the deconvoluted peaks. The microstructure factor increases with increasing micro-void concentration [59]. In our case, calculated r - value increases up to 0.5 with decreasing silane concentration. For the sample R=2.5 microstructure

factor is equal to 0.4. This shows that with decreasing silane concentration, SiH_2 related stretching mode located at 2100 cm^{-1} become more dominant and causes a shift in the SiH_x stretching mode slightly towards to higher wavenumbers. In the inset of the Fig 3-5, it is also shown that the position of the SiH_x stretching mode changes with the silane concentration. This shift is attributed to the formation of grain boundaries and micro-voids during nano-crystalline silicon formation [60].

Bonded hydrogen content, C_H , within the films is also calculated using the procedure explained in the previous chapter. We see from Fig 3-5 that the intensity of the FTIR signals is increasing with decreasing silane concentration SC. As might be expected, when the hydrogen dilution increases, the bonded hydrogen amount within the films increases. Fig 3-7 shows the numerical values of C_H deduced from intensity of the 630 cm^{-1} mode as a function of silane concentration.

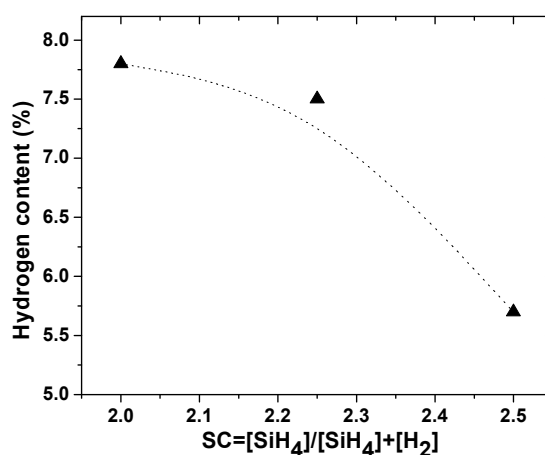


Fig 3-7 Estimated bonded hydrogen content C_H of films deposited with different SiH_4 concentration

Hydrogen contents of all deposited films are less than 10% which is desirable for high quality silicon thin films since high hydrogen content within the film induces micro voids formation [61]. C_H declines from 7.8% at $R=2\%$ to 5.6% at $R=2.5\%$.

3.1.2.2 Electrical Characterization

The electrical conduction in the produced films is crucially important for the device operation. It is well known that the conductivity in dark and under illumination depends on the structure of the films.

In general, the electronic conduction in the $\mu\text{c}/\text{nc}$ -Si films is easier than amorphous ones [62], due to the less defects and higher carrier life time and higher conductivity. This is an advantage when the charge collection after the light absorption is considered. Although we mainly focused on the structural and optical properties of the films in this study, we studied the electrical properties of the films to see the correlations with the structural properties.

Photo and dark-conductivity measurements are performed to study the carrier transport properties of the deposited films as a function of silane concentration at room temperature. In

Fig 3-8 current-voltage characteristics of the films are shown in logarithmic scale. As it is seen from Fig 3-8, with increasing crystallinity, the amount of current flow for a given voltage increases from around 10^{-8} to 10^{-5} due to the increase in the conductivity. The sample with 2% silane concentration has a crystalline volume fraction of about 49%. The sample prepared with 4.17% silane concentration in the feed-gas phase is purely amorphous with dark conductivity of $2.15 \times 10^{-6} \text{ S.cm}^{-1}$.

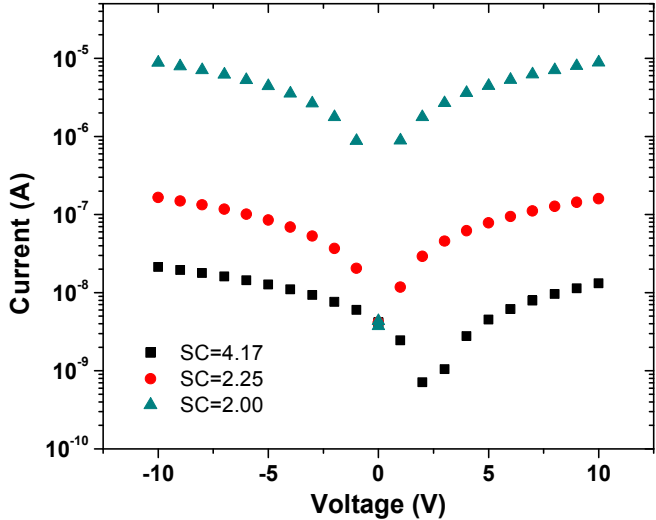


Fig 3-8 Dark I-V Characteristics of the films deposited with different H_2 dilution

These results indicate that dark conductivity increases with crystalline volume fraction as expected. The effect of light illumination on the I-V characteristics is also displayed in Fig 3-9. When the micro-structures change from amorphous regime to micro-/nano-crystalline regime, the photosensitivity of the film decreases drastically. Due to the metal semiconductor contact that creates Schottky Barrier, current flow has been observed for zero voltage in the sample deposited with 4.17 SC. From the Fig 3-9 (c) we see that for the film deposited with silane concentration of 4.2%, the slope of the I-V curve increases after illumination. However, the I-V curves (Fig 3-9 (b) & (c)) of the samples prepared with higher hydrogen dilution, does not exhibit that much sensitivity to the light illumination.

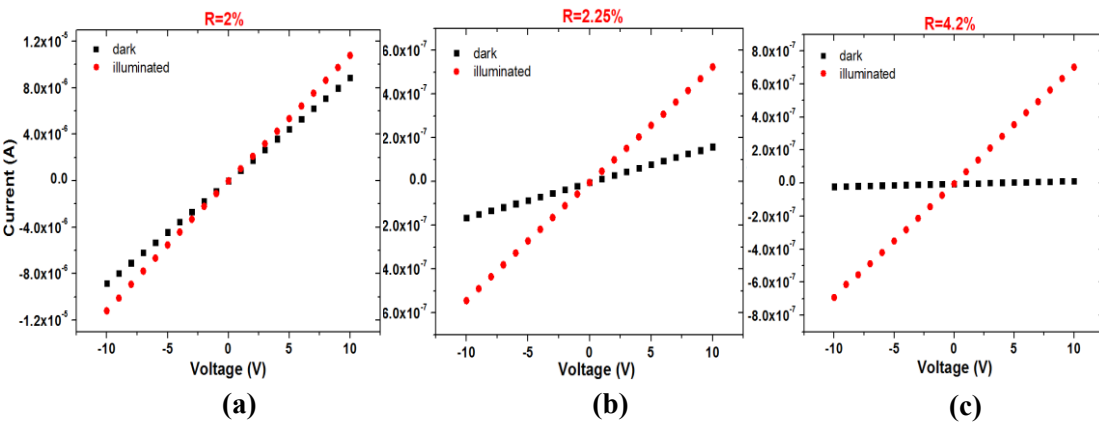


Fig 3-9 Dark and illuminated I-V characteristics for samples with different crystallinity

Photo- and dark conductivity values calculated from the I-V curves are listed in Table 3-5. Dark conductivity increases from 2.15×10^{-6} up to 3.79×10^{-4} with decreasing silane concentration. Photo-response of the deposited film is equal to the ratio of photo-conductivity to dark-conductivity (σ_{ph} / σ_d).

Table 3-5 Calculated conductivity values of the films deposited with different H_2 dilution

SC=[SiH ₄]/([SiH ₄]+[H ₂])	Crystalline Volume Fraction	σ_d	σ_{ph}
4.17	0	2.15×10^{-6}	8.73×10^{-3}
2.25	24 %	2.03×10^{-5}	6.64×10^{-5}
2.00	47 %	3.79×10^{-4}	8.08×10^{-4}

Thus the maximum photo - sensitivity is obtained at 4.17% silane concentration, which is the sample without crystalline phase regime. Even if, dark conductivity of the film deposited with 2% silane concentration is quite high as compared to other two samples, it shows quite low photo-response. One possible reason is related with the micro-voids appear between crystalline grain during the nano-/micro-crystal formation.

In summary, we have shown that the electrical conductivity of the silicon thin films produced in this study depends critically on the crystallinity that depends on the silane concentration.

3.2 Crystallization of Si-Thin Films Deposited by Electron Beam Evaporation Technique

Electron beam evaporation technique is another popular production method, since it is fast, simple and relatively inexpensive. It is generally used for poly-Si thin films fabrication for solar cell applications. In this part of the thesis, crystallization of the Si-thin film deposited by electron beam evaporation technique is investigated. Highly pure Si in the form of chunk is used as feedstock. Si chunks are placed in copper (Cu) crucible, pre-melted by heating and evaporated. The evaporated Si is grown on the substrate whose temperature is controlled by a heater. Substrate temperature is kept constant at 200°C. Amorphous phase Si thin films are deposited on a special glass substrate (alumino-borosilicate AF32®), which is high temperature resistant. It is a well - known that the major advantage of e-beam deposition is the high deposition rate (up to 1 μm/min or higher). During deposition, deposition rate is controlled by altering current density, which flows through the electron emitter (i.e., filament). A thickness monitor is used to measure the deposited thickness. After the deposition process, the a-Si film undergoes a crystallization process called Solid Phase Crystallization (SPC) in a rapid thermal annealing (RTA) chamber. Thus the a-Si film is crystallized and becomes poly-Si with a few microns size of grains [63]. RTA provides ordered crystal structures by removing point defects within the a-Si film in a very short time. During the RTA process, Ar gas is flown through the chamber to prevent oxidation of the film. Since SPC is a high temperature process, it is detrimental to use an appropriate substrate; standard glass is not suitable for this application.

The effect of RTA duration, deposition rate and film thickness on the crystallization of the deposited a-Si is examined by Raman Spectroscopy (RS), grazing incidence X-ray diffraction (GI-XRD) and spectroscopic ellipsometry (SE). It is observed that all these three deposition

parameters have significant influence on the film micro - structure.

3.2.1 Effect of RTA duration

RTA duration is an important parameter that controls phase change from amorphous to poly/micro-crystalline and thus the microstructure of the film. In the first set of experiments, following the fabrication of 450 nm thick films with 1 Å/s deposition rate, RTA duration is altered regularly while temperature is kept constant at 800°C.

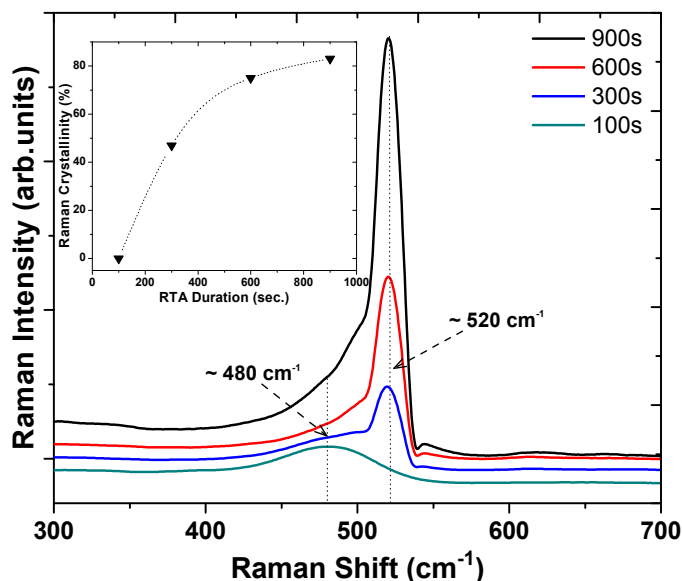


Fig 3-10 Raman spectra of the Si films by RTA at 800 °C for 100, 300, 600 and 900 s. The inset shows the Raman crystalline volume fraction variation of these samples

Fig 3-10 shows the RS of the films annealed with different duration ranging from 100 seconds to 900 seconds. As it is expected, with increasing annealing time, crystalline volume fractions of the films increase. After 100 s annealing, only amorphous phase related broad peak located at around 480 cm^{-1} is observed from RS. Films annealed at 800°C for longer than 300s display the crystalline phase related narrow, sharp peak located at around 520 cm^{-1} . The relative intensity of this peak increases with increasing annealing time; moreover it becomes narrower and sharper. Quantitative estimation on the crystalline volume fraction (X_c) of annealed films is also performed using the method, which is described in the previous section. Inset of the Fig 3-10 shows the change in crystalline volume fraction with annealing time. Raman X_c can be controlled from 0 to 83% by changing annealing time, giving values of 0, 47, 75, 83 % for the annealing duration of 100, 300, 600, 900 s, respectively. These results reveal that the crystallinity of the Si film is further improved by increasing the annealing duration. It is also important to notice that the change in Raman X_c is reduced after 600 s, since the microcrystalline Si film structure approaches saturation.

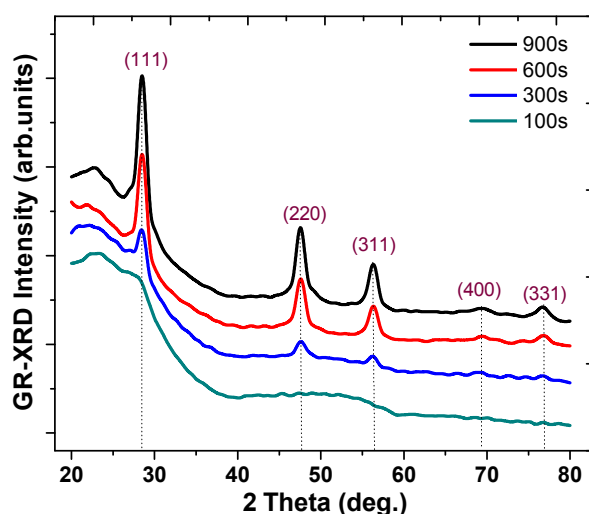


Fig 3-11 XRD spectra of the Si films that is annealed with RTA at 800 °C for 100, 300, 600 and 900 s.

During GI-XRD measurements, the grazing angle between incident beam and film surface was around 1° . Fig 3-11 displays the X-ray diffraction patterns of the Si films after RTA at 800°C for 100, 300, 600 and 900 s. As can be seen from this figure, prominent signature of Si crystals appear in all the XRD spectra, except for the sample annealed for 100 s. The diffraction peaks observed at 28.4° , 47.3° and 56.4° associated with the Si (111), Si (220) and Si (311) plane, respectively. Related diffraction peak intensities gradually increase with the annealing duration. These results suggest that $\mu\text{c-Si}$ films are formed in the case of annealing duration longer than 300 s at 800 °C with RTA process. FWHM of the Si (111) peak is also another important indicator, which shows the crystallization amount of the films. FWHM decreases with annealing time; for 300 s FWHM of Si (111) peak is 0.98° , while it is 0.80° for 600 s and 0.70° for 900 s.

3.2.2 Effect of Deposition Rate

In the second set of experiment, influence of the deposition rate on the crystallization is investigated. Approximately 450 nm thick a-Si films are fabricated with different deposition rates; 1, 5, 20, 50 Å/s. For optical characterization of these films, spectroscopic ellipsometry (SE) measurements are performed in a spectral range in between 240-840 nm (1.5-5.2 eV) at 70° incidence angle with Xenon lamp source.

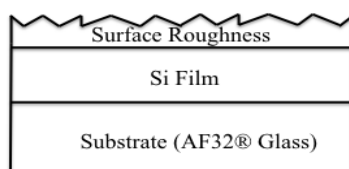


Fig 3-12 Schematic of film structure used as optical model in SE analyses

In SE measurements, it is crucial to incorporate film structure into an optical model. A multilayer optical model based on the structure displayed in Fig 3-12 is used to fit SE data and

obtain quantitative information. The model considers the number of layers covering the substrate as well as their thicknesses and their dielectric functions. For as deposited samples, SE data is interpreted with well-known Tauc-Lorentz (TL) model for the films layer. TL model is commonly used to parameterize the dielectric functions of materials in amorphous phase [64]. The energy dependency of imaginary part of dielectric function (ϵ_i) in this model is given by the following equation;

$$\epsilon_i = \begin{cases} \frac{AE_0C(E-E_g)^2}{(E^2-E_0^2)^2+C^2E^2} \frac{1}{E} & \text{for } E > E_g \\ 0 & \text{for } E \leq E_g \end{cases} \quad (\text{Eqn. 3-3})$$

where E is the photon energy, E_g is the band gap, C is the short range order related broadening parameter, A is the material density related amplitude factor and E_0 is the resonance of the Lorentz oscillator. However, this expression is acceptable for inter-band transition [65]. It is also possible to obtain real part of the dielectric function using Kramer-Kronig relations;

$$\epsilon_r(E) = 1 + \frac{2}{\pi} P \int_0^\infty \frac{E' \epsilon_i(E')}{(E')^2 - E^2} dE' \quad (\text{Eqn. 3-4})$$

$$\epsilon_i(E) = -\frac{2}{\pi} P \int_0^\infty \frac{\epsilon_r(E') - 1}{(E')^2 - E^2} dE' \quad (\text{Eqn. 3-5})$$

Surface the roughness of the film is analyzed with another model called as Bruggeman effective medium approximation. It is assumed that this layer is formed by a mixture of surface SiO_2 (50%) and void (50%). Generally, obtained thickness of the surface roughness is not much more than 4 - 5 nm.

Since the film layer of as deposited samples is modeled with TL, it is possible to parameterize band gap values. Following the fitting, it was observed that band gaps of the related samples are quite low compared to a-Si band gap which is equal to 1.7 - 1.8 eV. Thus in order to increase band gap values of the films, hydrogen treatment is performed at 450°C for 1 hour under N_2 (200sccm) + H_2 (20sccm) flow at RTA system. Before annealing, samples are dipped in a buffered HF solution (40 gr NH_4F + 10ml %49-HF + 60ml DI-water) for 10 second to remove thin native oxide layer, which can block the diffusion of hydrogen atoms.

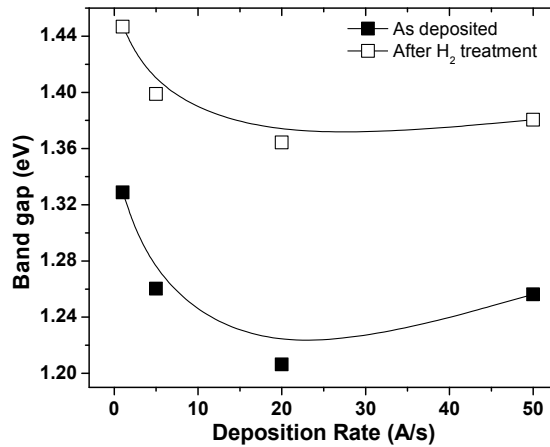


Fig 3-13 Band gap enhancement after 1-hour H₂ treatment at RTA system

Hydrogen is quite important atom that has significant effect on optical and electrical properties of the semiconductor materials. Hydrogen is very small atom having one electron in its shell; therefore it has great diffusivity through the material and extreme chemical activity. Fig 3-13 shows the band gap widening of the films after 1 hour H₂ treatment. Enhancement in the band gap with H₂ treatment is related with the increase in the bonded hydrogen content of the films and more hydrogen incorporation in the a-Si:H layer [66, 67]. It is well known that H₂ atoms can passivate the structural defects via bonding to the energetically suitable site, leading to the increase in the band gap.

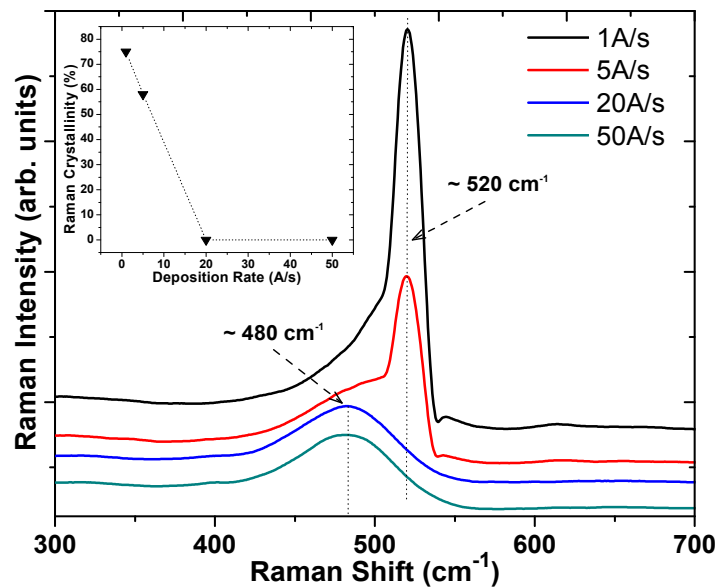


Fig 3-14 RS of the samples, annealed at 800°C for 10min, deposited with various deposition rates; 1A/s, 5A/s, 20A/s and 50A/s.

To observe the effect of the deposition rate on the crystallization, samples fabricated with different rates are annealed with RTA system at 800°C for 600 s. The common practice for the crystallization process is based on a furnace annealing at 600°C for a long time (8-12 hours). However, the aim of this study is not to reach the lowest temperature of the crystallization. In order to accelerate the experiments, RTA system is used and 800°C is chosen as an optimum

temperature. Fig 3-14 shows the RS of the samples after annealing. The lines are shifted for better clarity. As it is clearly seen from the figure, deposition rate has significant influence on crystalline volume fraction of the samples. The spectra of the films deposited with 20 and 50 Å/s rate exhibit only a broad peak located at around 480 cm⁻¹, that confirms completely amorphous structure of the films. On the contrary, the spectra corresponding to the films deposited with 1 and 5 Å/s rate present a sharp, narrow and dominant peak centered at around 520 cm⁻¹ which confirms the presence of the crystalline Si phase within the film structure. Inset of the Fig 3-14 shows the crystalline volume fraction percentage variation with deposition rate. While X_c is equal to 0 for 20 Å/s, it rises abruptly to the 58% for 5 Å/s and 75% for 1 Å/s. This RS results indicate that with decreasing deposition rate, more ordered structure is obtained and crystalline volume fraction increases more effectively after annealing process.

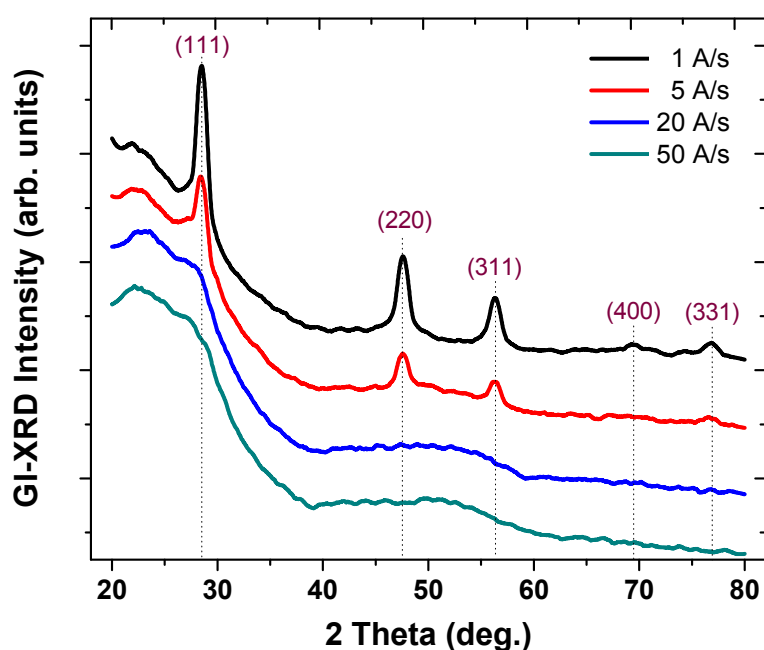


Fig 3-15 XRD patterns of the samples deposited with various deposition rates; 1Å/s, 5Å/s, 20Å/s and 50Å/s and annealed at 800°C for 10min.

Fig 3-15 shows the XRD spectra corresponding to the samples of Fig 3-14. The XRD pattern of the sample deposited with 50 Å/s rate displays a broad background without any diffraction peak. This is a well-known indication of the completely amorphous structure. Sample deposited with 20 Å/s has an XRD pattern with small shoulder that can be seen barely at 27.9°. This shoulder is indicating the onset of crystallization in the Si (111) crystalline plane. As the deposition rate is decreased, the other crystalline orientations can be seen clearly. For 5 Å/s, (111) peak become more intense and two additional peaks attributed to (220) and (311) crystal orientation of Si are observed at 46.26° and 55.79°, respectively. With a further decrease of deposition rate, for 1 Å/s, Si (400) and (331) crystal planes also become slightly clear at around 69° and 76°. The intensity of the (111) peak increases more than the intensities of the any other peaks with decreasing deposition rate. Hence, GI-XRD spectrum reveals that preferential growth orientation of the grains in the deposited films is again (111) crystal plane. Additionally, with decreasing deposition rate, diffraction peaks become narrower. GI-XRD

spectra results are highly correlated with Raman spectra that indicate the crystallization enhancement with reducing deposition rate.

It is also possible to complement the Raman and GI-XRD results with SE measurement. SE is very powerful method that gives additional information about optical and microstructural properties of the materials. The knowledge of optical constant is highly important while analyzing optoelectronic devices. SE measurements are performed in the 1.5 - 5 eV photon energy range at room temperature.

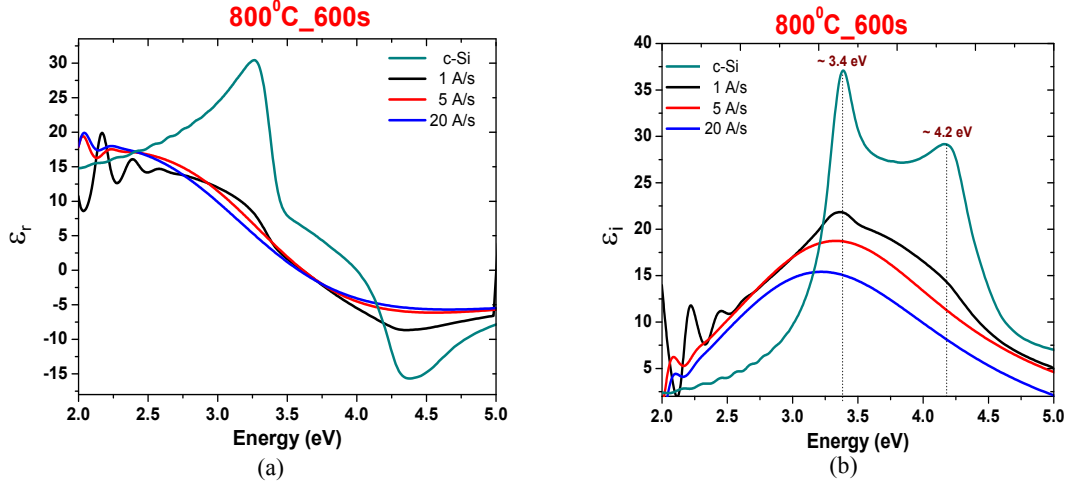


Fig 3-16 Pseudo-dielectric function spectra real part of the complex function (a) and imaginary part of the complex function (b), for the sample deposited with 1, 5, 20 Å/s and reference c-Si.

Fig 3-16 exhibits pseudo-dielectric function spectra for the samples fabricated with different deposition rate and single crystalline Si (as a reference). In the low energy region (1.5- 2.2 eV) spectra shows interference fringes associated with the penetration of light into the material. The optical interference disappears for the photon energy larger than 2.2 eV, as the incident light has been absorbed strongly with no multiple traversal through the film. Optical model illustrated in Fig 3-12 is again used for the analysis of corresponding spectra. For 20 Å/s, pseudo-dielectric function is fitted with TL model, since one broad peak observed in imaginary dielectric function spectrum, which is the typical amorphous tetrahedral material behavior [68]. According to the literature, this broad peak located at $E \sim 3.2$ eV is the signature of a-Si structure. When the rate is reduced to 5 Å/s, TL model does not work very well. To obtain better fittings, Bruggemen effective medium approximation (B-EMA) [69] is carried out. In this approximation, material is considered as a physical mixture of two or more components or phases. Here, the film layer of the sample deposited with 5 Å/s rate is assumed as a combination of fully a-Si and μ c-Si. B-EMA provides accurate calculation for the dielectric function of related layer and is defined as follows;

$$f_a \frac{\epsilon_a - \epsilon}{\epsilon_a + 2\epsilon} + f_{\mu c} \frac{\epsilon_{\mu c} - \epsilon}{\epsilon_{\mu c} + 2\epsilon} = 0 \quad (\text{Eqn. 3-6})$$

$$f_a + f_{\mu c} = 1 \quad (\text{Eqn. 3-7})$$

where f_a and ϵ_a are volume fraction and pseudo-dielectric function of a-Si, while $f_{\mu c}$ and $\epsilon_{\mu c}$ is volume fraction and pseudo-dielectric function of μc -Si and ϵ is the dielectric function of the material [70].

It is seen from the Fig 3-16 that with decreasing rate, broad peak shifts towards higher energy values and amplitude of ϵ_i increases. This amplitude change is explained with the density differences of the material. It is believed that imaginary dielectric function shows its highest value for bulk and dense materials [71]. Thus, amplitude improvement shows that the sample is not in fully amorphous phase anymore. For the sample deposited with 1 Å/s rate, again B-EMA model is used for fitting, however, in this case a void structure is added to the film structure (a-Si + μc -Si + void). Shape of the spectra becomes also relatively different when the deposition rate decreases from 5 Å/s to 1 Å/s, whereas two peaks becomes observable at 3.4 and 4.2 eV. As a reference data, dielectric function spectrum of bulk c-Si is also presented in the same graph. It is seen that these two peaks become more apparent and intense for mono-crystalline Si. According to literature, these two peaks are related with the direct electronic transition in UV-region of the c-Si [72]. Hence, they are direct inter-band transition energies of c-Si and sign of the crystalline phase in the sample. Also, the amplitude of the reference data is the highest one owing to a bulk structure. SE spectra show that transition from fully amorphous phase to crystalline phase is observed with reducing reposition rate. Here, SE spectral results are in good agreement with those obtained from RS and GI-XRD studies.

Table 3-6 Results of the SE spectra analysis obtained for films deposited with 1, 5, 20, 50 Å/s rates. Values of thicknesses, optical constants at 622 nm and Raman crystalline volume fractions.

Deposition Rate (Å/s)	Film Thickness (nm)	Surface Roughness (nm)	X _c (%)	E _g (eV)	n	k
1	441	9	75	1.35	4.09	0.10
5	464	5	58	1.42	4.23	0.19
20	440	6	0	1.47	4.41	0.23
50	406	9	0	1.46	4.65	0.43

Thicknesses of the film and surface roughness are summarized in Table 3-6. As it is mentioned at the beginning of this part, total thicknesses are around 450 nm. Since SE measurements sense mostly the top part of the film, for a reliable comparison of the films deposited with different conditions, they should have same thicknesses. In the contrary case, measured feature would be structural variations as a function of thickness instead of deposition conditions [73]. Optical constants and Raman crystalline volume fractions are also summarized in Table 3-6. Optical band gap decreases with decreasing rate. The film with 75% X_c has the smallest band gap value, 1.35 eV. Band gap increases with X_c reduction. This feature is expected since samples become more like c-Si with 1.12 eV band gap.

It is well known fact that for transparent films, propagation of the light can be determined by refractive index (n) entirely. However, for the films, which have high light absorption capability, propagation of the light cannot be determined only with n . To describe absorption of the film, extinction coefficient (k) is introduced in order to define complex refractive index N ($N = n - ik$). For the films deposited with different rates, obtained n and k values at 622 nm are summarized in Table 3-6, n and k values are increasing with the deposition rate. The refractive index at 622 nm wavelength increases with increasing rate owing to the reducing degree of the crystallinity. In literature it is reported that this decrease is caused by the microvoids that occurs during the crystal formation [74].

3.2.3 Effect of film thickness

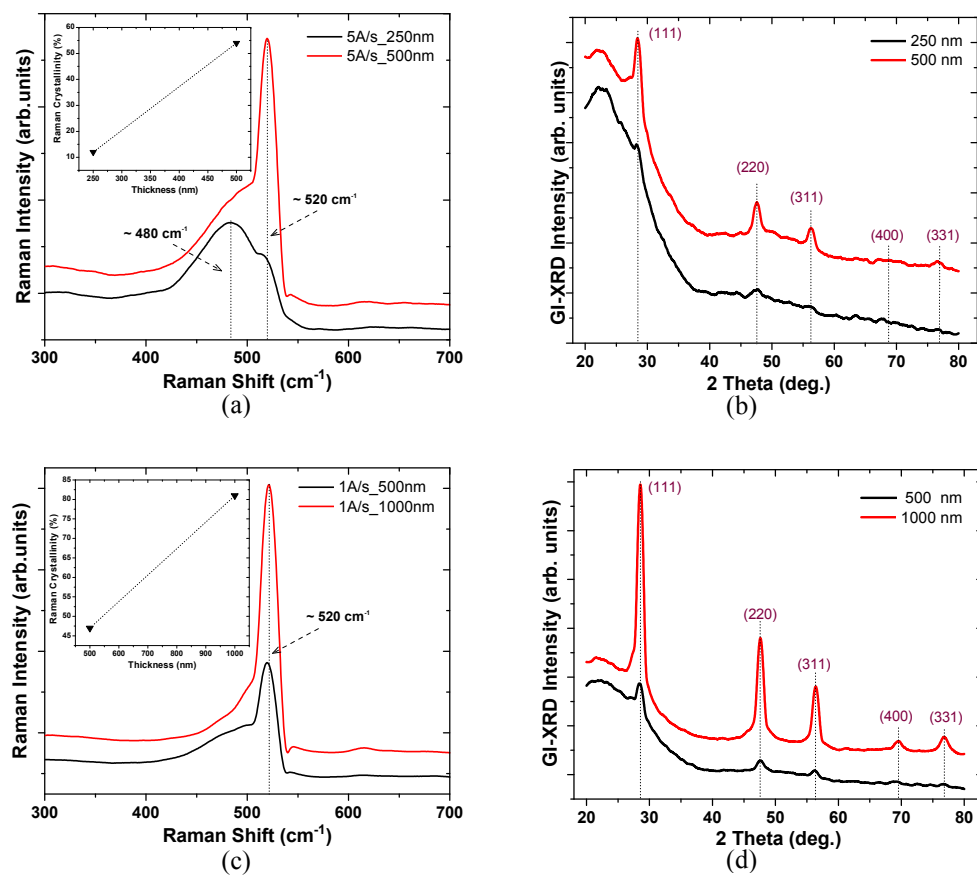


Fig 3-17 RS and GI-XRD spectra of the samples, annealed at 800^oC for 10 minute, deposited with various deposition rates and thicknesses. Two samples with 5 Å/s rate and two different thickness 250 nm & 500 nm (a,b), two samples with 1 Å/s rate and two different thickness 500 nm & 1000 nm (c,d).

Effect of film thickness on crystalline volume fraction is also investigated in this part of the thesis. We have prepared and analyzed two sample sets. In one set, 250 nm and 500 nm thick a-Si thin films are deposited with 5 Å/s rate. After the fabrication, RTA process is applied at 800^oC for 10 minutes for crystallization. As it can be seen from Fig 3-17 (a), for the 500 nm

thick sample, the crystalline volume fraction is equal to 58% while for 250 nm it is around 12%. Besides, Fig 3-17 (b) shows more pronounced diffraction patterns for 500 nm thick samples at the (111), (220) and (311) crystal Si orientations. In the second set, 500 nm and 1000 nm thick a-Si thin films are fabricated with 1 Å/s that is the lowest possible deposition rate in the system used. Following the deposition, samples are annealed with again RTA system at the same temperature for 5 minutes. In section 3.2.2, it is shown that the lowest deposition rate enables the crystallization improvement. We have observed a similar behavior in this case; for 1000 nm thick sample X_c is equal to 81%, while for 500 nm it is 75%. The narrow peak located at 520 cm^{-1} is related to the crystalline phase of Si in the sample and become more dominant for the 1000 nm thick sample (Fig 3-17 (c)). In Fig 3-17 (d) GI-XRD spectra of the same samples are shown. It is clear that for the 1000 nm thick film, more directional growth is observed since Si (400) and (331) crystal planes become faintly clear at around 69° and 76° . Thus, the crystallinity of the film increases with the film thickness. This is expected as the nucleation of the film starts only after certain thickness has been deposited.

3.3 Nanocrystalline Si formation in Silicon Rich Oxide System Deposited by Magnetron Sputtering

Silicon rich silicon oxide (SRO) thin film has been intensively studied because of their importance for optoelectronic integration devices in Si-based technology. However, optical and electrical properties of SRO film has not yet been fully understood, as it is complex and multiphase material composed a mixture of stoichiometric silicon oxide (SiO_2), sub-stoichiometric oxide (SiO_x , $0 \leq x \leq 2$) and elemental silicon (nano-crystal Si). In this part of thesis, properties of SRO films and nano-crystal formation process within this matrix has been investigated. Due to indirect band gap nature and efficient free carrier absorption of bulk silicon, it is considered as an inefficient light emitter material at room temperature. Generally, internal quantum efficiency (η_{int}) is important factor while specifying the light emission ability of the material. η_{int} is defined as the ratio of probability an excited electron-hole pair recombines radiatively to probability of electron-hole pair recombination [36]. For bulk Si, η_{int} is approximately equal to 10^{-6} , which shows non-radiative recombination is predominant. This is accepted as the main reason for poor luminescence of bulk Si. Nevertheless, after discovery of light emission from porous silicon [75], materials compatible with silicon technology and with excellent optical emission properties has been developed. It is reported that engineering silicon into the effective light emitter with designing low dimensional Si systems such as Si nano-crystals dispersed in a dielectric matrix [76] (SiO_2 , Si_3N_4 , et.al.), porous Si, Si nano-pillars, Si quantum dots is possible [77]. Especially, quantum confinement effect led to significant enhancement of the light emission efficiency in Si nano-structures, because radiative recombination probability rises with quantum confinement of the carriers. Most of the studies show that it is also possible to control the emission wavelength by altering the dimension of nanostructures [77]. Photoluminescence peak in the spectrum shows red - shift with increasing the size of nc-Si. However, the origin of the photoluminescence in nc-Si systems is still a topic of discussion. Some scientists believe that luminescence originates from confined carrier recombination while the others suppose an additional localized impurity states in the band gap of nc-Si due to the Si=O double bonds assist the recombination mechanism and cause a PL enhancement [78].

The optical characteristic of SRO is varied with the excess silicon amount within the film and this feature makes SRO attractive to fabricate optoelectronic devices. Here optical and structural characteristics of the films are investigated with different analyzing tools. Crystalline structure of the prepared films is verified both using Raman spectroscopy (RS) and high-resolution transmission electron microscopy (HRTEM). Stoichiometry and volume fractions of the film content are verified with x-ray photoelectron spectroscopy (XPS). SE studies are also performed in order to obtain optical constants and the thickness of the films. Ellipsometric angles Ψ and Δ are measured in a spectral range between 200–1200nm at 70° angle of incidence at room temperature with Xenon lamp. In the light of these analyses, the complex structures of the SRO films are modeled with SE as a mixture of nc-Si, a-Si, poly-Si, void, SiO_x, and SiO₂. By changing the fraction of these components we achieved an optimal model to analyze the SE data. It is also showed that different combination of these material systems can be analyzed with the same approach. The crystallinity in the film was obtained from the SE analysis and compared with those measured from RS. Reasonable agreement is obtained between these two techniques confirming that SE model is successful for the material systems studied here. It is also reported that refractive index and optical band gap of the materials can be controlled easily.

SRO films are fabricated by radio frequency (13.56MHz) magnetron sputtering technique which provides high-quality, well-controlled and homogeneous films [79, 80]. Films are co-sputtered from 99.9% pure Si and SiO₂ targets onto p-type Si (100) wafer and quartz substrates. Nanocrystal formation is observed after thermal annealing of these films with high temperature quartz tube furnace. Prior to deposition Si wafers are cleaned in piranha solution that includes 3:1 volume mixture of concentrated sulfuric acid (H₂SO₄) and 30% hydrogen peroxide (H₂O₂) for 10 minutes in order to remove organic contaminations. Sputtering system is operated in the high vacuum range ($\sim 10^{-6}$) to control and minimize contaminations. Before the evaporation the base pressure of the evacuated chamber is kept at around 5×10^{-6} Torr and the substrate heated up to 200°C. Deposition is done at room temperature and 99.99% pure Ar is used as the process gas. It is a well known fact that SiO₂ dielectric target can not be sputtered easily using DC power source because the accumulation of positive ions on the target surface block the conduction current which is required for maintenance of the plasma. Thus constant RF power, 180 W is applied to 3-inch diameter SiO₂ target. In order to change and control the excess silicon amount of the films, variable direct current (DC) power, in the range of 18-189 W, is applied to 3-inch diameter Si target. During deposition, the Ar flow and sputtering pressure are fixed at 20sccm and 4mTorr, respectively. Approximately 300-350nm thick films are grown and annealing is done for 1hour under constant flow of N₂ at 1100°C. This post-annealing process is the vital point of phase separation and Si nanocrystals nucleation within the oxide.

3.3.1 Structural Characterization

XPS, RS and HRTEM were performed for structural characterizations of the sputtered and post-annealed films. In order to change the excess Si amount, the applied DC power to the Si

target was increased gradually from 18W to 189W, while applied RF power to the SiO₂ target was kept constant. Four different powers were applied to the Si target: 18, 81, 126, 189 W.

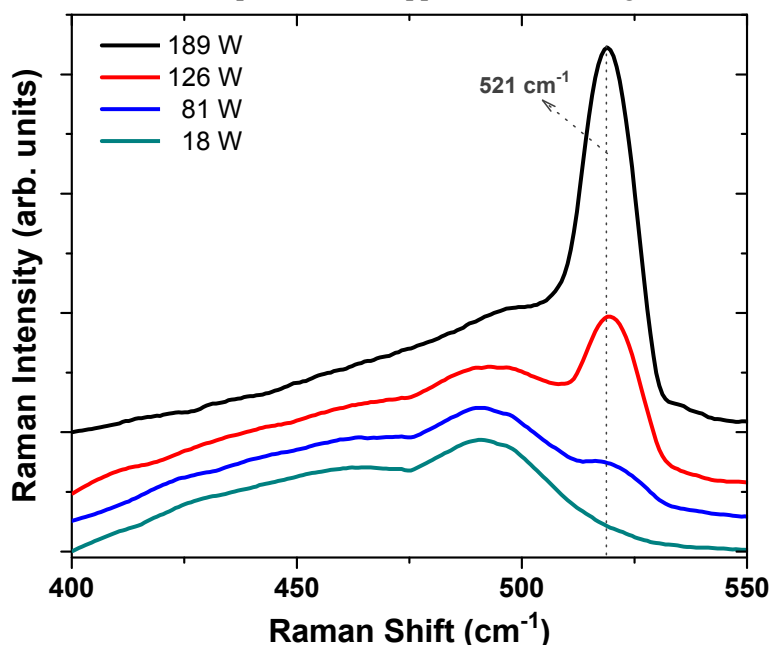


Fig 3-18 Raman measurement of the films deposited with different Si-target power and annealed at 1100°C.

During the XPS measurements, samples deposited on c-Si wafer substrate are used. XPS results present that the stoichiometry of the system can be tailored by changing the amount of excess Si delicately. For the SiO_x film deposited with 18 W Si target power, x value is equal to 1.72, for 81 W, 126 W, 189 W; it is equal to 1.07, 0.95 and 0.51, respectively. Thus with increasing power, excess Si amount is increasing according to the XPS measurements. In Fig 3-18 Raman spectra of the films deposited with different Si target power and annealed at 1100°C for 1 hour are illustrated. During Raman spectra analyses, samples deposited on quartz substrate are used. According to the RS, the sample deposited with 18 W power shows a broad transverse optical band associated with amorphous Si structure and no crystal phase related peak. Nevertheless, for 81 W small shoulder located at around 521 cm⁻¹ is observed which can be assumed as an evidence of nano-crystal formation. With a further increase of Si target power, spectrum consists of a well-ordered crystal phase related narrow band at 521 cm⁻¹ and broader band at lower wavenumber from disordered Si inclusions. Peak located at 521 cm⁻¹ become sharper and dominant with increasing applied power. Thus, Si and O concentrations have great significance on spectral features of sputtered and post-annealed thin films. These results indicate that deposited films containing high excess Si atoms, are crystallized more easily after high temperature furnace annealing process.

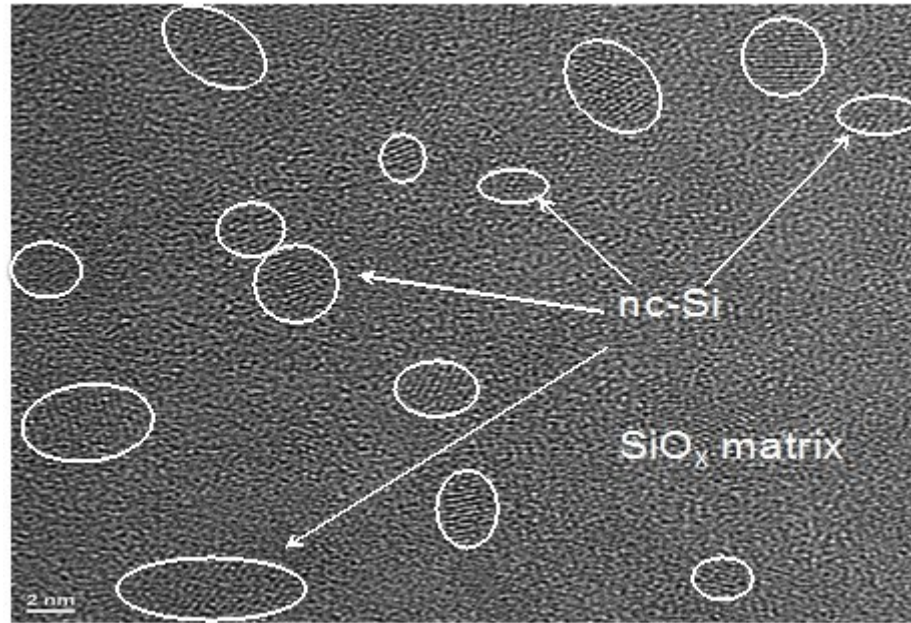


Fig 3-19 HRTEM image of nc-Si within SRO film deposited with 81W Si-target power and annealed at 1100^oC for 1 hour

Besides RS analysis, nanoscale crystal formation within the films is also confirmed via HRTEM analysis. Fig 3-19 shows the plan view HRTEM image of the film deposited with 81W ($x=1.07$) and annealed at 1100^oC for 1 hour. As it can be seen from the figure, small Si nanocrystals that have diameters of a few nano-meter are surrounded by mostly amorphous SiO_x matrix. Lattice fringes are marked with white circles for better view.

3.3.2 Optical Characterization

In order to investigate optical features of those samples, room temperature PL and ES measurements are performed. For both analyses, samples deposited on c-Si wafer substrate are used and all of them have the same thickness of 300 nm. Fig 3-20 shows PL spectra of the samples with different excess Si amount. As it is mentioned above, with increasing Si target power, excess Si amount is also increasing. After high temperature furnace annealing procedure, sample that have quite high excess Si (189 W, $x=0.51$) and low excess Si (18 W, $x=1.72$) shows no luminescence feature. However, for the other two samples, strong improvement of the PL intensity can be observed. Associated with high temperature annealing, phase separation of the SRO films lead to the formation of Si-nanocrystals surrounded by SiO_x matrix (Fig 3-19). According to the HRTEM images (not all of them are shown here) the mean crystal sizes increase with increasing Si concentration of the films correspondingly. Same feature was also observed in the study of Kahler et al. [81]. As there is no Si nanocrystal formation through the sample with very low excess Si (18W), according to the RS and HRTEM analyses, the film structure can be defined as completely amorphous. It can be seen clearly from the Fig 3-20, there is no PL signal for this sample. With increasing power (excess Si amount), small clusters in crystalline phase appear within the SiO_x matrix (Fig 3-20). Sample deposited with 81 W power shows a strong PL signal located at around 850 nm. This signal is attributed to the presence of Si-nanocrystals, which cause the quantum

confinement effect. With rising power, excess Si amount and nanocrystalline size increase. Sample deposited with 126 W power shows also strong PL signal located at around 900 nm. PL spectra indicate that, when crystal dimensions become larger, shifting of emission through the larger wavelength from 850 nm to 900 nm (red-shift) is observed [81]. For the film with high excess Si (189 W), nanocrystalline clusters become too large to display the quantum confinement effect (> 7 nm). Due to the in-direct band gap nature of c-Si, quantum confinement effect become weaker with increasing excess Si content, as a result PL signal vanishes [82].

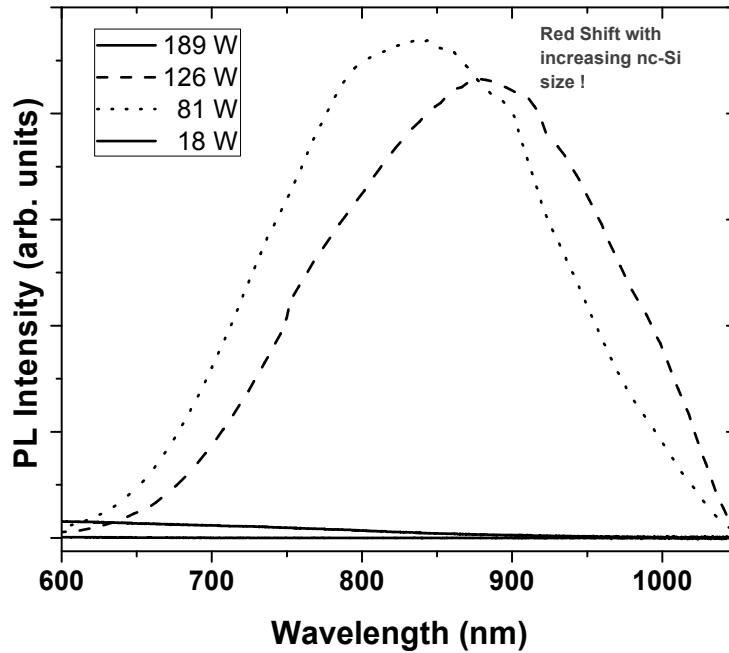


Fig 3-20 PL analyses of the films deposited with different Si-target power (different excess Si amount) and annealed at 1100°C for 1 hour.

In order to determine optical constants and dielectric functions of the sputtered and annealed SRO films, SE measurements were performed. Crystallization after high temperature furnace annealing process is also presented with SE analysis. SE data is interpreted with Tauc-Lorentz (TL) and Bruggeman effective medium approximation (BEMA) models. As it is mentioned before, TL is used for the parameterization of the optical functions for a-Si and insulator matrix whereas a combination of TL and BEMA is used for the parameterization of optical functions for more complex film structure. In our case this complex film structures consist of different volume fraction of a-Si, nc-Si SiO_x , SiO_2 , and void components.

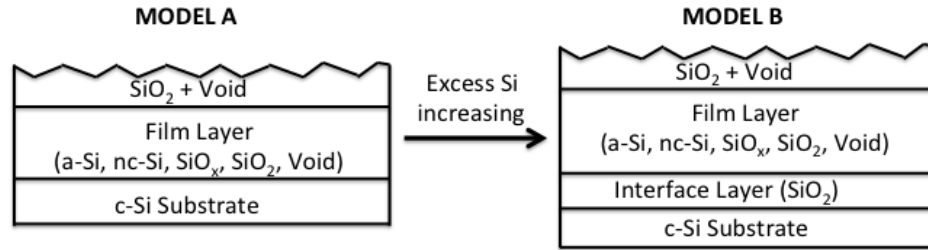


Fig 3-21 Schematic of the film structure used as optical models in SE analyses for the films with low excess Si (a) and for the films with high excess Si (b)

We introduce two simple optical models (Fig 3-21) with different layering to describe SRO thin films deposited with different Si target power and have different excess Si content. Optical model shown in Fig 3-21(a) works perfectly for the film that has low excess Si, but despite extensive efforts, we are not able to fit measured SE data using this model for the film that has high excess Si content. Only when an additional thin interface layer was introduced in between film and substrate Fig 3-21(b), a good fit for the sample that has high excess Si can be performed. This may be explained by the nature and distribution of sub-species in this complex system.

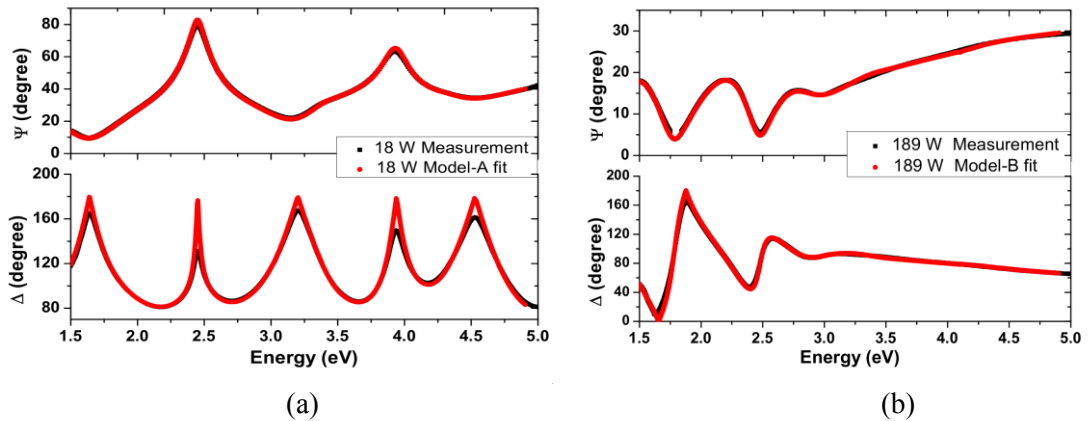


Fig 3-22 SE spectral data and their fitting by applying TL and BEMA to the models for SRO film deposited with 18 W (a) 189 W (b) Si-target power

As can be seen from Fig 3-22, complicated spectral features (Ψ , Δ) can be fitted excellently in Si-rich and Si-poor regimes via optical models shown in Fig 3-21. Two representative SE spectra are shown in Fig 3-22 (a)&(b), in order to show that our proposed model is a generic for both Si-rich (189 W, $x=0.51$) and Si-poor (18 W, $x=1.72$) regimes. SE data of the film deposited with 81 W was modeled with Model A (Fig 3-21 (a)) while for 126 W Model B (Fig 3-21 (b)) was used. This means that the generated optical models describe related regimes perfectly. Fig 3-22 also gives another significant information on crystallization. Fig 3-22 (a) is extremely similar to very well known SE spectral data of SiO_2 , which has excessive oscillatory behavior. This is not a surprise since it is known from XPS analysis that in Si-poor regime, SiO_2 dominates the film structure. Fig 3-22 (b) shows a decrease in oscillations and a broad feature between 3 and 5 eV photon energies, which indicates the formation of nc-Si regions as confirmed by RS and HRTEM. The oscillations are decreased in Si-rich regime and

the broad feature between 3 and 5 eV become quite prominent. This clearly shows the presence of nc-Si in the system. After the proper fittings, optical constants and concentration of the sub-species of the samples are obtained. Refractive index of the films can be controlled from 1.45 to 2.8 with increasing excess Si amount (decreasing oxygen content) and band gap energy is controlled from 3.9 eV to 1.8 eV. For the sample deposited with 18 W refractive index is 1.4 and band gap is 3.9, it is quite expected since the film consists of mostly SiO₂.

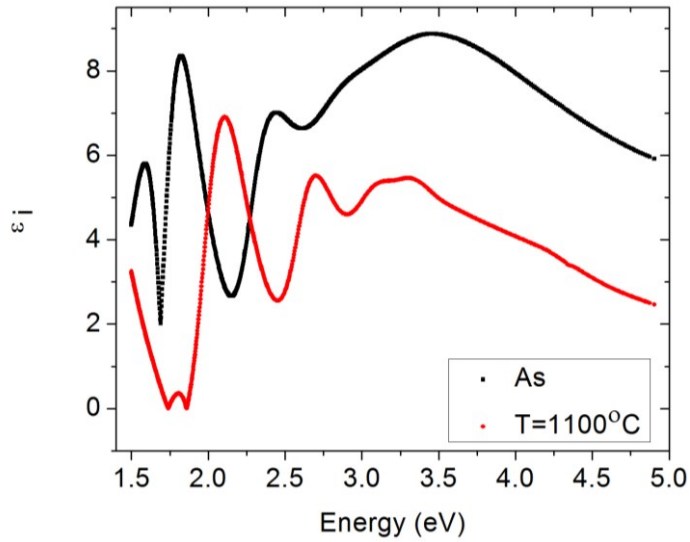


Fig 3-23 Annealing dependence of imaginary dielectric function (ϵ_i) for the SRO film deposited with 189 W Si-target power

Next, the dielectric functions of SRO films were extracted from spectral features (Ψ , Δ) in order to investigate their crystal formation dependency. For this purpose, temperature-dependence of the imaginary dielectric function is presented in Fig 3-23. As expected, Fig 3-23 shows a significant spectral shift with annealing. After annealing, Si starts to crystallize from SRO; this leads to a shift in the spectrum towards higher energies (blue-shift) and two slightly prominent features starts to appear at ~ 3.3 eV and ~ 4.3 eV, respectively. These are attributed to the critical points (CP) of c-Si; 3.3 eV for E1 and 4.3 eV for E2, respectively [83]. Although amplitudes of these points are higher and the feature is narrow, CP of nanocrystals shows both broadening and decreases in amplitude since their size distribution smears the transitions [84]. Since crystal sizes are much smaller than the wavelength of used light, it is not possible to gather primary information (directly from individual nanocrystals) but it is possible to gather secondary information (a function of average nanocrystal density) from nanocrystals. Two slightly appeared CP features in sample deposited with 189 W Si-target power and annealed at 1100°C indicates the presence of nc-Si. As formed nc-Si diameters are very small compared to c-Si, prominent CP features cannot be expected. It is also observed in numerous studies that the amplitudes of CP decreases and CP features broaden significantly due to small nanocrystal sizes [85]. One reason may be the neglect of excitonic effects, which are important in bulk spectra [85]. Agocs et. al. explained the amplitude decrease and broadening phenomenon as a consequence of increasing porosity, hence increasing grain boundaries in their work [86]. Lee

et. al. made a similar observation and concluded that this can be attributed to the inadequacy of band structure in nanocrystallites due to their extremely small volume and increased surface effect [87, 88].

As it is mentioned before, structural information about the thin films can be obtained via TEM images. In Fig 3-24 cross-sectional bright field TEM images of two different samples, which have different excess Si amount, are shown. It is better to notice that, when electron beam passes into the film, numerous electrons are diffracted via inelastic scattering owing to interactions. Bright field TEM image is obtained from the primary beam passing through the film and diffracted beams that are rejected. Rejected beams create dark fields while the passing beams generate bright fields. In this complex film structure Si nano-crystals cause the diffraction of the electron beam, as a result of this, they look like dark points in bright field image. In our case, bright areas can be considered as the film matrix SiO_x and dark areas can be considered as Si nano-crystals.

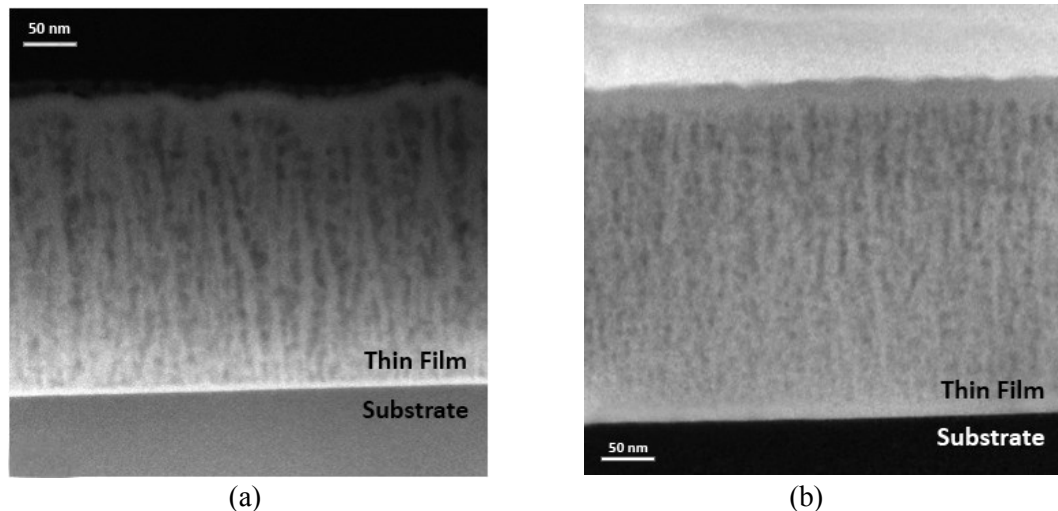


Fig 3-24 Cross-sectional bright field TEM images of the films deposited with 126 W (a) and 81 W (b) Si target power

Fig 3-24 (a) and (b) shows the cross-sectional bright field TEM images of the films deposited with 126 W and 81 W power, respectively. According to the XPS and SE results, the oxygen content of the films decreases with increasing Si target power. Fig 3-24 (a) is the image of the film that has more excess Si and thin SiO_2 interface layer can be seen clearly. Nevertheless, for the film deposited with 81 W the interface layer merge with film structure as the film content is mostly oxide (Fig 3-24 (b)). These film structures are highly correlated with the optical models (Fig 3-21) that are used for SE spectral data analyses and fittings. Introducing an interface layer was substantial for fitting.

Table 3-7 Volume fractions calculated from XPS peak fitting and SE spectral data fittings

Power (W)	XPS (%)		SE (%)		
	Si	SiO ₂ +SiO _x	SiO ₂ +void	Poly-Si	a-Si
189	49	52	14	34	40
126	12	87	81	9	10
81	8	92	84	5	11
18	0	100	100	0	0

XPS data presented in Table 3-7 is extracted from peak fittings of XPS Si 2p signal, whereas SE data presented in the table is extracted from SE spectral data fittings. Amount of Si volume fraction in XPS column is the percentage of total Si-Si bonds, whereas amount of (SiO₂+SiO_x) shows all Si-O bonds extracted from Si 2p signal. We calculate the amounts of Si₂O, SiO, Si₂O₃, and SiO₂ species separately but for the sake of simplicity we combine them here and include in (SiO₂+SiO_x). Since we cannot include every SiO_x species in SE calculations, we introduce the amounts of Si₂O, SiO, Si₂O₃, and SiO₂ species together as (SiO₂+void) in SE column. Also we include poly-Si and a-Si in SE calculations to represent Si species in the structure. We should stress out that (SiO₂+void) and a-Si volume ratios given in SE column are correlated with (SiO₂+SiO_x) volume fraction given in XPS column. As can be seen from the table, the amount of volume fractions used in SE spectral data fittings is highly correlated with XPS results.

In summary, generic model is presented in order to analyze spectral SE data of SRO system with different excess Si content. Obtained HRTEM images demonstrate that introduced optical models are highly similar with the real film structure. Additionally, subspecies within the SRO films are analyzed via two different techniques that give consistent results. With same approach, changing excess Si content of the films can control optical constants and subspecies.

CHAPTER 4

STRUCTURAL PECULIARITIES AND AGING EFFECT IN Si-THIN FILMS PREPARED BY ICP-CVD

Si thin films with sufficiently good quality have been commonly fabricated by plasma enhanced chemical vapor deposition (PECVD) with a capacitively coupled plasma (CCP) configuration [89]. However, this technique has some drawbacks, especially for nc-Si thin film deposition, because it requires high deposition pressures and powers, which result in powder formation, delamination of the film due to accumulated stress on surface and directional high-energy ion bombardment of the film [90, 91]. Since H₂ plays a critical role in nucleation [92], nc-Si thin films are deposited only when SiH₄ is heavily diluted with H₂, which leads to a decrease in the deposition rate and an increase in gas and power consumption [93]. To overcome these drawbacks, high-density plasma sources such as an inductively coupled plasma (ICP) source, which is a rich ion and radical source, have been recommended. This technique has been demonstrated as versatile and powerful way of nc-Si thin films fabrication. ICP provides higher deposition rates owing to its higher dissociation capacity and low plasma sheath potential that reduces the ion bombardment rate. The high dissociation capacity also leads to crystallization at low-temperatures, which is very important for applications on thermo-sensitive flexible substrates [94]. Finally, uniformity of the plasma in the radial and axial directions provides a good spatial homogeneity in the deposited film [95].

In this chapter, the structural peculiarities observed in a-Si and nc-Si thin films fabricated by ICP-CVD and the effect of aging on the chemical properties of these materials were investigated. The influence of deposition pressure and power on structural properties was also studied. In agreement with previous reports, it is observed that crystal formation was possible even at low temperatures [96]. The film grew in a columnar fashion with a high porosity and a fairly rough surface topology. These columnar structures appeared to be independent of the amorphous and crystalline nature of the films. Further investigation of the structure revealed that the columns consist of structures resembling cauliflower. Furthermore, it is shown that these cauliflower-like Si nanostructures oxidize gradually and uniformly throughout the film when exposed to air due to their highly porous nature and continue to do so for up to several days' weeks.

Aim of this study was to investigate structural and morphological transition from the amorphous to micro/nano- crystalline phase in Si-thin film samples deposited by ICP assisted CVD technique. In order to understand the effect of the plasma environment OES analyses were performed during the deposition. Afterwards; RS, SEM and HRTEM measurements were conducted for structural investigations. It is observed that films have been growing in columnar fashion with highly porous nature. To support this conclusion XPS and FTIR aging analyses were performed.

500 nm thick a-Si:H and nc-Si:H thin films were fabricated by ICP-CVD onto p-type (100) Si wafer with a resistivity of 10-20 Ω -cm and Corning Eagle-XG glass substrates using %90 H₂ diluted SiH₄ at room temperature. However, due to radiative heating and a high flux of energetic ion bombardment, substrate temperature may have been slightly higher than the room temperature [97]. The inductive source, manufactured by CCR and incorporated into a plasma thin film cluster tool (Fig 2-2) by Vaksis Company, was operated at a radio frequency (RF) of 13.56 MHz. Schematic diagram of the ICP system has been illustrated in Chapter 2 (Fig 2-6).

Table 4-1 Deposition parameters for the samples fabricated via ICP-CVD technique

Deposition Power	SiH ₄ Flow	H ₂ Flow	Deposition Pressure	Deposition Duration
2000 - 3000 W	9 sccm	81 sccm	10 - 50 mTorr	8 - 15 min

The total deposition pressure and deposition power was varied to control the structure and morphology of the films. Deposition parameters of the films fabricated by ICP-CVD method are shown in Table 4-1. During deposition, the SiH₄ flow and its dilution held constant at 9 sccm and %90, respectively. In first set of experiment, deposition power effect was investigated, while in the second part pressure effect was studied.

4.1 Effect of Deposition Power

Deposition power was varied from 2500 W to 3000 W in order to observe structural phase transition. Since the chamber volume is quite large (35 cm x 35 cm x 15 cm), high power values were used for deposition. In lower powers, transition is not observed; only amorphous Si structure was obtained.

4.1.1 Plasma Diagnostics and Deposition Rate

Fig 4-1(a) shows the deposition rate change with applied power density. It is obviously seen that deposition rate is increasing with increasing power.

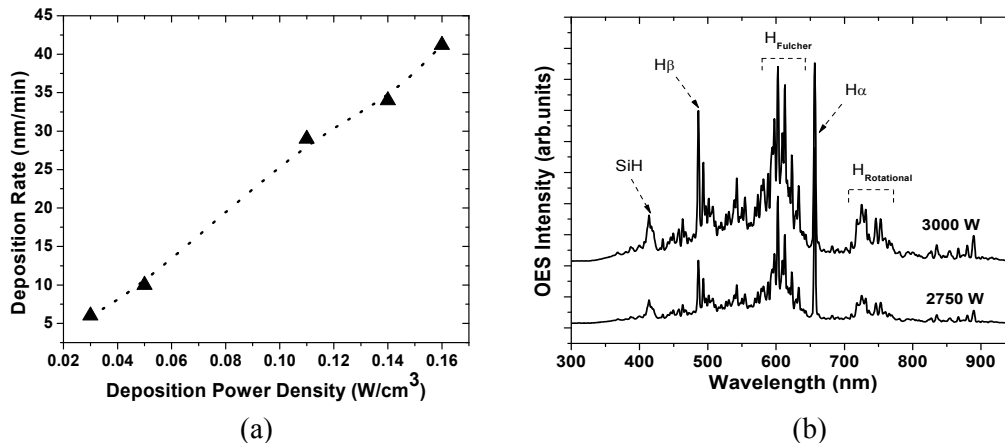


Fig 4-1 Applied power density dependence of deposition rate (a) and OES emission lines for the two different samples deposited at different power density (b).

Thicknesses of the deposited films were confirmed by cross-sectional SEM images and for deposition rates calculations, thicknesses have been divided by deposition duration. Deposition rate increment with power is an expected result since high power provides more elastic collision within the plasma. More collision causes the enhancement in dissociation of the feed-gases and this facilitates the higher deposition rate. Normally, in conventional CCP-PECVD system, high power cause high energetic ions in the plasma. These highly energetic ions lead the heavier ion bombardment through the surface of the producing film since two parallel electrodes create electric field between them and orientate the energetic ions through the substrate. Increasing applied power to the top electrode increases the electric field between top electrode and grounded bottom electrode, which has a substrate on the top. Enhancement in e-field creates faster ions and heavier bombardment, which is assumed as a main reason for the deterioration of film quality. However in ICP-CVD system, there is no ions orientation through the substrate, uniform plasma is created in the large quartz chamber surrounded by the induction coils. Hence, with increasing power it is possible to enhance deposition rate without causing deterioration in the film structure via ICP-CVD system. Fig 4-1 (b) shows the optical emission spectra of highly H₂ diluted SiH₄ RF discharges with two various different powers. As it is mentioned in Chapter 2, OES utilizes to investigate excited SiH*, Si* and H* that are formed by dissociative excitation in electron collision with feed-gas SiH₄, however SiH₃ and SiH₂ species cannot be detected with this tool [98, 99]. The thin vertical dotted lines specify the positions of commonly used emission lines for plasma analyses. H_α*, H_β*, and SiH* reactive species that can be detected in an OES spectrum with emission signals located at 656 nm, 485 nm, and 412 nm, respectively [23]. It is obviously seen from Fig 4-1 (b) that intensities of the emission lines are highly related with the applied power since power effects directly the density of the electrons within the plasma. Thus, with increasing the plasma power while keeping all other parameters constant (flow rate, pressure, temperature, etc.), an increase in SiH* and H* emission and deposition rate is observed. This result is highly correlated with the literature [100].

4.1.2 Crystallinity

RS of the samples deposited with various powers is illustrated in Fig 4-2. It has been well recognized that Si:H comprises three phases in terms of Raman scattering shift that deconvoluted with three Gaussian peaks : the amorphous phase (~480cm⁻¹), intermediate phase (~510cm⁻¹) originates from the defective part of the crystalline phase associated with grain boundaries, crystalline phase (~520cm⁻¹) comes from transverse optical (TO) mode of Si-Si vibrations in the crystalline phase. For the sample deposited with 2500W power (0.14W/cm³ power density) only small shoulder at the 520 cm⁻¹ is observed. With increasing power, crystalline phase related peak become sharper and enhancement in crystallization is observed clearly. This can be explained with again the high dissociation of the feed gases due to the high deposition power. More dissociation creates more additional hydrogen, which are able to passivate more dangling bonds by forming isolated Si-H bonds and create more ordered film structure. Inset of the Fig 4-2 crystalline volume fraction change with deposition power is shown. For the sample deposited with 2500 W power Raman crystalline volume fraction is equal to 14%. For the 2750 W power, it becomes 27% and further increasing, crystalline volume fraction value reaches 49% for the sample deposited with 3000 W power. It is very

interesting and essential to obtain nearly 50% crystallization at room temperature PECVD deposition.

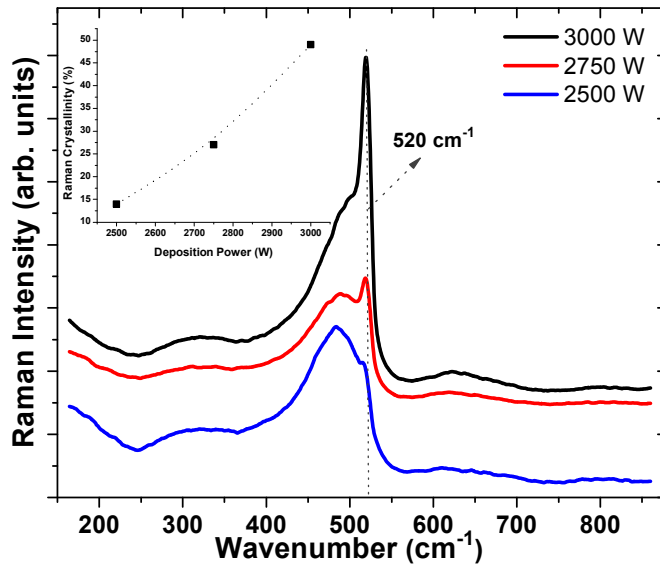


Fig 4-2 RS for the ICP-CVD deposited samples with various power

Fig 4-3 shows the XRD spectra corresponding to the samples of Fig 4-2. The XRD pattern of the sample deposited with 2500 W displays a broad background and small diffraction peaks related with (111), (200) and (311) crystal orientation of Si. These small shoulders are indicating the crystallization in the different Si crystalline planes. As the deposition power is increased, peaks attributed to (111), (220) and (311) planes of Si become sharper. With a further increase of deposition power, Si (400) and (331) crystal planes also become slightly clear at around 69° and 76° . The intensity of the (111) peak increases more than the intensities of the any other peaks with increasing deposition power. Hence, GI-XRD spectrum reveals that preferential growth orientation of the grains in the deposited films is (111)-plane.

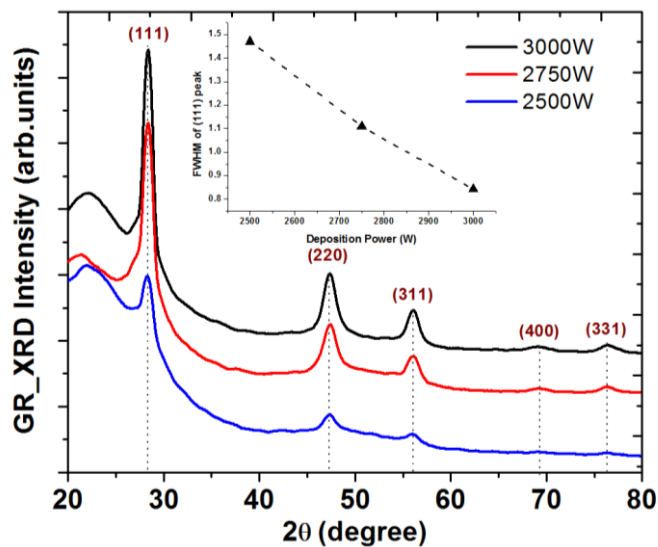


Fig 4-3 GI-XRD spectra for the ICP-CVD deposited samples with various power

Inset of the graph Fig 4-3, changes in FWHM values of the Si - (111) crystal orientation related peak with deposition power is presented. It is clearly seen from the figure that with increasing power, FWHM of the peak decreases from 1.5° (2500 W) to 0.8° (3000 W) that reveals the enhancement of the crystallization. As a result, GI-XRD spectra results are highly correlated with Raman spectra that indicate the crystallization enhancement with increasing deposition power.

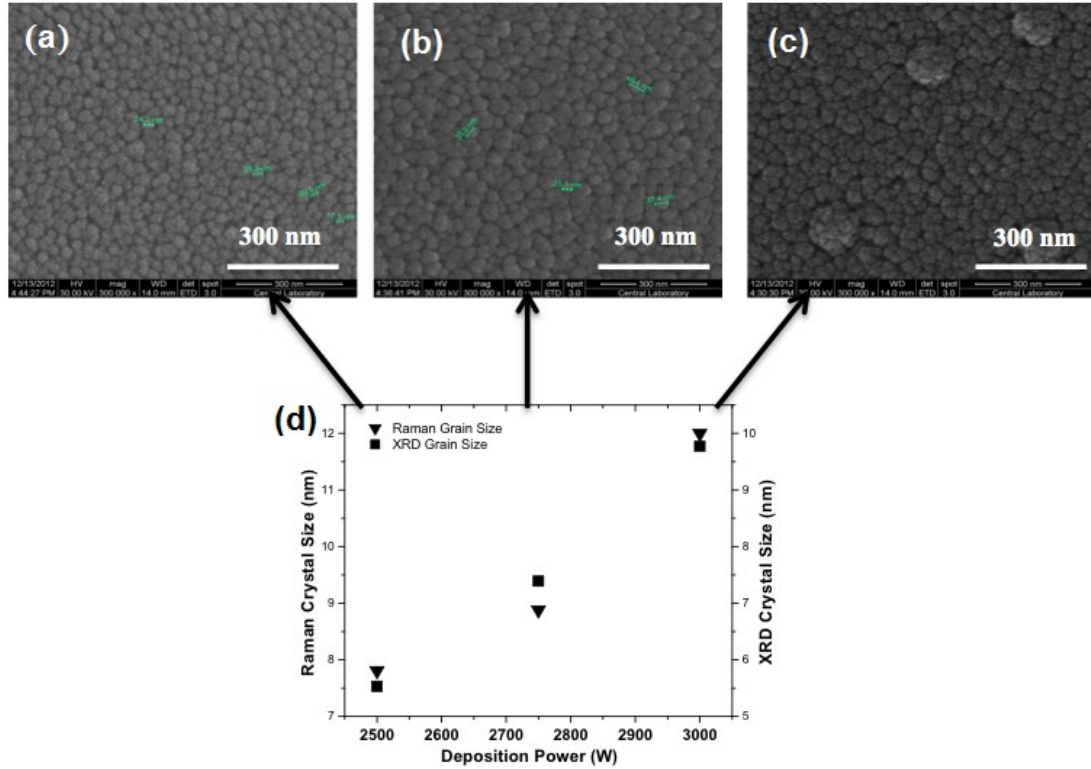


Fig 4-4 SEM images of the samples deposited with various power 2500 W (a), 2750 W (b), 3000 W (c) and Comparison of the calculated grain sizes with RS and GI-XRD (d).

As it is mentioned in Chapter 2, it is possible to calculate crystal size via Raman and XRD spectra. For the average grain size estimation via RS, wavenumber shift of TO mode of Si-Si vibration from 520 cm^{-1} wavenumber should be determined. According to empirical relation, crystal size upsurges from 7.8 nm to 8.9 nm and 12 nm with increasing power from 2500 W to 2750 W and 3000W, respectively. In order to determine XRD grain size well-known Debye-Scherrer formula is used. According to the GI-XRD spectra, estimated grain sizes are equal to 5.6 nm, 7.4 nm and 9.8 nm for the sample deposited with 2500 W, 2750 W and 3000W power, respectively. Hence, it is also observed from XRD spectra that grain size upsurges with increasing power. Difference in the sizes estimated from RS and XRD spectrum is equal to approximately 2 nm for all three samples. Fig 4-4(d) shows the comparison of the estimated crystal sizes with RS and GI-XRD, this reveals that both methods give reasonable and consistent grain sizes. In Fig 4-4 (a), (b) and (c) SEM images of the samples deposited with 2500 W, 2750 W and 3000 W are shown. The grain profile of the Si-thin films become sharper and the grain size upsurges with the process power according to the SEM images. Lien et al. claimed that grain size distributions strongly depend on the reactive SiH^* and H^* emissions in

OES. According to their study, increase in the excited radicals can be the reason of the crystalline phase enhancement [100].

4.2 Effect of Deposition Pressure

Deposition pressure was varied from 50 mTorr to 10mTorr in order to observe structural phase transition from amorphous to micro/nano-crystalline Si. Deposition power is kept constant at 3000 W. All other deposition parameters are shown in Table 4-1.

4.2.1 Plasma Diagnostics and Deposition Rate

The glow discharge mechanisms during the deposition of a- and nc-Si and the influence of deposition pressure on plasma properties are investigated. Fig 4-5(a) shows the results of OES of highly H₂-diluted SiH₄ plasma as a function of the deposition pressure. Additionally, Fig 4-5 (b) shows the intensity of signals originated from reactive species, which can be detected by OES. In general, the deposition rate increased with deposition pressure in correlation with an increased amount of reactive radicals such as SiH^{*}, H_α^{*}, and H_β^{*}. When the deposition pressure is increased, the numbers of molecules inside the vacuum chamber at a constant silane gas flow also increased because there were more SiH₄ molecules to dissociate into reactive radicals.

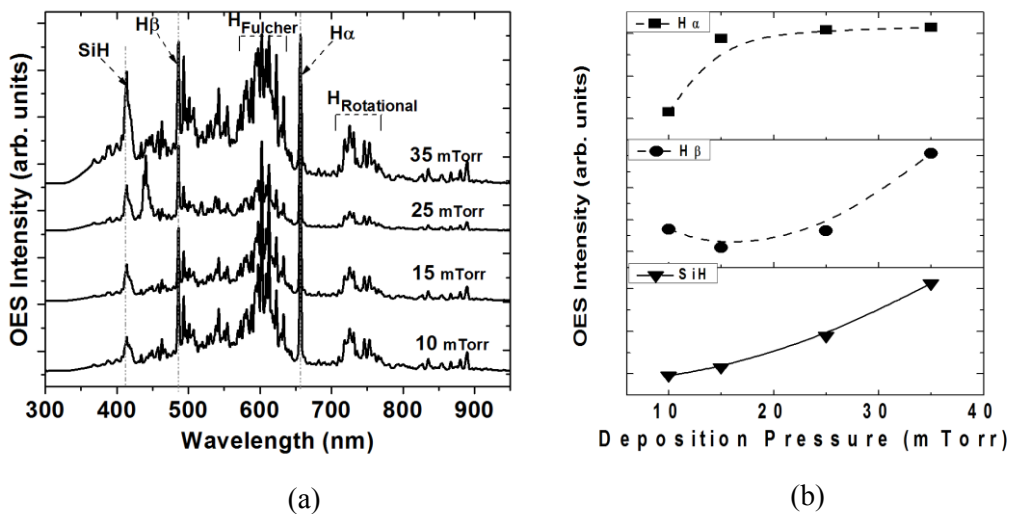


Fig 4-5 The effect of deposition pressure on optical emission spectroscopy (OES) spectra of the thin films (a), OES intensity change as a function of the deposition pressure of detectable plasma species (b).

It is well known that ICP provides sources of favorable reactive species, leading to a high deposition rate. The variation of the deposition rate as a function of deposition pressure is not presented here, however deposition rates as high as 65 nm/min were reached at high deposition pressures. The observed deposition rates in this study were significantly higher than those obtained with a conventional PECVD system equipped with an RF source. Only a very high frequency PECVD system is able to achieve similar deposition rates [101, 102].

The SiH signal located at 414 nm is a measure of the silane depletion rate [103]; the depletion rate increases as the intensity of this peak diminishes. In agreement with previous observations [103], we found that the transition from the amorphous to micro/nano-crystalline phase occurred when the SiH peak decreased, which means that crystallinity is strongly affected by silane depletion. In this study, the highest crystallinity was observed at the lowest deposition pressure, which is associated with the highest silane depletion rate.

4.2.2 Crystallinity

RS and XRD measurements were performed to estimate the crystal volume fraction of the a- and nc-Si thin films. Fig 4-6 shows the RS spectra of the samples prepared at different deposition pressures. It is well recognized that the Si:H RS signal is comprised of three phases: the amorphous phase ($\sim 480\text{cm}^{-1}$); intermediate phase ($\sim 510\text{cm}^{-1}$), originating from the defective part of crystalline phase associated with grain boundaries [4]; and crystalline phase ($\sim 521\text{cm}^{-1}$), related to the transverse optical (TO) mode of Si-Si vibrations [104]. It is also obvious from Fig 4-6 that the c-Si signal increased and became sharper as the deposition pressure was reduced, which suggests that the crystalline phase becomes dominant due to enhanced crystallization.

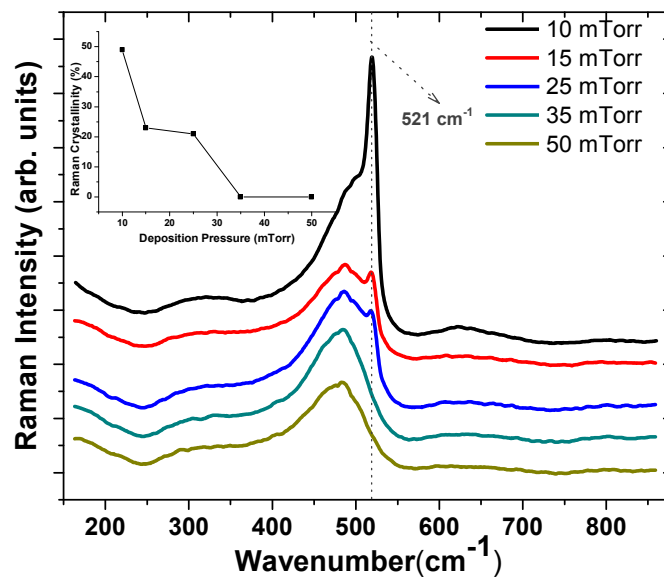


Fig 4-6 RS spectra of the samples deposited at different deposition pressures

According to the RS, when the deposition pressure was above 25 mTorr, the film remained in the amorphous phase; when the pressure was below 25 mTorr, the film transitioned from a-Si:H to nc-Si, as indicated by the emergence of a narrow peak at 521cm^{-1} . The intensity of the crystal signal increased as the deposition pressure decreased. Inset of the Fig 4-6 calculated crystalline volume fractions are illustrated. The maximum Raman crystallinity (X_C) was 49% for thin films prepared at 10 mTorr deposition pressure and it is decreasing with increasing deposition pressure values.

Fig 4-7 shows the XRD spectra of the same samples for which the RS spectra are shown in Fig 4-6. Although the RS spectra did not show any c-Si signal for films deposited at 35 mTorr, the

GI-XRD spectra showed a broad peak with a shoulder located around 28.4° , which indicated the onset of crystallization in the (111) direction. This pattern indicated nano-crystal formation in the (111) direction towards the film surface; however, the film structure was still mostly composed of the amorphous phase owing to its wide full width at half maximum (FWHM) value. As the deposition pressure decreased, other crystal orientations could be seen clearly. At 25 mTorr, the Si (111) peak became more intense and two additional peaks attributed to (220) and (311) crystal orientations of Si were observed at 46.26° and 55.79° , respectively. With a further decrease in the deposition pressure, the Si (400) and (331) crystal planes became slightly clear around 69° and 76° , respectively. The intensity of the Si (111) peak increased more than the intensities of any other peaks with decreasing deposition pressure. Hence, the GI-XRD spectrum indicated that preferential growth orientation of grains in the deposited films is towards the (111) crystal plane. According to Kakinuma et al., this preferential growth is explained by the lower surface energy of the (111) Si crystal orientation compared with the other crystal planes [44].

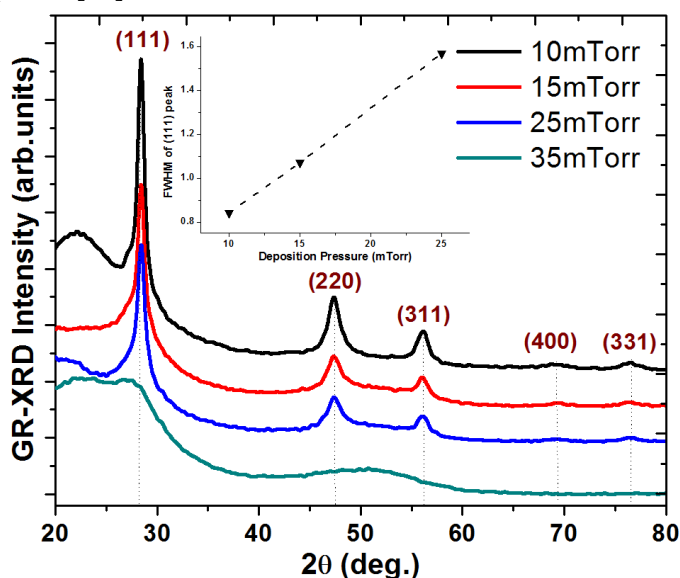


Fig 4-7 GI-XRD spectra of the Si thin films deposited at various deposition pressures

The grain size of films estimated from the FWHM and diffraction angle of Si (111) signal using the Debye-Scherrer formula (Eqn. 2-14). According to the XRD spectrum, the grain size increased as the deposition pressure decreased. It is not possible to calculate grain size for the sample deposited at 35 mTorr, since no clear peak is observed at (111) Si crystalline plane. Besides, crystal size for the sample deposited at 25 mTorr is equal to 7.6 nm while for 15 mTorr it is equal to 9.3 nm. With further increase grain size reaches 12 nm within the sample deposited at 10 mTorr. Additionally, the FWHM of the Si (111) crystal orientation related signal decreased with the plasma pressure, which indicates higher crystallinity at lower plasma pressures. Based on both the RS and XRD results, it is clear that low deposition pressures favor volume crystalline fraction with larger grain sizes.

The crystallization dynamics of an ICP process are quite different than the dynamics of the conventional CCP process, in which the quality of crystallization degrades at low deposition pressures due to the lack of sufficient atomic H. This phenomenon results in insufficient H

coverage of the film surface [105]. However, with ICP-CVD, the reactive H^* species and atomic hydrogen content in the plasma greatly increases due to excessive silane dissociation. The additional hydrogen may have a destructive etching effect on the Si network that provides disordered crystal lattices. Hence, over-abundant H-atoms cause degradation of the crystalline volume fraction [106].

4.2.3 Morphology

Surface topography and cross-sectional SEM images of nc-Si thin film deposited at 10mTorr (Fig 4-8 (a) and (b)) and a-Si thin film deposited at 35 mTorr pressure (Fig 4-8 (d) and (e)) are shown in Fig 4-8. It is clear from the cross-sectional images that both nc- and a-Si thin films shows a columnar fashion after the growth. However, columns are more bundled in amorphous structure while they are thinner and more separate in nanocrystalline phase structure.

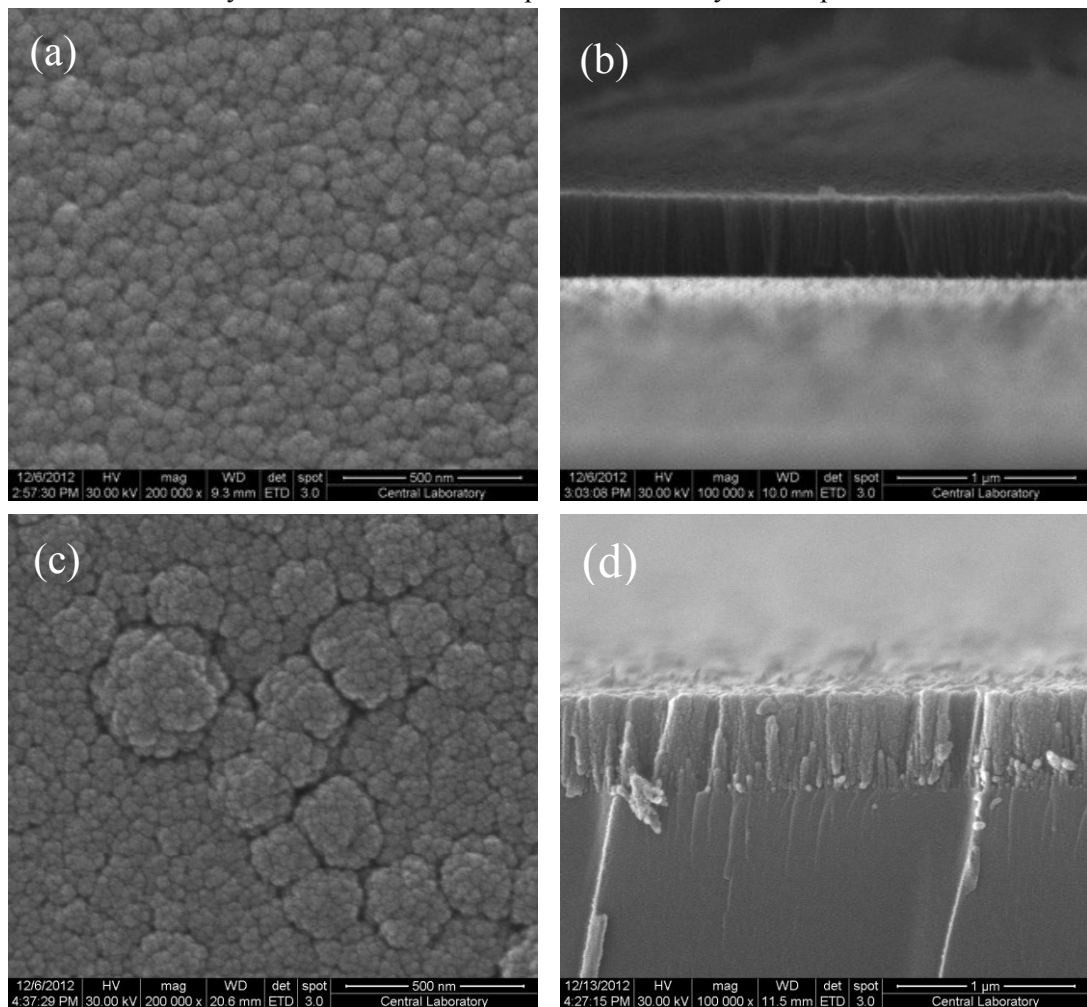


Fig 4-8 Surface topography (a) and Cross-sectional SEM images (b) of nc-Si thin film. Surface topography (c) and Cross-sectional SEM images (d) of a-Si thin film.

In previous studies, the columnar growth of ICP-CVD-deposited a- and nc-Si thin films has been explained by the domination of certain reactive plasma species, specifically SiH_x ($0 \leq x \leq 3$). It is well known that ICP-CVD systems can produce high-density plasmas, which

have a high dissociation capacity of SiH_4 and H_2 due to inelastic interactions of feed gases with electrons. Following the dissociation of silane, reactive species such as Si^* , SiH^* , SiH_2^* , SiH_3^* , and H_2 are formed. Generally, SiH_3 radicals are considered the main contributor to thin film growth because of their long lifetime and low reactivity [45, 107]. SiH_3 radicals have high surface diffusion; therefore, they generally find the most suitable energetic place before reacting with other species. On the contrary, any SiH_x ($0 \leq x \leq 2$) species arriving at an a-Si:H surface has sticking problem; they are highly reactive and have short lifetimes. These radicals can react immediately even at room temperature without finding the energetically most suitable sites. As a result, the dominance of SiH_x ($0 \leq x \leq 2$) species within the plasma under certain circumstances can result in a columnar microstructural formation owing to the limited lateral diffusion [108, 109], as it is observed in this study. Even so, this model is not sufficient to fully explain the observed columnar growth. In our paper, this columnar structure formation is explained via Ballistic deposition theory. According to this theory, particles that collide with the substrate via a straight vertical trajectory from a random position will stick to the substrate [110-112]. During the deposition, no external heat is applied to the substrate, which restricts the surface diffusion of the incoming subdivisions. Restricted lateral diffusion eventually forces the structure to grow vertically; hence the columnar growth is observed. Generally, there are two mathematical functions introduced to describe the ballistic deposition growth [111-114];

$$\bar{h}(t) = \frac{1}{L} \sum_{i=1}^L h(i, t) \quad (\text{Eqn. 4-1})$$

where \bar{h} is the mean height of the surface, L is the system size (the number of columns), $h(i, t)$ is the height of column i at time t .

$$w(L, t)^2 = \frac{1}{L} \sum_{i=1}^L [h(i, t) - \bar{h}(t)]^2 \quad (\text{Eqn. 4-2})$$

where $w(L, t)$ is the interface width that characterizes the roughness of the interface. This simple method provides control over the film morphology, porosity and directional growth. In short, columnar growth via the ballistic deposition process is independent of the material type; it is purely related to the deposition kinetics. Here, investigation of the surface morphologies of the deposited films showed that the structure closely resembles cauliflower. In a recent study on WO_3 , cauliflower-type growth has also been observed and successfully described by the ballistic deposition model [115]. The visible structural similarities between these quite different materials such as WO_3 [115], TO_2 [116], MgO [117] and a-Si/nc-Si are quite surprising.

In order to understand further the interior structure of these cauliflower-like structures, HRTEM imaging analyses are conducted. The structure was founded in a dendritic form with a excessive degree of porosity (Fig 4-9 (a)). The individual wire-like structures are bundled to each other during the fabrication until a critical radius is formed (Fig 4-9 (b)). When these bundles form next to each other, they begin forming these interesting cauliflower-like

structures on the surface of deposited thin films.

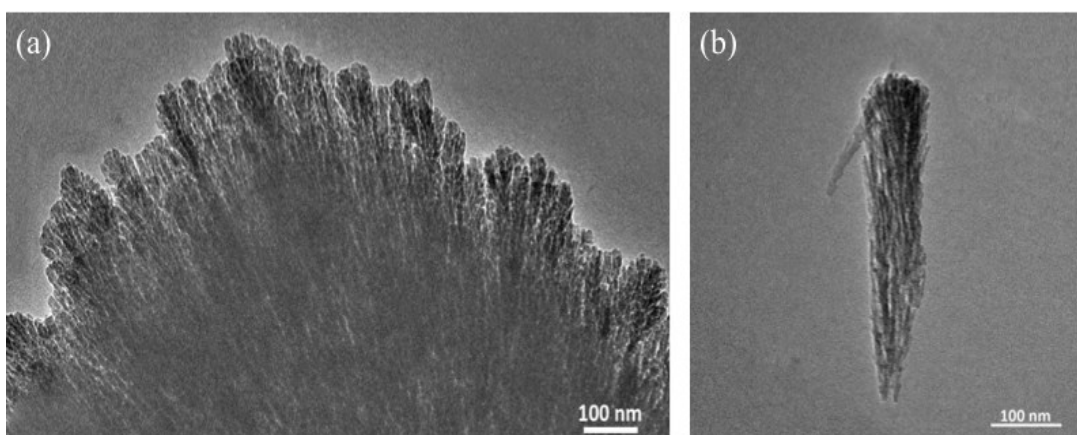


Fig 4-9 HRTEM images of Si:H cauliflower-like structure (a) and an individual Si:H bundle (b).

According to the ballistic deposition process, lateral migration of the species is limited, however a small number of atoms / clusters are moved to the next unoccupied site on the surface instead of assembling on top of an already occupied site. This leads to an angular lateral extension of the bundles, which can be described as fan-like structures basically, as a result of this extension the formation of dendritic structures is observed. This formation makes a large contribution to the porosity, which is assumed as the main reason for the aging effect that will be discussed in the following section. Recently, theoretical studies performed by Robledo et al. [113] and Saito et al. [111] have explained the formation of these fan-like structures extensively by modeling the dynamics of angular expansion during columnar growth using ballistic deposition theory; these studies are consistent with the results obtained in this work. Although these structures and non-uniformity may be considered as a main reason for poor film quality, the columnar structures provide effective channels for vertical carrier transport for the solar cell applications [118].

4.2.4 Aging Effect

FTIR measurements were conducted to determine the Si-H vibration modes and calculate the hydrogen content of the films. The FTIR absorption spectra of Si thin films deposited with different deposition pressures in the range of 550-2200 cm^{-1} is shown in Fig 4-10. Thin vertical dotted lines specify the position of the Si vibration modes. Absorption at 630 cm^{-1} was attributed to the Si-H rocking/wagging mode, the signal at 870 cm^{-1} was attributed to the Si-H₂ bending modes, the remaining peak at ~2000-2030 cm^{-1} was ascribed to the Si-H_x ($1 \leq x \leq 3$) stretching modes and the Si-O-Si bridging mode at 1070-1080 cm^{-1} . The position of the wagging mode shifted slightly to higher frequencies with decreasing deposition pressure, as observed in the inset of Fig 4-10. This shift has been reported to result from the rigid Si-Si bonds and increased crystallization at lower deposition pressures [119, 120], which is consistent with the RS and GI-XRD results presented in section 4.2.2. It is also observed that Si-O-Si bridging mode related peak increases with crystallization enhancement. This can be related with the micro-voids created during the micro/nano-crystals growth.

It is possible to calculate the bonded hydrogen concentrations of deposited films using signal intensities in the IR absorption spectrum. Since hydrogen content affects all optical and electrical properties of the films, it is very crucial to calculate the hydrogen content from the IR absorbance band. A commonly accepted method to determine the hydrogen concentration of films using the IR spectra is thoroughly explained in the studies of Mahan et al. and Kroll et al. [121, 122].

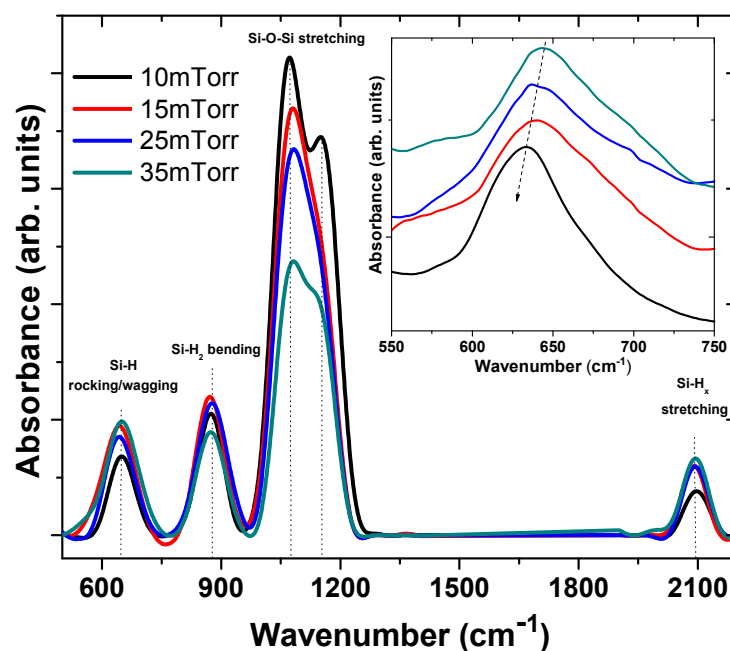


Fig 4-10 FTIR spectra of the samples deposited with various deposition pressures. Shifting of Si-H rocking/wagging mode with respect to deposition pressure (inset).

The hydrogen content of the film was less than 6.8% for all ICP-CVD deposited films with different pressure. Low hydrogen content is a well-known feature of ICP-CVD-deposited thin films. In Table 4-2 hydrogen content for the Si- thin films deposited with various pressure is shown. For the Si-thin film deposited at 35 mTorr, hydrogen content (C_H) value is equal to 3.5%. Qin et al. [123] also reported a low C_H level of 3.8%; they suggested that the enhancement of hydrogen desorption may be responsible for the reduced hydrogen content. C_H is equal to 3.7 % for the sample deposited with 25 mTorr pressure. With decreasing the pressure to 15 mTorr, C_H upsurges to 6.3% and with further decreases C_H reaches 6.8%. It is the well-know fact that hydrogen content is very important factor for Si layers quality. According to the literature, the best quality a-Si:H thin films deposited with plasma assisted techniques should have bonded hydrogen concentrations less than 10% [4]. It should be pointed out that the calculated hydrogen content via FTIR spectrum is generally less than the exact hydrogen content of the film, since in the calculation only Si-H rocking/wagging mode related peak is taken account.

Table 4-2 Hydrogen concentration changes with deposition pressure

Deposition Pressure (mTorr)	Hydrogen Content (%)
10	6.8
15	6.3
25	3.7
35	3.5

The most interesting feature of the FTIR spectra was the presence of a strong Si-O-Si bridging mode signal between 1000 cm^{-1} and 1200 cm^{-1} . To determine the origin of this stable oxide inside a film, we performed an aging experiment with recording the intensity of the oxidation concentration percentage as a function of time in a series of measurements. As it can be seen Fig 4-11, no oxygen contamination was observed immediately after the deposition. However, the film oxidized drastically over time. The integrated area of the Si-O-Si bridging mode signal is displayed as a function of time in the inset of Fig 4-10. We can see that the oxidation continues quite effectively even after 1 month. After 1 month, oxidation become more stable since the films structure was saturated.

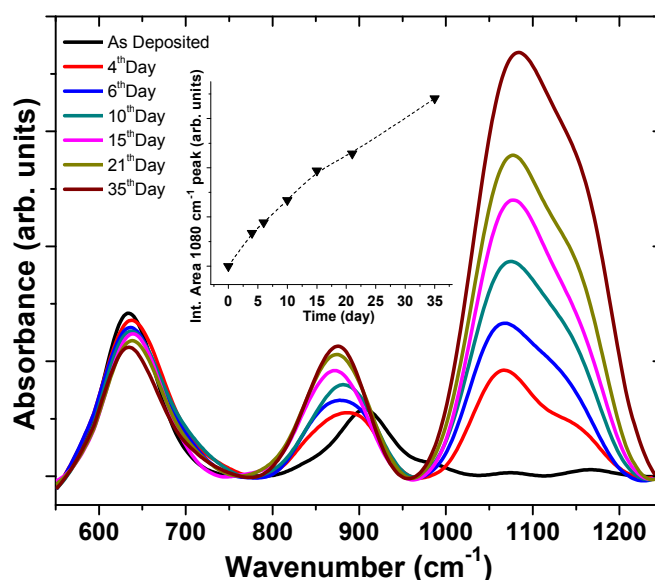


Fig 4-11 Variation of FTIR spectra with time (inset) integrated area change of Si-O-Si stretching mode signal

X-Ray Photoelectron Spectroscopy (XPS) depth profile analysis is performed for determination of the Si and O distribution through the film structure. Fig 4-12 shows XPS depth profiling spectrum for the sample deposited with 10 mTorr pressure, which has the highest crystalline volume fraction according to the RS (Fig 4-6 (inset)). The binding energy corresponding to the Si 2p and O 1s peak are measured. The calibration of the binding energies is performed using the peak at 532.7 eV attributed to the O 1s [124]. Peak observed at binding energy 98.2 eV is attributed to Si-binding energy in bulk-Si and 103.4 eV is attributed to the silicon - dioxide (SiO_2) [125]. According to the depth profiling near the surface of the film, SiO_2 and O 1s peaks become very clear. Fig 4-12 (a) shows that the uniform distribution of the

O 1s through the film and Fig 4-12 (b) shows the SiO₂ increases on the film surface and film-substrate interface.

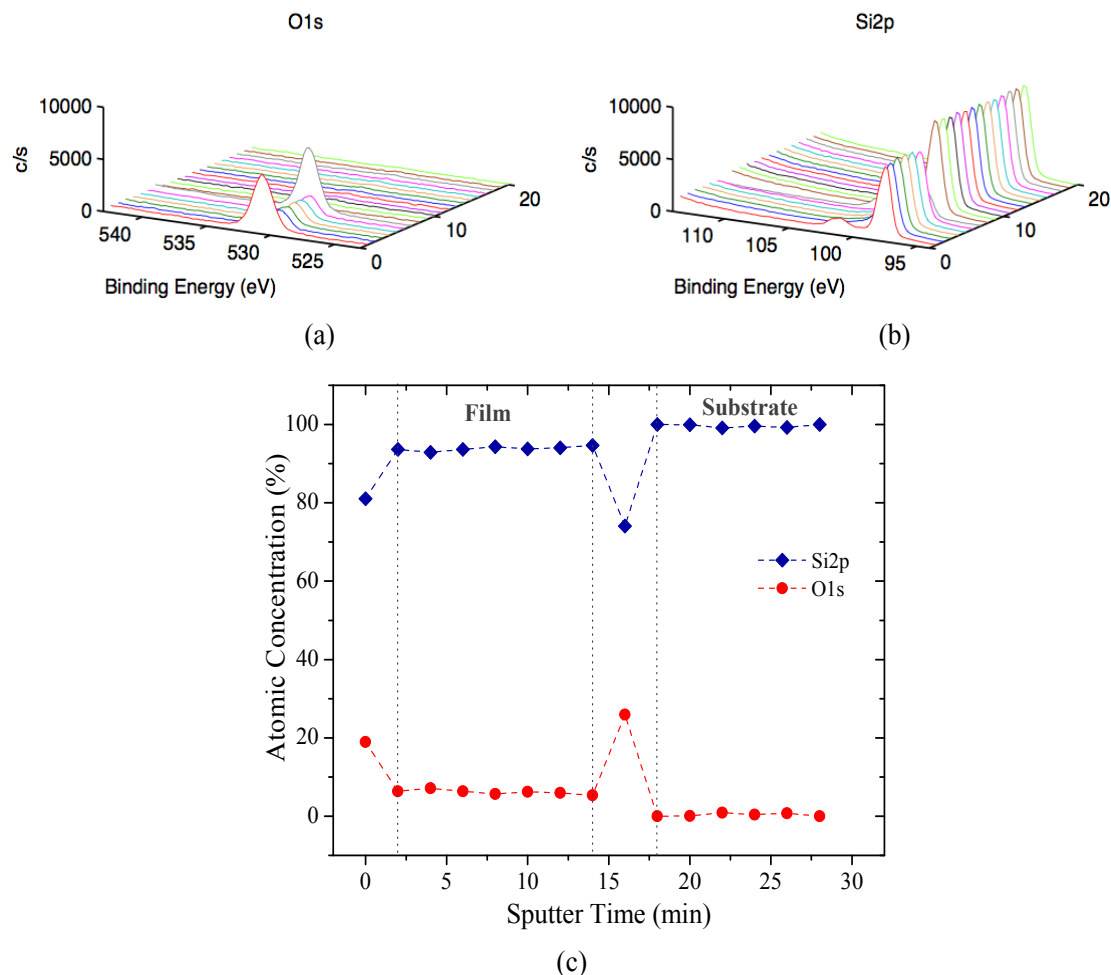


Fig 4-12 XPS depth-profiling spectrum of the film deposited with 10mTorr pressure at room temperature: O 1s core level (a), Si 2p core level (b) and atomic concentration percentage of O and Si extracted from XPS depth-profiling analyses(c).

Variation of the Si 2p and O 1s signals as a function of position from the film surface to substrate is displayed in Fig 4-12 (c). According to the atomic concentration of oxygen of the film was quite uniform through the film, indicating that the sample was uniformly oxidized. The uniform oxidation might be related to the high porosity associated with the cauliflower-like structures that allows easy oxidation paths even at room temperature.

Consequently in this part of the thesis, the structural properties of the samples deposited by ICP-CVD in different phases are investigated with changing the process powers and pressures. It is revealed that crystalline volume fraction and deposition rates are strongly related with the inductively coupled plasma pressure and power. With increasing power crystalline volume fraction and grain size upsurges while same trend is obtained by decreasing deposition pressure. It should also be pointed out that owing to the room temperature process, maximum

grain size observed in highly crystallized sample is equal to approximately 10-12 nm. Peculiar structures resembling cauliflower and columnar growth fashion are also observed in both a-Si and nc-Si thin films and those structures explained with two different approaches: one relates to the generated plasma species after the dissociation of silane and the other one is based on the well-known ballistic deposition theory. FTIR aging experiments indicated that the ICP-CVD-deposited Si structure is oxidized gradually and extremely uniformly throughout the film when exposed to air due to its highly porous nature. The columnar structure may provide vertical carrier transport channels that can increase the vertical electrical conductivity of Si thin films.

CHAPTER 5

OPTO-ELECTRONIC PROPERTIES OF Si THIN FILMS PREPARED BY ICP-CVD TECHNIQUE

In previous chapter, structural features of the silicon thin films fabricated via inductively coupled plasma enhanced chemical vapor deposition technique were examined with different aspects. Various analyses showed that these samples grown in columnar fashion with highly porous and dendritic nature. During the optical characterization of the ICP-CVD samples, it is observed that they also show tunable light emission at room temperature. In 1990s, a large number of scientists has been directed their attention towards the fundamental features of porous Si due to its highly efficient visible light emission property even at room temperature [75, 126]. Light emitted silicon is commonly considered as a remarkable material that can expand the functionality of well – recognized Si technology from micro-electronics to opto-electronic [127, 128]. Thus, photoluminescence feature of ICP-CVD deposited films was explained with the light emission mechanism of the porous Si and small Si nano-crystal formation within the large band-gap matrix. Detailed examination about Si nano-crystal formation was performed with HRTEM image analyses. In order to find the correlation in between crystallinity and band-gap expansion, optical band gap values were calculated using UV-visible spectrometer and well-known Tauc-plot method. Another important aim of the band-gap analyses was to tune the band-gap with Si nano-crystals, which enables the fabrication and optimization of tandem silicon solar cell structures. In addition to these analyses, current-voltage measurements and conductivity calculations are performed to understand the availability of ICP-CVD deposited samples for the photovoltaic device applications.

In this chapter, optoelectronic properties of the same set of samples, which were studied in Chapter 4, and effects of the porous nature of the film in optical features were investigated. Additionally, hydrogen dilution effects on the structural and optical properties of the deposited films were investigated with two samples fabricated at room temperature with same deposition parameters except hydrogen dilution.

5.1 Photoluminescence Properties

The optical behaviors of films were examined by steady-state photoluminescence (PL) measurement at room temperature in their as grown states with using Nd-YAG 532 nm continuous laser as an excitation source. Pavesi et al.[36, 38] reported that when the Si-nanocrystals surrounded by larger band gap matrix, such as SiO₂, SiO_x, a-Si or air, two-dimensional potential well structure with extra-localized energy states has been expected. If the photons transmitted to the sample surface has the energy larger than the quantized energy, two kind of optical relaxation are expected. Fig 5-1 describes schematically the additional energy states levels involved in excitation and luminescence. There was a group of excited

states near the Si conduction band edge that participated in the luminescence process, contributing to the inhomogeneous broadened PL spectrum. Typical porous silicon and silicon rich oxide (SRO) emit light at room temperature in a broad red/infrared range of 600 ~ 1100 nm [129]. Quantum confinement by the nanostructures and the highly - localized interface defects residing at their boundaries are the dominant source of photoluminescence in nanostructured and porous silicon. In Fig 5-1, PL1 illustrates the emission related with the quantum confinement effect while PL2 shows emission from the localized interface energy states [130].

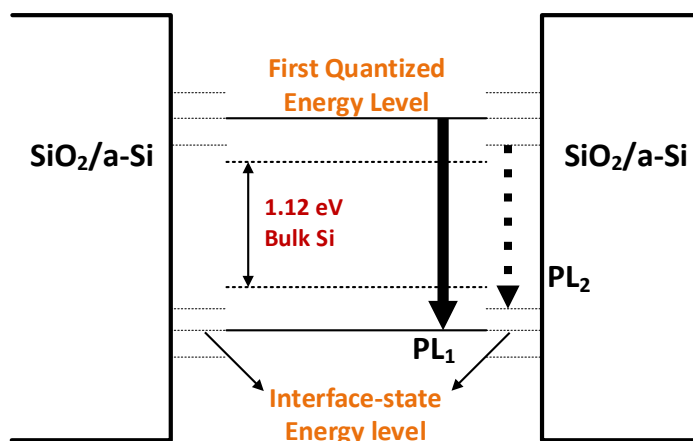


Fig 5-1 Schematic energy level diagram and competing PL mechanisms for Si nanocrystals surrounded by large band gap material

To explore this issue further generally PL spectra were deconvoluted into three Gaussian components as defined in Table 5-1: Peak-I (750 – 800 nm), Peak-II (850 – 950 nm) and Peak-III (1000–1150 nm)[131]. Previous studies attributed these components to the quantum confinement associated with the Si nanocrystals [132] and the surface states residing at their boundaries. Component I (750 – 800 nm) is attributed to transitions from the lowest occupied level in the conduction band tail states to the highest vacant level in the valence band tail states. The other two peaks are attributed to the transition from defect levels associated with the nanostructure boundaries to the valence band and localized states in a-Si cluster [133], respectively.

Table 5-1 Positions and origins of the deconvoluted Gaussian components of PL spectra[131]

Peak-I	700-800 nm	Quantum confinement
Peak-II	850-1000 nm	Interface state
Peak-III	1000-1150 nm	Localized states of a-Si clusters

Deconvolution of the PL spectra produces the opportunity to control and observe origin of the emission. Afterwards, effects of deposition parameters; pressure and hydrogen dilution, on luminescence feature was investigated.

5.1.1 Pressure Effect

As it was proved in previous chapter after exposure to air, columnar porous-like structure absorbs oxygen from the ambient and produces interface states in between silicon nanocrystals and air or SiO_x matrix. Fig 5-2 presents the PL spectra of the samples deposited at various pressures. For the sample deposited at 50-mTorr, which is totally in amorphous phase according to the RS and GI-XRD spectra (see Chapter 4), gives no PL signal and behaves like a glass substrate. However, PL signal increases significantly with decreasing pressure, which is strongly correlated with the confinement by the crystalline phase. As shown in Fig 5-2, our sample deposited at 35-mTorr shows quite broad PL signal that includes all three Gaussian components unambiguously. Especially, the peak-I located at 750 nm become very prominent for the film deposited at 35-mTorr. As the pressure decreases and peak-II become more dominant in the PL spectra due to the enhancement of the interface states. With decreasing pressure, the crystalline volume fraction increases but, as shown above by HRTEM and by XRD calculations, the size of the resulting nanostructure increases. This results in a larger total surface area at low pressures, strongly suggesting that not only quantum confinement but also surface states at their boundaries are also involved.

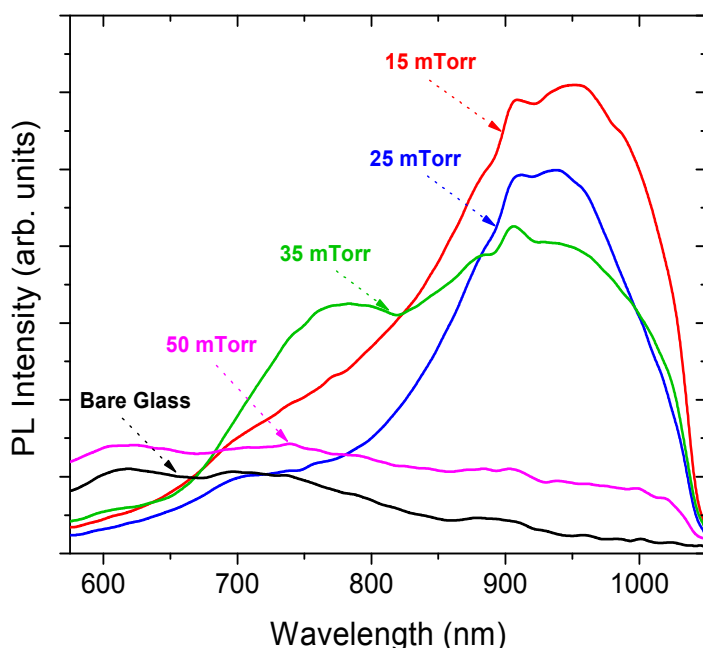


Fig 5-2 PL Spectra of the samples fabricated at various deposition pressures

The changes in the positions of the deconvolution components were shown in Fig 5-3 for the various pressures used. It can be obviously seen from the Fig 5-3 that a negligible shift in position is observed for Peaks II and III for all three samples. However peak-I, which is related with the quantum confinement effect, illustrates significantly appreciable red shift of the position with decreasing pressure.

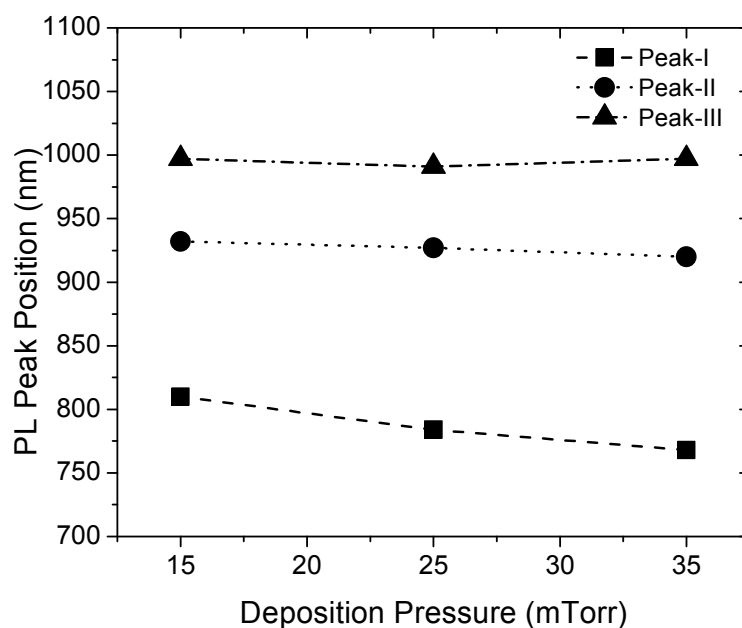


Fig 5-3 Positions of the deconvoluted three Gaussian components for three different pressures

To demonstrate this shift more clearly, we normalize the values of peak I for all pressures and plot them together in Fig 5-4. The position of peak-I, is clearly red-shifted with decreasing pressure. This shift is considered as an indication of the larger nanoparticles sizes according to the quantum confinement model. Size calculations from Debye-Scherrer formula using GI-XRD spectra (Chapter 4) showed that the nanocrystalline size also increases with decreasing pressure, which is consistent with the PL results and a natural consequence of quantum confinement as predicted by the quantum confinement model.

Crystal size for the sample deposited at 15-mTorr is equal to 7.6 nm according to the XRD spectrum and deconvoluted peak-I position is 810 nm. Calculated grain size becomes 5.2 nm with the decreases in the deposition pressure up to 25mTorr and position of the peak-I shifts to 784 nm. With further increasing of the pressure, unfortunately it is not possible to calculate grain size with using GI-XRD spectrum. As it is mentioned in previous chapter, for the sample fabricated at 35-mTorr only small and broad shoulder is observed at 111 crystal silicon orientation (Fig 4-7) which indicates the onset of the crystallization, however it is not possible to use that peak for Debye-Scherrer size calculation. Even if we could not calculate the sizes, it is obvious that there are small Si crystals embedded into amorphous Si matrix. Deconvoluted peak-I position for the same sample is 760 nm.

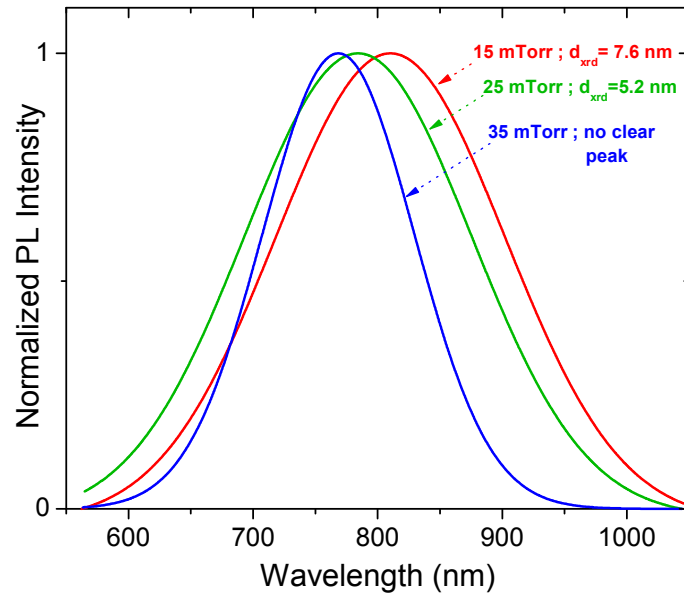


Fig 5-4 The shift in position of peak-I of the PL spectra normalized to unity for the films deposited room temperature and at different pressures as indicated.

With decreasing pressure, calculated XRD crystal size increases and crystalline volume fraction enhancement is observed. Red shift of the PL spectra also confirms this result due to the quantum confinement model. Another important analyses that can be confirmed the obtained consequence is the HRTEM images of the deposited samples.

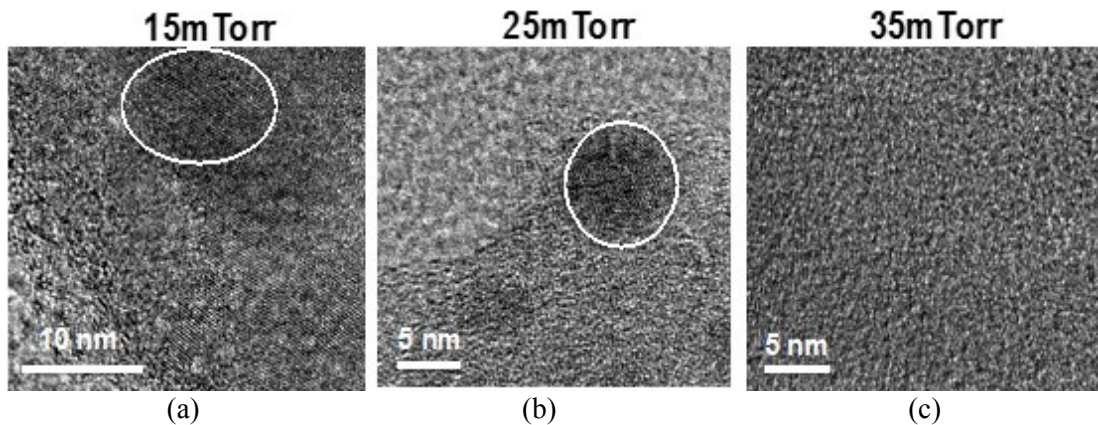


Fig 5-5 HRTEM images of three films deposited at room temperature and: 15-mTorr (a) 25-mTorr (b) and 35-mTorr (c)

HRTEM analysis has been used to verify the most detailed evidence about the internal structure of the material. Fig 5-5 shows the HRTEM images of the samples deposited at various pressures. It can be clearly seen that the grain sizes are decreasing with increasing pressure, which is highly correlated with the results obtained from PL and XRD spectra measurements. White circles were drawn just as a visual guide.

5.1.2 Hydrogen Dilution Effect

The effect of hydrogen dilution was also investigated by producing two samples with different hydrogen dilution, all other parameters such as SiH_4 flow (9sccm), pressure (25mTorr), power, etc. were kept constant. As it is mentioned before hydrogen dilution is defined as the ratio of the hydrogen flow to the total flow. In Fig 5-6 (a), we show the PL spectra for two samples obtained at low pressure (25mTorr) with large nc-Si fractions where significant enhancement is observed for the film with higher hydrogen dilution. However further analysis of these data reveals no shift in the position of any peak. Therefore, hydrogen flow effects the radiative emission of interfacial state significantly.

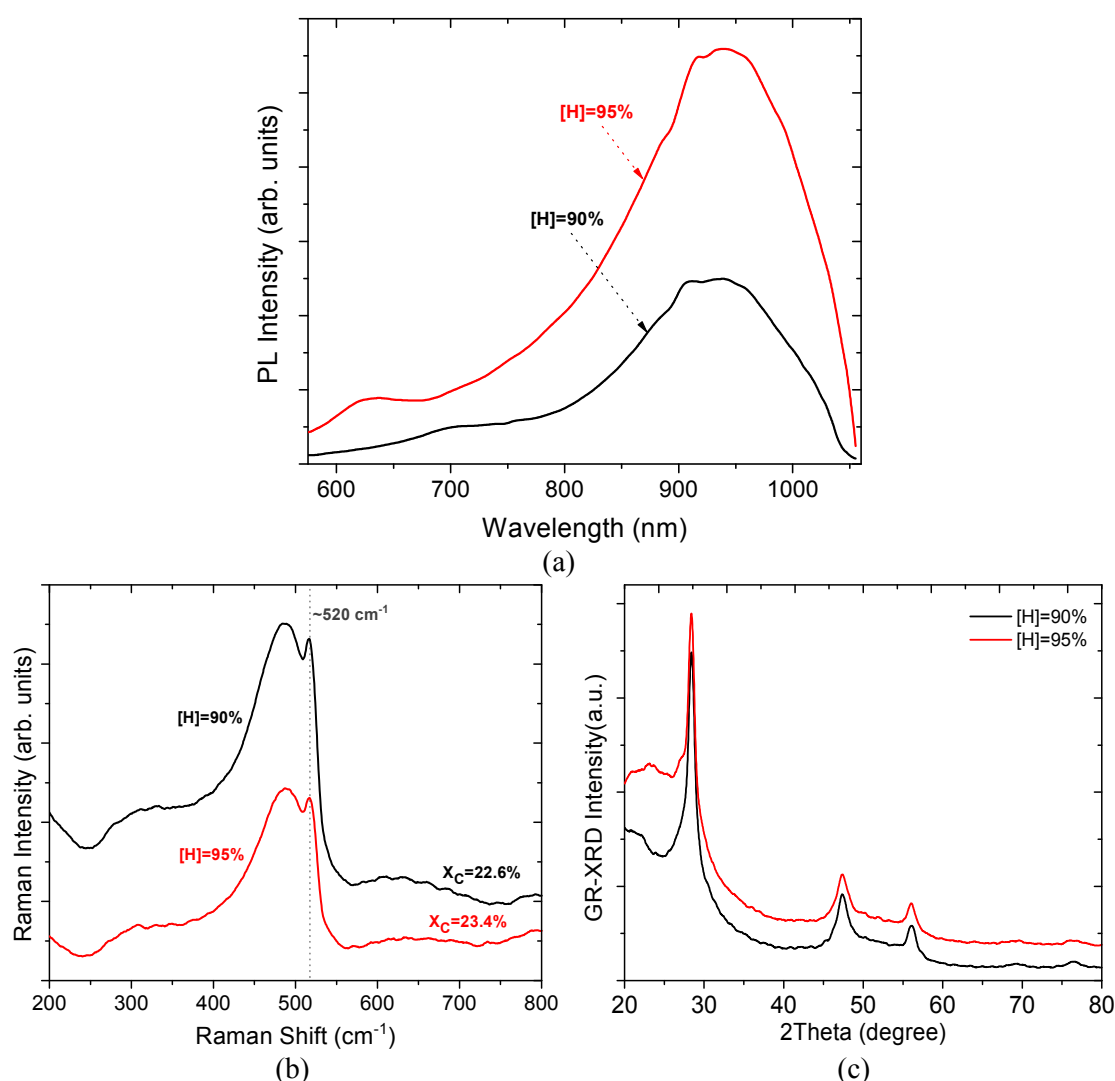


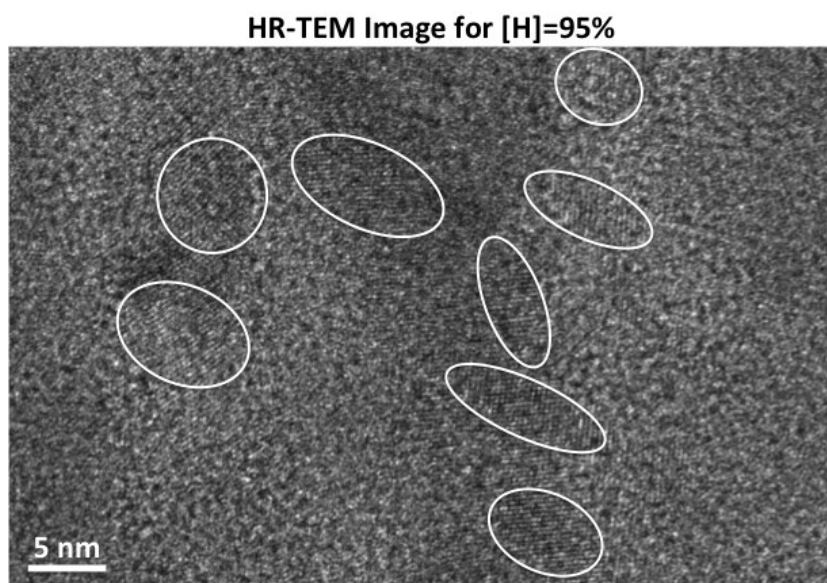
Fig 5-6 The PL (a), RS (b) and GI-XRD (c) spectra for two films deposited at room temperature, 25 mTorr and different hydrogen dilution as indicated.

In order to understand the origin of the 5-fold enhancement in PL signal, additional analyses are performed. Raman spectra of the samples (Fig 5-6 (b)) show that 5% change in hydrogen dilution has no significant effect on crystalline volume fractions since it is equal to 22.6% for the sample deposited with 90% hydrogen dilution and 23.4% for 95% hydrogen dilution. Fig

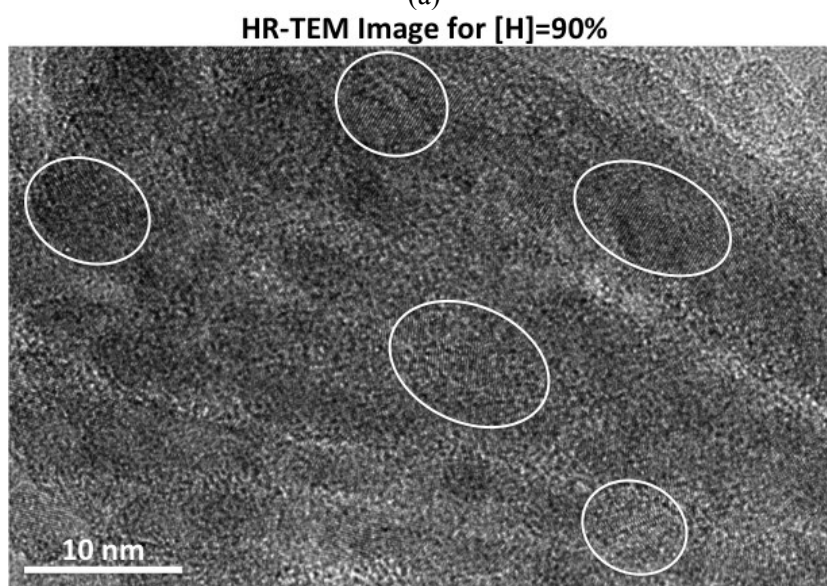
5-6 (c) shows the GI-XRD spectra of the same samples. It is obvious that crystallinity of the samples are very close to each other, however grain size calculation using Debye-Scherrer formula shows that sample deposited with higher hydrogen dilution has smaller nanocrystals (Table 5-2). Smaller nanocrystals with same crystalline volume fraction means larger number of nanocrystals, thus more interface states in between nanocrystals and larger band gap matrix.

Table 5-2 Summary of XRD data for the Si thin films deposited with different hydrogen dilution

[H]	2 θ	FWHM	d (nm)
90%	28.42	1.57	5.2
95%	28.73	2.97	2.7



(a)



(b)

Fig 5-7 HRTEM images for the samples deposited with 95% (a) and 90% (b) hydrogen dilution.

Fig 5-7 (a) and (b) show the HRTEM images for the samples deposited with different hydrogen dilution. White circles were drawn just as a visual guide. It is obvious that grain sizes are larger for the sample with 90% hydrogen dilution. It is also well-known fact that increasing hydrogen flow leads to the reduction of the grain sizes. Hence, HRTEM image analyses give the correlated results with the PL and GI-XRD spectra. Smaller and denser nanocrystals created more interface states and enhanced the light emission.

5.2 Band Gap Estimation

UV-visible spectrometer is used to determine transmission characteristics of the sample deposited with different pressures. Optical transmittance measurements were also used for extract information about the optical band gap (E_g) of the materials using Tauc's equation [134-136]:

$$\sqrt{\alpha h\nu} = B(h\nu - E_g) \quad \text{Eqn. 5-1}$$

In this method, $(\alpha h\nu)^{1/2}$ is plotted against $h\nu$, the linear portion of the curve is extrapolated and its intercept with the energy axis is taken to represent the optical band gap basically [137]. In this plot, $h\nu$ is incident photon energy, B is the edge width parameter related to the width of band tails and density of states in the film and α is the absorption coefficient which can be calculated from: $I_T = I_0 e^{-\alpha d}$, where I_T/I_0 is equal to transmission T and d is the thickness of the deposited nc-Si films. In Fig 5-8, the optical band gap, as obtained by the Tauc's plot decreases appreciably and linearly with increasing pressure. This result is an important signature of nanostructure formation in amorphous systems and can actually be taken to indicate nanostructure formation.

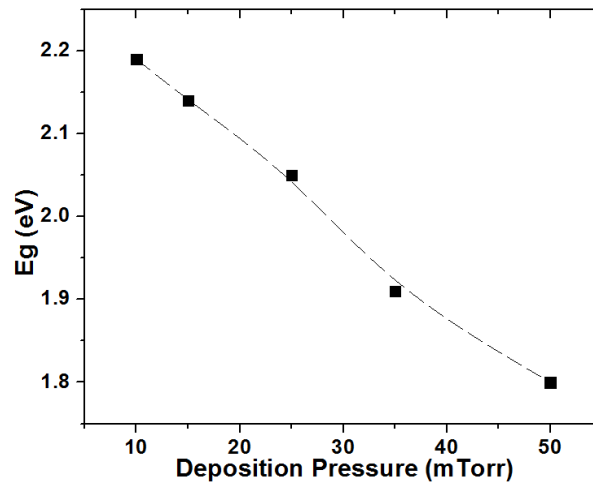


Fig 5-8 The optical band gap as determined from the Tauc's plot versus deposition pressure.

A non-monotonic change observed in the Tauc's band gap with pressure could not be explained in terms of the crystalline volume fraction because it increases monotonically with decreasing pressure. Instead, we try to correlate the change in band gap with hydrogen content. In the present work, the linear decrease in the optical band gap with pressure is consistent with the decreasing hydrogen content (Chapter 4) as well as the increase in crystallinity. This result

is also consistent with the clear shift in peak-I of photoluminescence obtained for these films as shown in Fig 5-4. The higher than typical values of the band gap in our films may be explained in terms of the larger oxygen adsorption upon exposure to atmosphere as demonstrated by the FTIR results in previous chapter. It is also good to note that some scientists claim that higher than normal band gap values are due to an inherent over-estimation of the band gap associated by the Tauc's method. In 1991, Gosele and Lehmann [138] reported that porous Si structures could display a band gap enhancement compared with bulk-Si. They also claimed that this property and formation mechanism involve quantum size effect which can be also the reason of increase in band gap.

5.3 Electrical Characterization

Film conductivity is the one of the most important property that identifies the materials. Dark conductivity (σ_{dark}) and photoconductivity (σ_{photo}) of the films deposited at room temperature with different deposition pressure were measured in two co-planar electrode method described in Chapter 2. The measurement is performed in ambient atmosphere at room temperature. Conductivity change with various deposition parameters such as pressure and hydrogen dilution were examined in this part of the study.

5.3.1 Pressure Effect

Fig 5-9 (a) and (b) show the current voltage characteristics of the samples deposited at 15-mTorr and 25-mTorr, respectively. For the determination of the photo response of the films halogen lamp is used as an illumination source. It is obvious that photo responses are quite low, however it is reasonable since all samples are deposited at room temperature.

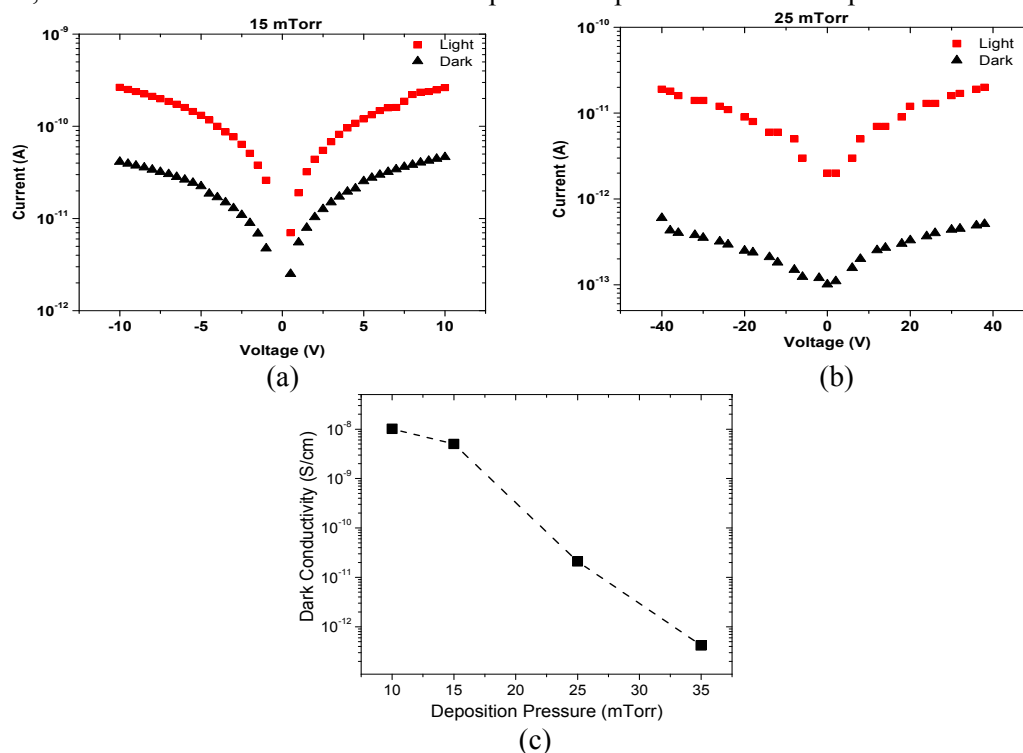


Fig 5-9 Measured Current-Voltage spectra of the samples deposited at 15mTorr (a) and 25mTorr (b). Variation of dark conductivity with deposition pressure (c).

Fig 5-9 (c) illustrates the dark conductivity variations of the films deposited with different pressures at room temperature. It can be clearly seen from the figure that dark conductivity increases with decreasing deposition pressures; this result can be explained with the enhancement of the crystalline volume fractions. Highly crystallized samples have more ordered structure, which enables the more effective carrier transport within the film.

5.3.2 Hydrogen Dilution Effect

Hydrogen dilution is commonly controlled in order to improve layer quality. It is also very essential for the phase transition from amorphous to micro/nano-crystalline due to its passivation effect of the dangling bonds. It is a well-known fact that when a-Si layer deposited only with silane, defect density of the layer would be quite high (10^{19} defects/cm³ instead of 10^{16} defects/cm³ or less)[4].

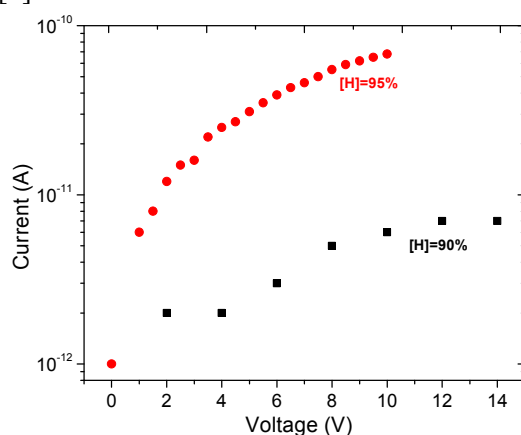


Fig 5-10 Measured current-voltage spectra of the samples deposited with different hydrogen dilution at room temperature in the dark ambient.

As it is mentioned before 5% change in hydrogen dilution has no significant effect on crystalline volume fraction, however it causes 5-folds enhancement in PL spectrum. Dark current-voltage characteristic of the same samples (Fig 5-10) show that the sample deposited with more hydrogen-diluted gas has higher conductivity, which is correlated with the PL measurements. Additional hydrogen passivates the defects and decrease trap states within the band gap, thus more carriers join the emission instead of trapping defects states. Current voltage characteristic also supports that hydrogen dilution increases the film conductivity. Dark conductivity of the film deposited at 25mTorr with 90% hydrogen dilution is equal to 6.38×10^{-10} S/cm while for the sample deposited at same parameters but with 95% hydrogen dilution, it is equal to 8.97×10^{-9} S/cm. Photo-response of the layers are quite low ($\sigma_{\text{photo}} / \sigma_{\text{dark}} \sim 30$), however it is expected due to the low fabrication temperature.

As a conclusion, opto-electronic properties of the Si thin films deposited via ICP-CVD technique were studied with different aspects using PL, HRTEM and current-voltage spectra. It is observed that luminescence of the samples can be tuned with deposition parameters easily. HRTEM images provide detailed information about nano crystalline formation within the film matrix and approximate values of grain sizes. Conductivity measurements revealed that film

conductivity is highly related with the crystalline volume fractions and enhance with increasing crystallinity.

CHAPTER 6

CONCLUSIONS AND FUTURE STUDIES

In this thesis, phase transition from amorphous Si to micro/nano-crystal Si has been investigated for the possible photovoltaic applications. Si thin film fabrication methods are commonly divided into two groups; chemical vapor deposition and physical vapor deposition techniques. During the study both techniques have been used for Si layer fabrication for comparison purposes. Deposited thin films have been characterized with different diagnostics tools. Basically, Raman Spectroscopy, Grazing Incidence XRD, FTIR, Spectroscopic Ellipsometry, Photoluminescence, SEM and HRTEM image analyses have been employed in order to obtain detailed information about film characteristics. In addition to these diagnostic tools, some conductivity measurements have been also performed using co-planar electrode method. In Chapter 2, basic physics behind the deposition techniques and working principles of the characterization tools used in this study have been explained very briefly. Especially, references used in this chapter can be considered as extremely valuable sources of information. In Chapter 3, crystallization properties of Si-thin films prepared by different deposition techniques have been examined. In this part, three different fabrication methods have been used for Si-thin film production; magnetron sputtering (PVD), electron beam evaporation (PVD) and plasma enhanced chemical vapor deposition (CVD) system with capacitively coupled plasma configuration. In Chapter 4, plasma enhanced chemical vapor deposition system with inductively couple plasma sources has been used for Si thin film fabrication. Interesting results obtained from this part force us to make more analyses in order to understand the structural properties of the samples. In Chapter 5, opto-electronic features of the same set of samples have been investigated. Below, general conclusion of this thesis has been summarized.

The most commonly used fabrication CVD system for the Si thin films is the PECVD system with CCP configuration. First set of samples were produced with this technique and good-quality a-Si:H layers were obtained using H₂ diluted SiH₄ as a source gas. It has been observed that deposition pressure is very important parameter that can change the film structure from amorphous to crystalline phase at room temperature depositions. With increasing pressure, it is possible to obtain approximately 60% crystallized Si thin films. However, when the substrate temperature increases, deposition pressure become more and more ineffective. Another important parameter that affects the film structure is silane concentration. In same part, four samples were deposited with different silane concentration at 200°C and with increasing silane concentration; deterioration of the crystals has been observed. Further investigations have revealed that conductivity of the films improve with the reduction of the silane concentration, however photo response of the films decreases with crystallinity. Hence, photo response of the a-Si:H layer is larger that the crystallized Si films, this result has been explained with an increase of the microstructure factor which is related with the micro-void concentration.

Second set of samples was fabricated by another popular method electron beam evaporation. This method is the one of the most simple and inexpensive PVD method and generally used for poly-Si fabrication. In order to obtain crystallized samples, solid phase crystallization process was applied in rapid thermal annealing chamber. In this system, it is possible to control deposition rate by changing applied current to the filament, which provides energetic electron for evaporation. We observed that, deposition rate has significant effect on the film structure. Four samples with approximately same thicknesses were fabricated with different deposition rate and it has been observed that sample deposited with the lowest rate is crystallized faster than the other three. Another important observation is that a-Si films fabricated by e-beam technique show quite narrow band gap according to the SE measurements and after H₂ treatment band gap value enhances approximately 0.2 eV. Additionally, two different samples were fabricated with same deposition rate but different thickness. Thicker films crystallized more effectively. Crystalline volume fraction of the sample changes from 10% to 58% with 250 nm thickening.

The nanocrystalline formation in SiO_x matrix has been investigated by carrying out various characterization methods. SRO films were deposited via magnetron sputtering technique. After the fabrication, films were annealed at 1100°C in high temperature quartz furnace. The most significant part of this study was the modeling of the spectroscopic ellipsometry results. Since modeling of the SE data provides the opportunity of obtaining information about films crystallinity and analyzing subspecies within the SRO films. Presented generic model has been also confirmed with the HRTEM images. It has been observed that when the excess Si amount is quite high, SiO₂ interface layer in between substrate and film layer can be seen very clearly.

PECVD system with ICP configuration has been also used during the study in order to increase deposition rate for nano/micro-crystal Si thin film production. ICP is the high-density plasma source, which has high dissociation capacity, this property provides high deposition rate and low temperature crystallization. Induced plasma diagnostics were analyzed with OES and high silane dissociation has been observed. With increasing deposition power, reactive species, which can be detected with OES increases and higher deposition rates have been obtained. Three different samples were deposited with different power at room temperature and we observed that high deposition power favors the crystalline volume fraction. Deposition pressure is also another significant parameter that affects the structure at room temperature deposition. It is possible to control crystalline volume fraction from 0% to 49% just by changing pressure. With decreasing pressure, more crystallized films have been obtained. The most interesting result from this investigation might be the columnar and porous nature of the ICP-CVD deposited films. Cross-sectional SEM images have revealed that films grown in columnar fashion for both amorphous and micro/nano crystalline phases. This columnar growth has been explained with two different theories; first one is related with the dominance of some plasma species and second one is the well-known ballistic deposition theory. Interestingly, highly intense and broad Si-O-Si stretching mode has been observed in FTIR spectra for all ICP-CVD deposited samples. With further investigation, it has been shown that there is no oxygen within the film immediately after the deposition, however films are oxidized

drastically with time. XPS depth profiling analyses have represented the uniform oxidation throughout the approximately 500 nm thick films. This uniform oxidation and HRTEM images indicate the porous and dendritic nature of the films, which allow easy oxidation path.

Optoelectronic properties of the same set of ICP-CVD deposited samples have been also explored. It has been observed that samples emit light at room temperature after excitation with 532 nm Nd-YAG continuous laser. This emission mechanism has been explained with the same photoluminescence mechanism of well-known porous Si material. We also observed from HRTEM images that nanocrystals sizes were not larger than 10 nm even if crystalline volume fraction values reaches 60%. Thus, quantum confinement effect has also been observed. Blue shift in the PL spectra has been explained with the increases in Si nanocrystal sizes. Changing hydrogen dilution from 90% to 95% causes no change in crystalline volume fraction, however 5-fold enhancement has been observed in light emission due to the hydrogen passivation effect. Dark conductivity of the sample deposited with higher hydrogen dilution is also higher than the other sample. Since more dangling bonds are passivated with hydrogen and more ordered structure is obtained with increasing hydrogen dilution.

Further studies can be performed about some of the subjects that have been mentioned in this thesis. More detailed analyses about substrate temperature effect on crystallinity can be examined for the films deposited via PECVD technique. The columnar Si structures obtained in ICP-CVD deposited thin films may provide vertical carrier transport channels that can increase the vertical electrical conductivity of Si thin films. Thus vertical conductivity measurements might be performed to observe advantages of the columnar growth. Additionally, doping studies for the ICP-CVD deposited samples might be very useful since this material may serve as a new material with nanostructures for third generation solar cells.

REFERENCES

- [1] T. Markvart, Solar electricity, John Wiley & Sons, 2000.
- [2] H. J. Möller, Semiconductors for solar cells, Artech House Boston, 1993.
- [3] M. A. Green, K. Emery, Y. Hishikawa, W. Warta, and E. D. Dunlop, Progress in Photovoltaics 21 (2013) 1.
- [4] A. Shah, Thin-film silicon solar cells, Epfl Press, Lausanne, 2010.
- [5] J. Meier, H. Keppner, S. Dubail, Y. Ziegler, L. Feitknecht, P. Torres, C. Hof, U. Kroll, D. Fischer, and J. Cuperus, in Proceedings of the 2nd World Conference on PV Energy Conversion, Vienna, 1998, p. 375.
- [6] J. Poortmans and V. Arkhipov, Thin film solar cells: fabrication, characterization and applications, Wiley, 2006.
- [7] X. Deng and E. A. Schiff, (2003)
- [8] D. L. Staebler and C. R. Wronski, Applied Physics Letters 31 (1977) 292.
- [9] P. J. Reddy, Science & technology of photovoltaics, BS Publications, 2010.
- [10] C. Droz, Université de Neuchâtel, 2003.
- [11] W. Luft and Y. S. Tsuo, Hydrogenated amorphous silicon alloy deposition processes, Marcel Dekker New York, 1993.
- [12] R. F. Bunshah, Handbook of Deposition Technologies for Films and Coatings: Science, Applications and Technology, Noyes publications, 1994.
- [13] M. A. Lieberman and A. J. Lichtenberg, (1994)
- [14] M. Konuma, Film deposition by plasma techniques, Springer, 1992.
- [15] F. L. Jones, Reports on Progress in Physics 16 (1953) 216.
- [16] G. I. Babat, Journal of the Institution of Electrical Engineers-Part III: Radio and Communication Engineering 94 (1947) 27.
- [17] M. A. Lieberman and R. A. Gottscho, Physics of Thin Films 18 (1994) 1.
- [18] R. A. Powell and S. M. Rossnagel, PVD for Microelectronics, Academic Press, 1998.
- [19] K. Seshan, Handbook of thin film deposition, William Andrew, 2012.
- [20] D. Song, D. Inns, A. Straub, M. L. Terry, P. Campbell, and A. G. Aberle, Thin Solid Films 513 (2006) 356.
- [21] M. Taniguchi, M. Hirose, T. Hamasaki, and Y. Osaka, Applied Physics Letters 37 (1980) 787.
- [22] I. P. Herman, Optical diagnostics for thin film processing, Academic Press, 1996.

- [23] F. Tochikubo, A. Suzuki, S. Kakuta, Y. Terazono, and T. Makabe, *Journal of Applied Physics* 68 (1990) 5532.
- [24] S. Ilday, G. Nogay, R. Turan, D. Friedrich, and K.-H. Heinig, in *27th European Photovoltaic Solar Energy Conference and Exhibition*, Frankfurt, Germany, 2012.
- [25] H. Fujiwara, *Spectroscopic ellipsometry: principles and applications*, Wiley, 2007.
- [26] H. G. Tompkins and W. A. McGahan, (1999)
- [27] S. Filonovich, H. Aguas, I. Bernacka-Wojcik, C. Gaspar, M. Vilarigues, L. Silva, E. Fortunato, and R. Martins, *Vacuum* 83 (2009) 1253.
- [28] G. Ertl and H. Knözinger, *Handbook of heterogeneous catalysis: 8 volumes*, Wiley-VCH, 2008.
- [29] C. Smit, R. Van Swaaij, H. Donker, A. Petit, W. Kessels, and M. Van de Sanden, *Journal of Applied Physics* 94 (2003) 3582.
- [30] R. Tsu, J. Gonzalez, Hernández, S. Chao, S. Lee, and K. Tanaka, *Applied Physics Letters* 40 (1982) 534.
- [31] W. Bragg and W. Bragg, *Proceedings of the Royal Society of London. Series A* 88 (1913) 428.
- [32] S. Li, Z. Wu, W. Li, Y. Jiang, and N. Liao, *Physica B: Condensed Matter* 403 (2008) 2282.
- [33] A. Mahan, L. Gedvilas, and J. Webb, *Journal of Applied Physics* 87 (2000) 1650.
- [34] A. M. Fox, *Optical properties of solids*, Oxford university press, 2001.
- [35] M. Abdel-Baki and F. El-Diasty, *Current Opinion in Solid State and Materials Science* 10 (2006) 217.
- [36] L. Pavesi, *Materials Today* 8 (2005) 18.
- [37] G. Davies, *Physics reports* 176 (1989) 83.
- [38] S. Ossicini, L. Pavesi, and F. Priolo, *Light emitting silicon for microphotonics*, Springer, 2004.
- [39] O. Vetterl, F. Finger, R. Carius, P. Hapke, L. Houben, O. Kluth, A. Lambertz, A. Mck, B. Rech, and H. Wagner, *Solar Energy Materials and Solar Cells* 62 (2000) 97.
- [40] R. Collins, A. Ferlauto, G. Ferreira, C. Chen, J. Koh, R. Koval, Y. Lee, J. Pearce, and C. Wronski, *Solar Energy Materials and Solar Cells* 78 (2003) 143.
- [41] D. Tsu, B. Chao, S. Ovshinsky, S. Guha, and J. Yang, *Applied Physics Letters* 71 (1997) 1317.
- [42] R. Baghdad, D. Benlakehal, X. Portier, K. Zellama, S. Charvet, J. Sib, M. Clin, and L. Chahed, *Thin Solid Films* 516 (2008) 3965.

- [43] K. Ikuta, Y. Toyoshima, S. Yamasaki, A. Matsuda, and K. Tanaka, *Journal of non-crystalline solids* 198 (1996) 863.
- [44] H. Kakinuma, M. Mohri, M. Sakamoto, and T. Tsuruoka, *Journal of Applied Physics* 70 (1991) 7374.
- [45] K. Nomoto, Y. Urano, J. L. Guizot, G. Ganguly, and A. Matsuda, *Jpn. J. Appl. Phys.* (1990) 1372.
- [46] M. Zhu, X. Guo, G. Chen, H. Han, M. He, and K. Sun, *Thin Solid Films* 360 (2000) 205.
- [47] S. Veprek, F.-A. Sarott, and Z. Iqbal, *Physical Review B* 36 (1987) 3344.
- [48] A. Matsuda, *Journal of non-crystalline solids* 59 (1983) 767.
- [49] H.-Y. Kim, K.-Y. Lee, and J.-Y. Lee, *Thin Solid Films* 302 (1997) 17.
- [50] Z. Iqbal and S. Veprek, *Journal of Physics C: Solid State Physics* 15 (1982) 377.
- [51] S. Saha and S. Ray, *Journal of Applied Physics* 78 (1995) 5713.
- [52] C. Das, A. Dasgupta, S. Saha, and S. Ray, *Journal of Applied Physics* 91 (2002) 9401.
- [53] A. Matsuda, K. Kumayin, and K. Tanaka, *Japanese Journal of Applied Physics* 22 (1983) L34.
- [54] S. Veprek, Z. Iqbal, R. Kuhne, P. Capezzuto, F.-A. Sarott, and J. Gimzewski, *Journal of Physics C: Solid State Physics* 16 (1983) 6241.
- [55] W. G. Van Sark, *Thin Films and Nanostructures* 30 (2002) 1.
- [56] A. Mahan, P. Raboisson, and R. Tsu, *Applied Physics Letters* 50 (1987) 335.
- [57] S. Guha, J. Yang, S. J. Jones, Y. Chen, and D. Williamson, *Applied Physics Letters* 61 (1992) 1444.
- [58] W. Du, X. Yang, H. Povolny, X. Liao, and X. Deng, *Journal of Physics D: Applied Physics* 38 (2005) 838.
- [59] V. Vavrunkova, J. Mullerova, and P. Sutta, *Advances in Electrical and Electronic Engineering* 6 (2011) 108.
- [60] D. Han, K. Wang, J. M. Owens, L. Gedvilas, B. Nelson, H. Habuchi, and M. Tanaka, *Journal of Applied Physics* 93 (2003) 3776.
- [61] S. Mukhopadhyay, C. Das, and S. Ray, *Journal of Physics D: Applied Physics* 37 (2004) 1736.
- [62] J. Kleider, C. Longeaud, R. Bruggemann, and F. Houze, *Thin Solid Films* 383 (2001) 57.
- [63] Z. Ouyang, University of New South Wales, Sydney (2011)

- [64] R. Collins, J. Koh, H. Fujiwara, P. Rovira, A. Ferlauto, J. Zapien, C. Wronski, and R. Messier, *Applied Surface Science* 154 (2000) 217.
- [65] V. I. Merkulov, D. H. Lowndes, G. Jellison, A. Puzder, and D. Geohegan, *Applied Physics Letters* 73 (1998) 2591.
- [66] T. Schulze, L. Korte, F. Ruske, and B. Rech, *Physical Review B* 83 (2011) 165314.
- [67] A. Descoeur, L. Barraud, S. De Wolf, B. Strahm, D. Lachenal, C. Guérouin, Z. Holman, F. Zicarelli, B. Demareux, and J. Seif, *Applied Physics Letters* 99 (2011) 123506.
- [68] S. Adachi, *Optical constants of crystalline and amorphous semiconductors: numerical data and graphical information*, Kluwer Academic Pub, 1999.
- [69] D. Bruggeman, *Ann. Phys* 24 (1935) 636.
- [70] M. Erman, J. Theeten, P. Chambon, S. Kelso, and D. Aspnes, *Journal of Applied Physics* 56 (1984) 2664.
- [71] A. Hadjadj, N. Pham, P. Roca i Cabarrocas, O. Jbara, and G. Djellouli, *Journal of Applied Physics* 107 (2010) 083509.
- [72] Y. Bouzid, C. Abbes, J. Sib, D. Benlakehal, R. Baghdad, L. Chahed, K. Zellama, and S. Charvet, *Journal of Physics: Condensed Matter* 20 (2008) 445221.
- [73] P. Petrik, T. Lohner, M. Fried, L. Biro, N. Khanh, J. Gyulai, W. Lehnert, C. Schneider, and H. Ryssel, *Journal of Applied Physics* 87 (2000) 1734.
- [74] J. Müllerová, S. Jurečka, and P. Šutta, *Solar Energy* 80 (2006) 667.
- [75] L. T. Canham, *Applied Physics Letters* 57 (1990) 1046.
- [76] W. L. Wilson, P. Szajowski, and L. Brus, *Science-New York then Washington* 262 (1993) 1242.
- [77] N. Tomozeiu, *Silicon Oxide (SiO_x, 0 < x < 2): a Challenging Material for Optoelectronics*, 2011.
- [78] A. Puzder, A. Williamson, J. C. Grossman, and G. Galli, *Physical review letters* 88 (2002) 097401.
- [79] N. Karpov, V. Volodin, J. Jedrzejewski, E. Savir, I. Balberg, Y. Goldstein, T. Egenskaya, N. Shwartz, and Z. Yanovitskaya, *Journal of optoelectronics and advanced materials* 11 (2009) 625.
- [80] M. I. Alonso, I. C. Marcus, M. Garriga, A. R. Goni, J. Jedrzejewski, and I. Balberg, *Physical Review B* 82 (2010) 045302.
- [81] U. Kahler and H. Hofmeister, *Optical Materials* 17 (2001) 83.

- [82] D. Nesheva, C. Raptis, A. Perakis, I. Bineva, Z. Aneva, Z. Levi, S. Alexandrova, and H. Hofmeister, *Journal of Applied Physics* 92 (2002) 4678.
- [83] N. V. Nguyen, D. Chandlerhorowitz, P. M. Amirtharaj, and J. G. Pellegrino, *Applied Physics Letters* 64 (1994) 2688.
- [84] M. Ben-Chorin, B. Averboukh, D. Kovalev, G. Polisski, and F. Koch, *Physical review letters* 77 (1996) 763.
- [85] D. Kovalev, H. Heckler, G. Polisski, and F. Koch, *physica status solidi (b)* 215 (1999) 871.
- [86] E. Agocs, P. Petrik, S. Milita, L. Vanzetti, S. Gardelis, A. Nassiopoulou, G. Pucker, R. Balboni, and M. Fried, *Thin Solid Films* 519 (2011) 3002.
- [87] M. Aceves-Mijares, A. A. González-Fernández, R. López-Estopier, A. Luna-López, D. Berman-Mendoza, A. Morales, C. Falcony, C. Domínguez, and R. Murphy-Arteaga, *Journal of Nanomaterials* 2012 (2012) 1.
- [88] K.-J. Lee, T.-D. Kang, H. Lee, S. H. Hong, S.-H. Choi, K. J. Kim, and D. W. Moon, in *Materials Research Society Symposium Proceedings*, Vol. 817, Cambridge Univ Press, 2004, p. 127.
- [89] A. Parashar, S. Kumar, P. N. Dixit, J. Gope, C. M. S. Rauthan, and S. A. Hashmi, *Solar Energy Materials and Solar Cells* 92 (2008) 1199.
- [90] Y. Mai, S. Klein, R. Carius, J. Wolff, A. Lambertz, F. Finger, and X. Geng, *Journal of Applied Physics* 97 (2005) 114913.
- [91] Q. Cheng, S. Xu, S. Huang, and K. Ostrikov, *Crystal Growth & Design* 9 (2009) 2863.
- [92] S. Sriraman, S. Agarwal, E. S. Aydil, and D. Maroudas, *Nature* 418 (2002) 62.
- [93] V. L. Dalal, J. Graves, and J. Leib, *Applied Physics Letters* 85 (2004) 1413.
- [94] S. Ä. Kim, S. Ä. Han, S. Ä. Kuk, D. Ä. Kang, T. Ä. Ha, and M. Ä. Han, in *SID Symposium Digest of Technical Papers*, Vol. 39, Wiley Online Library, 2008, p. 1262.
- [95] K. N. Ostrikov, S. Xu, and M. Y. Yu, *Journal of Applied Physics* 88 (2000) 2268.
- [96] Q. Cheng, S. Xu, and K. Ostrikov, *Nanotechnology* 20 (2009) 215606.
- [97] R. C. Mani, I. Pavel, and E. S. Aydil, *Journal of Applied Physics* 102 (2007) 043305.
- [98] F. Kampas and R. Corderman, *Journal of non-crystalline solids* 59 (1983) 683.
- [99] E. Amanatides, D. Mataras, D. Rapakoulias, M. Van den Donker, and B. Rech, *Solar Energy Materials and Solar Cells* 87 (2005) 795.
- [100] S.-Y. Lien, Y.-C. Chang, Y.-S. Cho, Y.-Y. Chang, and S.-J. Lee, *Electron Devices, IEEE Transactions on* 59 (2012) 1245.

- [101] B. Rech, T. Repmann, S. Wieder, M. Ruske, and U. Stephan, *Thin Solid Films* 502 (2006) 300.
- [102] H. Takatsuka, M. Noda, Y. Yonekura, Y. Takeuchi, and Y. Yamauchi, *Solar Energy* 77 (2004) 951.
- [103] A. A. Howling, B. Strahm, and C. Hollenstein, *Thin Solid Films* 517 (2009) 6218.
- [104] D. Song, E.-C. Cho, G. Conibeer, C. Flynn, Y. Huang, and M. A. Green, *Solar Energy Materials and Solar Cells* 92 (2008) 474.
- [105] A. Matsuda, *Thin Solid Films* 337 (1999) 1.
- [106] J. Li, J. Wang, M. Yin, P. Gao, D. He, Q. Chen, Y. Li, and H. Shirai, *Journal of Applied Physics* 103 (2008) 043505.
- [107] A. Matsuda, *Japanese Journal of Applied Physics* 43 (2004) 7909.
- [108] C. C. Tsai, J. C. Knights, G. Chang, and B. Wacker, *Journal of Applied Physics* 59 (1986) 2998.
- [109] A. Y. Kovalgin, A. Boogaard, I. Brunets, J. Holleman, and J. Schmitz, *Surface and Coatings Technology* 201 (2007) 8849.
- [110] J. Krug and P. Meakin, *Physical Review A* 43 (1991) 900.
- [111] Y. Saito and S. Omura, *Physical Review E* 84 (2011)
- [112] A. Gorsky, S. Nechaev, R. Santachiara, and G. Schehr, *Nuclear Physics B* 862 (2012) 167.
- [113] A. Robledo, C. N. Grabill, S. M. Kuebler, A. Dutta, H. Heinrich, and A. Bhattacharya, *Physical Review E* 83 (2011)
- [114] A. L. Barabasi and H. E. Stanley, *Fractal concepts in surface growth*, Cambridge university press, Cambridge, 1995.
- [115] B. Šmíd, Z. Li, A. Dohnáková, B. W. Arey, R. S. Smith, V. Matolín, B. D. Kay, and Z. Dohnálek, *The Journal of Physical Chemistry C* 116 (2012) 10649.
- [116] D. W. Flaherty, Z. Dohnalek, A. Dohnalkova, B. W. Arey, D. E. McCready, N. Ponnusamy, C. B. Mullins, and B. D. Kay, *The Journal of Physical Chemistry C* 111 (2007) 4765.
- [117] Z. Dohnalek, G. A. Kimmel, D. E. McCready, J. S. Young, A. Dohnalkova, R. S. Smith, and B. D. Kay, *The Journal of Physical Chemistry B* 106 (2002) 3526.
- [118] S. Mukhopadhyay, C. Das, and S. Ray, *Journal of Physics D: Applied Physics* 37 (2004) 1736.
- [119] D. Han, K. Wang, J. M. Owens, L. Gedvilas, B. Nelson, H. Habuchi, and M. Tanaka, *Journal of Applied Physics* 93 (2003) 3776.

- [120] M. M. Adachi, K. L. Kavanagh, and K. S. Karim, *Journal of Vacuum Science & Technology A: Vacuum, Surfaces, and Films* 25 (2007) 464.
- [121] A. H. Mahan, L. M. Gedvilas, and J. D. Webb, *Journal of Applied Physics* 87 (2000) 1650.
- [122] U. Kroll, J. Meier, A. Shah, S. Mikhailov, and J. Weber, *Journal of Applied Physics* 80 (1996) 4971.
- [123] Y. Qin, H. Yan, F. Li, L. Qiao, Q. Liu, and D. He, *Applied Surface Science* 257 (2010) 817.
- [124] L. Khriachtchev, T. Nikitin, C. J. Oton, R. Velagapudi, J. Sainio, J. Lahtinen, and S. Novikov, *Journal of Applied Physics* 104 (2008) 104316.
- [125] J. F. Moulder, J. Chastain, and R. C. King, *Handbook of X-ray photoelectron spectroscopy: a reference book of standard spectra for identification and interpretation of XPS data*, Physical Electronics Eden Prairie, MN, 1995.
- [126] D. J. Lockwood, *Semiconductors and Semimetals* 49 (1997) 1.
- [127] A. Cullis, L. T. Canham, and P. Calcott, *Journal of Applied Physics* 82 (1997) 909.
- [128] F. Iacona, G. Franzo, and C. Spinella, *Journal of Applied Physics* 87 (2000) 1295.
- [129] L. Canham, *physica status solidi (b)* 190 (1995) 9.
- [130] S. Godefroo, M. Hayne, M. Jivanescu, A. Stesmans, M. Zacharias, O. Lebedev, G. Van Tendeloo, and V. V. Moshchalkov, *Nature nanotechnology* 3 (2008) 174.
- [131] A. M. Ali, *Journal of luminescence* 126 (2007) 614.
- [132] B. Averboukh, R. Huber, K. Cheah, Y. Shen, G. Qin, Z. Ma, and W. Zong, *Journal of Applied Physics* 92 (2002) 3564.
- [133] X. Wang, J. Zhang, L. Ding, B. Cheng, W. Ge, J. Yu, and Q. Wang, *Physical Review B* 72 (2005) 195313.
- [134] J. Tauc, R. Grigorovici, and A. Vancu, *physica status solidi (b)* 15 (1966) 627.
- [135] J. Pankove, Academic Press, 1984.
- [136] G. Cody, *Journal of non-crystalline solids* 141 (1992) 3.
- [137] S. Knief and W. von Niessen, *Physical Review B* 59 (1999) 12940.
- [138] V. Lehmann and U. Gösele, *Applied Physics Letters* 58 (1991) 856.